

ABSTRACT

Title of Dissertation: **A Study of Diverse Hot Jupiter Atmospheres**
 Guangwei Fu
 Doctor of Philosophy, 2022

Dissertation Directed by: **Professor Drake Deming**
 Department of Astronomy

The discovery of over 5000 planets outside the solar system has evermore changed our view of the universe and the tale of other worlds beyond Earth is no longer folklore. In 1989, David Latham found the first planetary candidate HD 114762b ([Latham et al., 1989](#)) using the radial velocity technique which was later used to discover 51 Pegasi b as the first exoplanet orbiting a solar-type star by Didier Queloz and Michel Mayor ([Mayor and Queloz, 1995](#)). Then back to December 1999, the first transiting exoplanet HD 209458b lightcurve was measured by David Charbonneau ([Charbonneau et al., 2002](#)). The gold rush of exoplanet discovery and characterization today is probably beyond the wildest dreams of the early pioneers.

From the early days of discovering hot Jupiters, we are now able to study their atmospheres in detail. This thesis focuses on the study of hot Jupiter atmospheres. Hot Jupiters are rare outcomes of planet formation and their origin remains a mystery ([Dawson and Johnson, 2018](#)). The study of their atmospheres can help us to understand their formation and evolution history and also develop techniques for future remote sensing of potentially habitable transiting exoplanets in the search for life beyond earth. Just like our solar system with every planet being special and

different, the same is true for hot Jupiters. I will first go into detailed studies of 4 individual hot Jupiters (WASP-76b, WASP-74b, HAT-P-41b, and KELT-20b) and then connect them to more broad population-level statistical studies.

These four hot Jupiters all have dayside temperatures exceeding 2000K with an inflated radius and a very short (<10 days) orbital period. However, they exhibit different atmospheric features and properties. The relatively cooler ones like WASP-74b and HAT-P-41b show mostly blackbody-like dayside emission spectra which indicate isothermal temperature-pressure profiles. The largely featureless transmission spectrum from WASP-74b is likely caused by clouds condensing in the terminator region. On the other hand, the hotter WASP-76b dayside shows CO emission features with evidence for water thermal dissociation. Combined with heavy metal absorption features seen in the NUV part of the transmission spectrum, gaseous metals are likely causing thermal inversion in the upper atmosphere. KELT-20b shows the strongest water and CO emission features on the dayside despite a similar dayside temperature compared to WASP-76b. The unique A-type host star of KELT-20b is likely the difference-maker. The intense short-wavelength UV/NUV radiation from the A star gets preferentially absorbed in the upper atmospheres by the gaseous metals which heats up the corresponding layers and drives stronger thermal inversion.

The dayside emission spectra of these four planets are then compared to all other hot Jupiters with temperatures ranging from $\sim 1500\text{K}$ to over 4000K . These four planets sit in a key transitional parameter space where we see dayside emission spectra from cooler planets mostly have water absorption features and hotter planets are mostly blackbody-like. This trend shows the cooler (<2000K) planets do not have high altitude absorbers needed for thermal inversion, and the much hotter (>3000K) ones are affected by thermal dissociation of water and rising continuum opacity of H^- . Only in this in-between temperature range combined with strong

inversion from gaseous metal absorbers and strong UV radiation, we could see prominent water emission features.

I also did a population-level statistical study of all observed transmission spectra focused on the $1.4 \mu m$ water band. Each spectrum was fitted to determine the water feature strength which is then normalized by the planetary atmospheric scale height. I found a statistically significant trend of stronger water absorption features as a function of planet equilibrium temperature. This trend can be explained by the presence of aerosols which condense more easily under cooler conditions. Although this study was conducted back in 2017 before my other publications, the trend still holds and provides a valuable statistical comparison study framework for exoplanet atmospheres.

A Study of Diverse Hot Jupiter Atmospheres

by

Guangwei Fu

Dissertation submitted to the Faculty of the Graduate School of the
University of Maryland, College Park in partial fulfillment
of the requirements for the degree of
Doctor of Philosophy
2022

Advisory Committee:

Professor Drake Deming, Advisor

Professor Eliza Kempton, Chair

Professor Derek Richardson

Professor Thaddeus Komacek

Professor David Sing

Professor Kayo Ide

© Copyright by
Guangwei Fu
2022

Preface

The research presented in Chapters 2,3,4,5 and 6 of this dissertation has been previously published.

Chapter 2 is presented with only minimal modification since appearing in *The Astronomical Journal* (AJ) as “The Hubble PanCET Program: Transit and Eclipse Spectroscopy of the Strongly Irradiated Giant Exoplanet WASP-76b” (Fu et al., 2021). Paper authors are Guangwei Fu, Drake Deming, Joshua Lothringer, Nikolay Nikolov, David K. Sing, Eliza M.-R. Kempton, Jegug Ih, Thomas M. Evans, Kevin Stevenson, H. R. Wakeford, Joseph E. Rodriguez, Jason D. Eastman, Keivan Stassun, Gregory W. Henry, Mercedes López-Morales, Monika Lendl, Dennis M. Conti, Chris Stockdale, Karen Collins, John Kielkopf, Joanna K. Barstow, Jorge Sanz-Forcada, David Ehrenreich, Vincent Bourrier, and Leonardo A. dos Santos. The data was collected from multiple observing programs as listed in the paper. I performed the WFC3 transit and eclipse data reduction, the binary star contamination correction. Drake Deming did the Spitzer data reduction. Nikolov did the STIS data reduction. David Sing did the ATMO retrieval and Joshua Lothringer did the PHOENIX forward modeling. I did the combined analysis and wrote the majority of the manuscript.

Chapter 3 is presented with only minimal modification since appearing in *The Astronomical Journal* (AJ) as “The Hubble PanCET program: Transit and Eclipse Spectroscopy of the Hot-Jupiter WASP-74b” (Fu et al., 2021). Paper authors are Guangwei Fu, Drake Deming, Erin May, Kevin Stevenson, David K. Sing, Joshua D. Lothringer, H. R. Wakeford, Nikolay Nikolov,

Thomas Mikal-Evans, Vincent Bourrier, Leonardo A. dos Santos, Munazza K. Alam, Gregory W. Henry, Antonio García Muñoz, and Mercedes López-Morales. The data was collected from multiple observing programs as listed in the paper. I performed the WFC3 transit and eclipse data reduction. Drake Deming and Erin May did the Spitzer data reduction. David Sing did the STIS data reduction. I did the PLATON retrieval, combined analysis and wrote the majority of the manuscript.

Chapter 4 is presented with only minimal modification since appearing in *The Astronomical Journal* (AJ) as “The Hubble PanCET Program: Emission Spectrum of Hot Jupiter HAT-P-41b” (Fu et al., 2022a). Paper authors are Guangwei Fu, David K. Sing, Drake Deming, Kyle Sheppard, H. R. Wakeford, Thomas Mikal-Evans, Munazza K. Alam, Leonardo A. Dos Santos, Mercedes López-Morales, and Joshua D. Lothringer. The data was collected from multiple observing programs as listed in the paper. I performed the WFC3 eclipse data reduction. David Sing did the ATMO retrieval. I did the combined analysis and wrote the manuscript.

Chapter 5 is presented with only minimal modification since appearing in *The Astrophysical Journal Letters* (ApJL) as “Strong H₂O and CO Emission Features in the Spectrum of KELT-20b Driven by Stellar UV Irradiation” (Fu et al., 2022b). Paper authors are Guangwei Fu, David K. Sing, Joshua D. Lothringer, Drake Deming, Jegug Ih, Eliza M. -R. Kempton, Matej Malik, Thaddeus D. Komacek, Megan Mansfield, and Jacob L. Bean. I wrote the HST telescope proposal and planned the observation to collect the WFC3 eclipse data. I did the data reduction and Drake Deming did the Spitzer data reduction. David sing did the ATMO retrieval. I did the combined analysis and wrote the manuscript.

Chapter 6 is presented with only minimal modification since appearing in *The Astrophysical Journal Letters* (ApJL) as “Statistical Analysis of Hubble/WFC3 Transit Spectroscopy of Extrasolar

Planets” ([Fu et al., 2017](#)). Paper authors are Guangwei Fu, Drake Deming, Heather Knutson, Nikku Madhusudhan, Avi Mandell, and Jonathan Fraine. The data was collected from previous published datasets. I did the statistical analysis of all the data and wrote the manuscript.

Dedication

To family and friends

Acknowledgments

I would like to first thank my parents for kindling my interest in science and technology from a very young age and continue to support my pursuit and curiosity throughout the years. My path to become an astronomer was never planned from the beginning. It was full of coincidences and luck. In the summer of 2014, I was just an undergraduate at UW-Madison looking for a summer job. After many failed attempts at the engineering department, I decided to walk around the astronomy department. Luckily Prof. Matthew Bershadsky was in his office that afternoon and gave me a job at his fiber optics lab for the Sloan digital sky survey. I would like to thank Matt for keeping his office door open that afternoon and giving me the opportunity to start a career in astronomy.

After undergraduate, it was then probably pure luck that I got into graduate school at University of Maryland since it was the only acceptance out of the 20 schools I applied. Even more fortunate that I found a great PhD advisor Drake Deming right from the beginning. Thank you Drake for giving me a terrific graduate school experience, especially during the first few years when you trained me to become an independent researcher. I am honored to become your last graduate student!

During the last couple years of my graduate school most things went remote due to COVID-19 and David Sing took me in a part of his research group at JHU. David has not only been a close and extremely helpful collaborator but also an unofficial advisor to me. Thanks for all the

valuable advice you gave me and I look forward to my next chapter at JHU!

Thank you Eliza for serving as the committee chair and all your help during my time at UMD. Time has flew by since we both started at UMD five years ago!

Table of Contents

Preface	ii
Dedication	v
Acknowledgements	vi
Table of Contents	viii
List of Tables	xi
List of Figures	xii
Chapter 1: Introduction	1
1.1 Why do we study exoplanets?	1
1.2 Why do we study exoplanet atmosphere?	2
1.3 Why do we study hot Jupiter atmospheres?	3
1.4 How do we study hot Jupiter atmospheres?	4
1.4.1 How we study hot Jupiter atmospheres with space-based telescopes	6
Chapter 2: Transit and Eclipse Spectroscopy of the Strongly Irradiated Giant Exoplanet WASP-76b	8
2.1 Overview	8
2.2 Introduction	9
2.3 Observations and Data Analysis	11
2.3.1 Companion Star & EXOFASTv2 Fit	11
2.3.2 HST STIS G430L & G750L	14
2.3.3 HST WFC3 G141	15
2.3.4 Spitzer IRAC	20
2.4 PHOTOMETRIC OBSERVATIONS OF WASP-76	28
2.5 Comparison with previous studies	30
2.6 Analysis & Interpretation	32
2.6.1 Strong metal absorbers in STIS G430L spectrum	34
2.6.2 Detection of TiO and H ₂ O	36
2.6.3 Emission spectrum	38
2.6.4 Temperature inversion	39
2.6.5 Model comparison	40
2.7 Summary and Conclusions	42

2.8	Appendix	43
Chapter 3:	Transit and Eclipse Spectroscopy of the Hot Jupiter WASP-74b	47
3.1	Overview	47
3.2	Introduction	47
3.3	Observations	49
3.4	Data analysis	50
3.4.1	HST STIS data reduction	50
3.4.2	HST WFC3 data reduction	51
3.4.3	Spitzer data reduction	51
3.5	Simultaneous ground-based photometric monitoring	54
3.6	Comparison with previous studies	56
3.7	PLATON retrieval	61
3.7.1	Transit retrieval	61
3.7.2	Eclipse retrieval	62
3.8	Follow up observations with JWST	65
3.9	Conclusion	66
3.10	Appendix	66
Chapter 4:	Emission spectrum of hot Jupiter HAT-P-41b	80
4.1	Overview	80
4.2	Introduction	80
4.3	Observations	83
4.4	HST WFC3 data reduction	83
4.5	Retrieval analysis	84
4.6	Compared with other hot Jupiter atmospheres	88
4.7	Conclusion	90
Chapter 5:	Strong H₂O and CO emission features in the spectrum of KELT-20b driven by stellar UV irradiation	92
5.1	Overview	92
5.2	Introduction	93
5.3	Observations and data reduction	94
5.3.1	HST Analysis	94
5.3.2	TESS Analysis	95
5.3.3	Spitzer Analysis	95
5.4	ATMO retrieval and PHOENIX model	98
5.5	Discussion	99
5.5.1	S _{H₂O} water feature strength	101
5.5.2	WFC3/G141 to Spitzer 4.5 μm brightness temperature difference	102
5.5.3	High-resolution spectroscopy	103
5.6	Conclusion	105
Chapter 6:	Statistical Analysis of Hubble/WFC3 Transit Spectroscopy of Extrasolar Planets	107

6.1	Overview	107
6.2	Introduction	108
6.3	Data Analysis	110
6.4	Statistical Correlations	113
6.5	Summary and Conclusions	118
Chapter 7: Conclusion		122
7.1	What have we learned about hot Jupiter atmospheres?	122
7.2	What is next for hot Jupiter atmospheres?	123
7.2.1	Finding the origin of hot Jupiters through atmospheric characterization	123
7.2.2	Understanding the chemical and physical processes of hot Jupiters	124
7.3	What is beyond hot Jupiter atmospheres?	125
Appendix A: Facilities and Software		127
A.1	Facilities	127
A.2	Software	127

List of Tables

2.1	A list of our 7 transit and 5 eclipse observations of WASP-76b.	11
2.2	Measured flux ratio between WASP-76A and WASP-76B in 5 different bands from HST STIS, Wöllert and Brandner (2015) and KECK-AO NIRC2.	14
2.3	Transit and eclipse times and depths for WASP-76b in the Spitzer bands. These are "as observed" transit/eclipse depths, not corrected for dilution by the companion star. The two eclipses from GO 12085 (PI: Deming) were published in (Garhart et al., 2020) and therefore not included here.	28
2.4	SUMMARY OF AIT PHOTOMETRIC OBSERVATIONS OF WASP-76	30
2.5	ATMO transit retrieval priors & Posteriors	33
2.6	ATMO eclipse retrieval priors & Posteriors	33
3.1	A list of our 6 transit and 3 eclipse observations of WASP-74b.	49
3.2	Parameters are from (Mancini et al., 2019).	49
3.3	SUMMARY OF AIT PHOTOMETRIC OBSERVATIONS OF WASP-74	56
3.5	60
3.7	60
3.9	60
3.11	61
3.12	WASP-74b transit spectrum	67
3.13	Transit spectrum LD coefficients	69
3.14	WASP-74b eclipse spectrum	75
4.2	87
4.3	HAT-P-41b eclipse spectrum	91
5.1	KELT-20b eclipse spectrum	104
6.1	Absorption in scale heights (A_H), based on spectra from Tsiaras et al. (2018) unless otherwise noted. Our analysis used the A_H values from fitting to the strongest region of water absorption (1.3 - 1.65 μm), versus the entire WFC3 bandpass (1.1 - 1.65 μm), both listed in the middle set of columns. The columns on the right give values for comparison, based on spectra from other authors. T_{eq} calculated from parameters in corresponding references are listed in the left column.	121

List of Figures

1.1	Illustration of the transmission and emission spectroscopy techniques (Sing, 2018).	5
2.1	Resolved images of spectrum of the WASP-76 binary system, obtained with HST STIS F28X50LP (Top Left), G750L spectrum (Top Right), Keck-AO NIRC2 Brackett-gamma (Bottom Left) and J-Cont (Bottom Right).	13
2.2	Two-component SED fit for WASP-76A (black) and WASP-76B (red) with the blue points as integrated fluxes and cyan points as spatially resolved flux measurements.	14
2.3	Satellite crossing contamination frames. Spatial scan is in the vertical direction and wavelength is in the horizontal direction.	18
2.4	The effect of satellite crossing contamination on the white light transit curve. The two satellite contaminated data points have very high flux and were set to fixed values to show the timing of the events. Satellite crossing (a) was significantly more severe than satellite crossing (b) and distorted the ramp shape for the third orbit. We decided to discard the frames after satellite crossing (a), see text. The upper and lower sets of points are due to spectra vertical shifts during the forward versus backward scan.	20
2.5	Spitzer transit light curves in 3.6 and 4.5 μm after systematic correction.	21
2.6	HST STIS G430L visit one light curves for each spectral channel. Left panel: raw light curves with evident systematics as a function of telescope orbital phase. Middle panel: De-trended light curves overplotted by the best-fitting transit models. Right panel: corresponding residual (data minus fit) for each spectral channel with the dotted lines showing the 1σ standard deviation.	22
2.7	Same as Fig 2.6 but for HST STIS G430L visit 2.	23
2.8	Same as Fig 2.6 but for HST STIS G750L.	24
2.9	HST WFC3 G141 spectral bin transit lightcurves after ramp-effect correction using RECTE (left) and corresponding residuals (right). The dotted lines in the residual plot represent expected photon noise.	25
2.10	HST WFC3 G141 spectral bin eclipse light curves after ramp-effect correction using RECTE (left) and corresponding residuals (right). The dotted lines in the residual plot represent expected photon noise.	26
2.11	<i>Top</i> : AIT photometry of WASP-76 between 2014 and 2020 but lacking the 2017-18 observing season. The observations have been normalized so that all observing seasons have the same mean as the first season. <i>Bottom</i> : Frequency spectrum of the normalized observations showing the lack of any significant periodicity between 1 and 100 days.	31

2.12	Transmission spectrum of WASP-76b overplotted two different best-fit models. The green line is the PHOENIX atmosphere model with equilibrium chemistry, solar metallicity and internal temperature of 200K. The blue line is the best-fit models from ATMO retrieval.	35
2.13	The eclipse spectrum (left panel) of WASP-76b overplotted with two PHOENIX (green and orange) models and one ATMO (blue) best-fit spectrum. The two PHOENIX models are both at solar metallicity with dayside heat redistribution, but one with TiO/VO and the other without. The comparison is to show the presence of TiO/VO is strongly favored by the data. The corresponding TP profiles are plotted in the right panel with matching colors to the three emission model spectra.	37
2.14	The TP profiles of ATMO retrieval (blue) and PHOENIX (black) atmosphere model for the emission spectrum. The dashed blue lines represent one and two sigma range for ATMO TP profiles.	38
2.15	Partial pressure contours of four chemical species (Fe, TiO, H ₂ O and H-) overplotted with PHOENIX model TP profiles from transit (full heat redistribution, dashed lines) and eclipse (dayside heat redistribution, dotted lines) spectra. Gaseous Fe is abundant and present in both the terminator and dayside regions of the planet across all pressure levels. TiO and water vapor exist in higher pressure regions but begin to dissociate in higher temperature and altitude layers. H- is limited in the cooler terminator but starts to show up on the hotter dayside.	41
2.16	Transit lightcurves used in EXOFASTv2 fit.	44
2.17	The posterior distribution of ATMO retrieval of the transmission spectrum. Six chemical elements (C, O, Na, Ti, V, Fe) are allowed to vary freely with everything else scale to solar metallicity. All retrieved elemental abundance are consistent with solar value to one sigma.	45
2.18	The posterior distribution of ATMO retrieval of the emission spectrum. The carbon and oxygen abundances are poorly constrained due to a muted water feature in the WFC3/G141 band. Retrieved solar metallicity is consistent with results from the transmission spectrum and the PHOENIX models.	46
3.1	Centroids (top panels), raw flux (middle panels) and corrected flux (bottom panels) as a function of phase for all four Spitzer IRAC data sets as labeled. One can see that the 3.6 μm data sets are more heavily affected by a visit-long ramp, in combination with a stronger initial ramp for the 3.6 μm transit event. The trimmed parts of the lightcurves are shaded in grey.	52
3.2	BLISS maps from best fits for all 4 Spitzer IRAC events as labeled. For the 4.5 μm maps, the darker grey regions denote where the fixed sensitivity map exists. Axis units are in sub-pixels. The BLISS map shown here is the subset of the fixed sensitivity map at the locations of the data centroids. It is not generated from this 4.5 μm dataset.	53

3.3	Demonstration of the dependence on ramp choice and amount of data trimmed from the start of events. The $3.6 \mu m$ and $4.5 \mu m$ events are shown on the same scale for ease of comparison. Left: Transits, Right: Eclipses. Top: $3.6 \mu m$, Bottom: $4.5 \mu m$. Our use of the fixed sensitivity map for systematic removal at $4.5 \mu m$ results in a consistent eclipse and transit depth regardless of pre-trimming and ramp model, while the $3.6 \mu m$ events are heavily dependent on the choice of these parameters due to the flexibility of the BLISS map.	54
3.4	<i>Top</i> : The Cousins R band photometry of WASP-74 from 2018–2021, acquired with the C14 automated imaging telescope (AIT) at Fairborn Observatory. The star is constant on night-to-night and year-to-year time scales to the limit of our precision. <i>Bottom</i> : Frequency spectrum of the complete data set shows no significant periodicity between 1 and 100 days. The horizontal dashed line in the bottom panel represents the noise limit below which reliable periods are not found in multi-color photometry (Henry et al., 2011).	57
3.5	Comparison of transit spectra from this study to previous studies. We have fixed all orbital parameters to the exactly values as used in (Mancini et al., 2019).	58
3.6	Comparison of Spitzer eclipse spectra from this study to (Garhart et al., 2020). We have fixed all orbital parameters to the exactly values as used in Mancini et al. (2019).	58
3.7	Best-fit PLATON retrieval of WASP-74b transit spectrum. Purple line is the full resolution model with pink dots for corresponding binned model. Left panel uses the full spectrum and the right panel excludes the $3.6 \mu m$ point. We see strong scattering with muted water feature and no evidence for TiO absorption or super-Rayleigh scattering in both retrievals. However, the low $3.6 \mu m$ point does drive up the cloud scattering factor.	62
3.8	Best-fit PLATON retrieval of WASP-74b eclipse spectrum. Left panel uses the full spectrum and the right panel excludes the $3.6 \mu m$ point. Purple line is the full resolution model with pink dots for corresponding binned model and overplotted with blackbody at 2260K in orange represent dayside only heat redistribution. In the full spectrum (left), we see a featureless blackbody-like WFC3/G141 spectrum with a methane absorption feature at $3.6 \mu m$ band. Without the $3.6 \mu m$ point (right), the methane absorption feature disappears and the retrieved C/O ratio drops significantly.	63
3.9	TP profile from PLATON eclipse retrieval with the solid line as the median values and shaded regions representing one sigma uncertainty. Left panel uses the full spectrum and the right panel excludes the $3.6 \mu m$ point. The TP profiles are highly consistent showing the thermal structure is not sensitive to the one $3.6 \mu m$ point.	64
3.10	HST STIS G430L visit 1 spectral bin transit lightcurves after systematics correction using jitter decorrelation (left) and corresponding residuals (right).	67
3.11	HST STIS G430L visit 2 spectral bin transit lightcurves after systematics correction using jitter decorrelation (left) and corresponding residuals (right).	71
3.12	HST STIS G750L spectral bin transit lightcurves after systematics correction using jitter decorrelation (left) and corresponding residuals (right).	72

3.13	HST WFC3 G141 spectral bin transit lightcurves after ramp-effect correction using RECTE (left) and corresponding residuals (right).	73
3.14	HST WFC3 G141 spectral bin eclipse lightcurves after ramp-effect correction using RECTE (left) and corresponding residuals (right).	74
3.15	Posterior distribution of PLATON retrieval on the transit spectrum.	76
3.16	Posterior distribution of PLATON retrieval on the transit spectrum without the Spitzer 3.6 μm point.	77
3.17	Posterior distribution of PLATON retrieval on the eclipse spectrum.	78
3.18	Posterior distribution of PLATON retrieval on the eclipse spectrum without the Spitzer 3.6 μm point.	79
4.1	HST WFC3 G141 spectral bin transit lightcurves after ramp-effect correction using RECTE (left) and corresponding residuals (right) with their relative ratios to the photon-limit noise (σ/σ_γ) levels.	82
4.2	The WFC3/G141 emission spectrum of HAT-P-41b is in excellent agreement with Mansfield et al. (2021).	82
4.3	ATMO retrieval of HAT-P-41b emission spectrum. The featureless blackbody-like spectrum (left) is best fitted with an isothermal TP profile (right).	84
4.4	Posterior distribution of the ATMO retrieval for HAT-P-41b. The metallicity is mostly unconstrained due to a lack of features within the emission spectrum.	85
4.5	HAT-P-41b WFC3/G141 emission spectrum compared with other hot Jupiters. The water feature strength index (S_{H_2O}) (Mansfield et al., 2021) measures the 1.4 μm water band feature size relative to the blackbody model based on the out-of-band spectrum. Centered at zero being the blackbody-like featureless spectrum. Increasing negative values (redder color) represent stronger emission features and increasing positive values (bluer color) represent stronger absorption features. The circle size scales with the host star temperature (T_{eff}). The grey vertical dash lines are condensation lines for various metals at 100 mbar assuming solar metallicity. We see mostly featureless spectra at higher dayside temperatures ($>2700K$) where H^- continuum opacity is expected to dominate (Parmentier et al., 2018). At the lower temperature side, we see mostly water absorption features where the atmosphere is too cool for gaseous heavy metal absorbers such as TiO to form and drive thermal inversion. HAT-P-41b sits at this in-between transitional region where planets can have absorption, emission or featureless spectra. Further observations of HAT-P-41b in the longer wavelength with JWST will help us to precisely determine its thermal structure and understand what causes thermal inversion in hot Jupiters atmospheres.	86

5.1	The emission spectrum of KELT-20b (black) is overplotted with the ATMO retrieval best-fit model (purple), PHOENIX forward model (pink), and blackbody model of 2402K (grey). The blue shaded regions represent 1 to 3 σ uncertainties from ATMO retrieval. The TP profiles are shown on the right with corresponding colors for ATMO and PHOENIX best-fit models. The blue shaded region represents 1 σ uncertainties. Contribution functions from ATMO for each wavelength channel are overplotted in dashed lines. The data probe pressure levels range from 100 to 1mbar with TESS being the lowest pressure and the blue side of WFC3/G141 (1.1-1.3 μm) being the highest. We detected prominent H ₂ O and CO emission features indicating a strongly inverted TP profile as shown by both models. The excellent agreement of the TP profiles between ATMO and PHOENIX shows the dayside atmosphere is or very close to radiative equilibrium.	97
5.2	KELT-20b emission spectrum metrics compared with other hot Jupiters with day side temperature higher than 2200K overplotted with PHOENIX models assuming solar metallicity and C/O ratio. The top panel shows the water feature strength metric S_{H_2O} from Mansfield et al. (2021) and KELT-20b is located in a unique parameter space of high host star temperature combined with low dayside temperature. The large water emission feature from KELT-20b is consistent with the PHOENIX model predictions. The bottom panel shows the Spitzer 4.5 μm blackbody brightness temperature relative to the WFC3/G141 out of water band blackbody brightness temperature. The large difference between the two bands in KELT-20b indicates a prominent CO emission feature.	100
5.3	Posterior distribution of ATMO retrieval. The retrieved metallicity, carbon, and oxygen abundances are ~ 3.9 , 10, and 17 times higher than the solar values, but the retrieved C/O ratio of $0.454^{+0.211}_{-0.205}$ is consistent with the solar value to within one sigma. The log(g) is not well constrained as the emission spectrum is not sensitive to surface gravity.	106
6.1	Example of our MCMC fitting of an Exo-transmit template spectrum to the data for WASP-67b. This planet has the median χ_ν^2 in the sample, with $\chi_\nu^2 = 1.05$. The a coefficient is the amplitude scale factor for fitting the Exo-transmit template spectrum, and b is the wavelength coefficient of a baseline slope. The $\leq 1\sigma$ contours are shaded in blue for the posterior distribution samples (lower left) and for the fit to the data (upper right).	110
6.2	The upper panel is the 1.3 - 1.6 μm absorption in scale heights versus planet equilibrium temperature. We infer a positive baseline slope correlation (p-value = 0.01) with upward scattering on the left side. After applying the binning method discussed in section 3, we obtain a statistically significant ($r_s = 0.85$) baseline correlation as shown in the lower panel. Mass uncertainty is proportional to squares size. The eight planets shaded in blue circles in the upper panel are the ones investigated in (Sing et al., 2016)	115
6.3	Planet surface gravity, mass, and radius versus absorption in scale heights (1.3-1.65 μm). We do not detect any significant statistical correlation; the suggestion of a correlation with mass is due to an intrinsic degeneracy in the sample, combined with the temperature correlation shown in Figure 2.	116

6.4 Upper plot shows the distribution of absorption in scale heights ($1.3 - 1.65 \mu\text{m}$) is more likely to be log-normal than normal. This is caused by the target selection bias as there are more cooler planets than hotter ones in the sample (shown in the lower panel). 117

List of Abbreviations

CCD	Charge-Coupled Device
GO	General Observer
HAT	Hungarian Automated Telescope
HST	Hubble Space Telescope
IRAC	Infrared Array Camera
JWST	James Webb Space Telescope
KELT	Kilodegree Extremely Little Telescope
MCMC	Markov Chain Monte Carlo
NASA	National Aeronautics and Space Administration
NUV	Near Ultraviolet
NIRSpec	Near Infrared Spectrograph
NIRISS/SOSS	Near Infrared Imager and Slitless Spectrograph/Single-Object Slitless Spectroscopy
PanCET	Panchromatic Comparative Exoplanet Treasury
PLATON	PLanetary Atmospheric Tool for Observer Noobs
STIS	Space Telescope Imaging Spectrograph
TESS	Transiting Exoplanet Survey Satellite
TRAPPIST	TRAnsiting Planets and Planetesimals Small Telescope
WASP	Wide-Angle Search for Planets
WFC3	Wide Field Camera 3

Chapter 1: Introduction

1.1 Why do we study exoplanets?

A captivating question is at the core of every significant human endeavor. To be the fastest-growing subfield in astronomy, the study of exoplanets must touch on the most fundamental questions that we ask. Humans evolved to become curious and social beings through random natural processes and selection. We wonder about the unknown and long for companionship. Even before discovering outer space, we have fantasized about life from within the clouds to the moon and the Sun. Astronomy first brought us an understanding of the solar system and further sparked our interests in life beyond earth. As sung by David Bowie, "Is there life on Mars?" The discovery of exoplanets then opens countless more possible cradles for life.

All life forms known to date are from Earth, a rocky planet with liquid water and an oxygen-rich atmosphere. Although we can not generalize Earth as the only suitable environment for life to flourish, it is a starting point based on the only data point we have. If life can happen once on Earth, it could happen again somewhere else similar. Therefore the next natural logical step of searching for life beyond earth will be the search for Earth-like planets around other stars.

Over 5000 exoplanets have been discovered to date and roughly a third are gas giants like Jupiter and Saturn, a third being Neptune-like and another third being Super-Earth. Only around 4% are actually small rocky terrestrial planets similar to earth. The sample size is heavily biased

by the discovery technique limitations with larger and shorter period planets being the easiest to discover. However, even the 4% represents ~ 200 earth-like planets for us to search for another habitable planet.

Using Earth as the blueprint for a habitable home of life, we are looking for planets with liquid water on the surface ([Kasting and Catling, 2003](#)) which requires the planet to have a narrow range of suitable temperature (273 to 373K) at one atmospheric pressure. The planet will also need to be able to hold on to its atmosphere from stellar wind driven atmospheric escape ([Murray-Clay et al., 2009](#)).

1.2 Why do we study exoplanet atmosphere?

Measuring the bulk mass, radius, and equilibrium temperature of exoplanets can give us a general picture of the type of planets they are, but will not tell us if there is life on them. To know that we need to characterize their atmospheres. Earth's atmosphere is constantly being affected by life on the surface. From photosynthesis of plants and organisms converting carbon dioxide to oxygen, to human and animal activities generating greenhouse gases. The presence of life on Earth leaves unique atmospheric signatures compared to all other planets in the solar system.

Using a similar methodology we can study the atmospheres of exoplanets and search for atmospheric features that would indicate biological processes. Maybe we will find oxygen and methane just like what we see on Earth, or we may discover other complex and unexpected atmospheric species that could be the product of evolution ([Seager et al., 2016](#)). The study of exoplanet atmosphere will give us a direct pathway to search for evidence of life beyond Earth.

1.3 Why do we study hot Jupiter atmospheres?

The atmosphere is usually only $\sim 1\%$ of the planetary radius which means atmospheric characterization of small rocky planets is extremely challenging and out of reach for the current generation of telescopes available. However, there is a unique class of exoplanets called hot Jupiters which are Jupiter-sized exoplanets orbiting closely to their host stars on typical periods of only a few days (Fortney et al., 2021). The close proximity means they are all tidally locked with a permanent day and night side (Goldreich and Soter, 1966; Guillot et al., 1996; Komacek et al., 2017). Their host stars also blast them with intense electromagnetic radiation which can heat up their dayside atmospheres to over 2000K (Fu et al., 2021). This extreme environment is nothing like Earth and we certainly do not expect any life we know to be found on hot Jupiter. However, their large inflated radius and high equilibrium temperature make them the best targets for atmospheric study. Hot Jupiters are ideal laboratories to test our atmospheric models of highly irradiated tidally locked planets. They are also important stepping stones to developing remote sensing techniques for transiting exoplanet atmospheres.

1.3.0.1 What do we know about hot Jupiter atmospheres?

As the earliest type of exoplanet that we have been able to do atmosphere characterization (Charbonneau et al., 2002), most of what we know about exoplanet atmospheres are from hot Jupiters. On the relatively cooler ones ($\sim 1000 - 2000\text{K}$), we have detected water (Deming et al., 2013; Kreidberg et al., 2015; Spake et al., 2020; Wakeford et al., 2017), carbon-dioxide (Line et al., 2021), helium (Kirk et al., 2020; Spake et al., 2018), alkali metals (Charbonneau et al., 2002; Nikolov et al., 2015) and aerosols (Fu et al., 2021; Sing et al., 2016). Methane and

potassium are still yet to be found despite predictions from models (Kreidberg et al., 2018b). For the ultra-hot Jupiter ($>2000\text{K}$), we have detected heavy metals (Ehrenreich et al., 2020; Fu et al., 2021; Lothringer et al., 2022; Sing et al., 2019) and H- (Arcangeli et al., 2018; Mansfield et al., 2020) but the search for important optical absorbers TiO/VO still remains elusive.

Hot Jupiter atmospheres are nothing we have seen on any solar system planets and they strongly depend on the temperature. Although we expect composition variation such as C/O ratio and metallicity (Madhusudhan, 2012; Wakeford et al., 2017) will also have a significant effect on their atmosphere, we do not yet have the measurements precise enough to test those hypothesis.

1.4 How do we study hot Jupiter atmospheres?

All the exoplanets discovered to date can be largely classified into two categories of transiting and non-transiting planets. While transiting planets have been mostly found through the ground (e.g. WASP, HAT, KELT) and space-based (e.g. Kepler, TESS) photometric monitoring campaigns of nearby stars, non-transiting planets were discovered through radial velocity, direct imaging, and microlensing surveys. For non-transiting planets, we can access their atmospheres using direct high contrast imaging (Currie et al., 2022) with coronagraph or interferometry by removing the host starlight and measuring the light from the planet's atmosphere. This technique certainly holds great promise for future investigation of Earth-like planets around sun-like stars, we do not yet have such instrument capabilities. Therefore, transiting planets still remain mostly accessible for atmospheric studies.

When a planet transits in front of the host star, we can measure its transit depth which corresponds to the planetary radius (Figure 1.1) (Sing, 2018). If the planet has an atmosphere, its

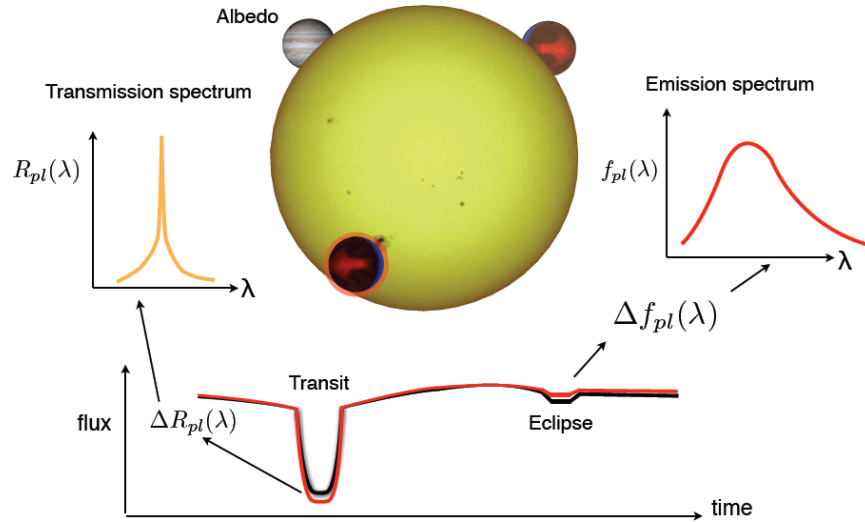


Figure 1.1 Illustration of the transmission and emission spectroscopy techniques (Sing, 2018).

radius will be wavelength-dependent depending on the optical depth of its terminator region at a given wavelength. By measuring the transit depth of the planet as a function of wavelength, we can determine the atmospheric composition of the planetary terminator region. This technique is called transmission spectroscopy.

If a planet transits in front of a star, it will also likely eclipse behind a star. When the planet hides behind the star, we can measure the stellar flux alone (Figure 1.1). Then by subtracting the stellar flux from the combined star and planet dayside flux measured just before and after the secondary eclipse, we can obtain the dayside emission spectrum of the planet. The emission spectrum probes deeper into the atmosphere relative to the transmission spectrum due to the different observing geometry. This technique is called secondary eclipse spectroscopy.

These are the two main techniques used for my thesis work. By combining the two, we can gain insights into the thermal structure and chemical composition of hot Jupiter atmospheres across a wide range of pressure levels from the terminator to the dayside.

1.4.1 How we study hot Jupiter atmospheres with space-based telescopes

My thesis focuses on using space telescopes to characterize exoplanet atmospheres. Space-based observatories are free from the contamination of telluric features which allows for high precision measurements of exoplanet atmospheres. This is especially important in the longer wavelength where the thermal emission from the Earth's atmosphere becomes to dominate. All the exoplanetary spectra presented in this thesis are collected using HST and Spitzer which together cover from optical to infrared in wavelength.

Observing with space telescopes come with their unique challenges which vary between instruments. HST orbits the Earth every ~ 90 minutes and usually only about half of the time it is able to collect science data due to the Earth occultation. Therefore each orbit could have different systematics due to the thermal profile changes of the telescope between orbits (Deming et al., 2013; Sing et al., 2008). The telescope pointing also drifts during the observation. Although the shift is usually on sub-pixel levels, it changes the incoming flux distribution among different pixels. Since each pixel has a slightly different quantum efficiency, this leads to changing in the total counts. To correct for this effect, the shifts of the PSF from each exposure can be calculated by interpolating each frame and fit for the shifts between them. Then the shifts are scaled using a polynomial and fitted to the light curve counts. The polynomial can be linear, 2nd, 3rd or even higher order depending on the levels of the pixel drifts and non-linearity in the pixel response (Fu et al., 2021; Sing et al., 2015). In addition, jitter information from the engineering files of the telescope have also been shown to be useful in correcting for systematics. Jitter files record the location and orientation of the telescope during the observation and are correlated to the final counts (Sing et al., 2019).

Each detector also has their own systematics and this is more severe for infrared detectors such as HST WFC3 infrared channel detector. It is a $1k \times 1k$ HgCdTe which suffers from charge trapping effects. After photons are absorbed by the photodiodes free charge carriers are produced which are then emptied out via the electric potential gradient (Zhou et al., 2017). However, during this process, some free charge carriers are left behind trapped in the detector. This effect leads to lower signal to be counted for the exposure. During the next exposure the same process happens again but less free charge carriers get trapped due to the reducing number of charge traps available. This continue to take place until all the charge traps are filled and the counts reach a steady level. Therefore the time series flux measurement exhibits a ramp-like shape (Deming et al., 2013) for the initial exposures. The detector is reset during the Earth occultation when the telescope is not observing and the same charge trapping pattern appear again for the new orbit.

Spitzer also suffers from infrared detector systematics specifically the intra-pixel sensitivity variations (Deming et al., 2015). The quantum efficiency varies within the pixels of the Spitzer InSb detector. Combined with the pointing fluctuations this leads to large systematics for time-series observations. This effect is the strongest for the $3.6 \mu m$ channel where the intra-pixel sensitive map varies in time (May and Stevenson, 2020). Multiple techniques have developed to correct for the Spitzer systematics (Deming et al., 2015; May and Stevenson, 2020; Shporer et al., 2014; Stevenson et al., 2014a) but there have not been a unified and consistently reliable approach to reduce the Spitzer $3.6 \mu m$ datasets (Ingalls et al., 2016). The future JWST observations will allow us to confirm our current Spitzer observation.

Chapter 2: Transit and Eclipse Spectroscopy of the Strongly Irradiated Giant Exoplanet WASP-76b

2.1 Overview

Ultra-hot Jupiters with equilibrium temperature greater than 2000K are uniquely interesting targets as they provide us crucial insights into how atmospheres behave under extreme conditions. This class of giant planets receives intense radiation from their host star and usually has strongly irradiated and highly inflated atmospheres. At such high temperature, cloud formation is expected to be suppressed and thermal dissociation of water vapor could occur. We observed the ultra-hot Jupiter WASP-76b with 7 transits and 5 eclipses using the HST and Spitzer for a comprehensive study of its atmospheric chemical and physical processes. We detected TiO and H₂O absorption in the optical and near-infrared transit spectrum. Additional absorption by a number of neutral and ionized heavy metals like Fe, Ni, Ti, and SiO help explain the short wavelength transit spectrum. The secondary eclipse spectrum shows muted water feature but a strong CO emission feature in Spitzer's 4.5 μm band indicating an inverted temperature pressure profile. We analyzed both the transit and eclipse spectra with a combination of self-consistent PHOENIX models and atmospheric retrieval (ATMO). Both spectra were well fitted by the self-consistent PHOENIX forward atmosphere model in chemical and radiative equilibrium at solar metallicity, adding to

the growing evidence that both TiO/VO and NUV heavy metals opacity are prominent NUV-optical opacity sources in the stratospheres of ultra-hot Jupiters.

2.2 Introduction

Transiting exoplanets can offer us detailed insights into their atmospheres during the transit and eclipse phases. When transiting in front of the parent star, the limb of planetary atmosphere filters out a portion of the starlight. The amplitude of that effect varies with wavelength, depending on the composition of the atmosphere. The spectral features of the upper exoplanetary atmosphere (~ 1 mbar) are thereby imprinted onto the stellar light. During the secondary eclipse, the planet passes behind the host star, and deep (10-100 mbar) thermal emission of the atmosphere can be measured via the total flux difference before and after the eclipse. Both techniques have been used extensively in recent years to characterize exoplanetary atmospheric properties like chemical composition ([Kreidberg et al., 2014b](#)), thermal structure ([Stevenson et al., 2014b](#)), aerosols ([Sing et al., 2016](#)) and hydrodynamical escape ([Sing et al., 2019](#); [Spake et al., 2018](#)).

Most detectable exoplanetary spectral features produce only a few hundred part per million (ppm) of signal over broad wavelength ranges ([Deming et al., 2013](#); [Stevenson et al., 2014a](#); [Wakeford et al., 2017](#)). High precision photometry is required to capture these small variations in the depth of transit and eclipse light curves. Indeed, since the first detection of sodium absorption in HD 209458b made by ([Charbonneau et al., 2002](#)) using the Hubble Space Telescope (HST), many atmospheric studies have used space telescopes, notably HST and Spitzer. Some recent ground based observations ([Allart et al., 2018](#); [Ehrenreich et al., 2015](#); [Kirk et al., 2020](#)) have also successfully detected various atmospheric features such as water, sodium and helium. Chemical

species that absorb in the very high atmosphere (~ 10 scale heights) can cause a few thousand ppm excess transit depth within the narrow range of the absorption line profile core, which is often detectable from the ground despite additional noise from telluric contamination and changing weather conditions.

Hot Jupiters are especially targets of interest for atmospheric characterization due to their inflated and highly irradiated atmospheres which produce strong detectable spectral features (Fortney et al., 2008). Over a dozen hot Jupiters Sing et al. (2016); Tsiaras et al. (2018) have been studied in detail over the past decade and the results are highly intriguing yet complex (Fu et al., 2017). While some planets exhibit prominent water absorption features (Deming et al., 2013; Wakeford et al., 2017), others show significant aerosols presence in the upper atmosphere (Fu et al., 2021). Inverted temperature pressure profiles have also been observed (Evans et al., 2017; Haynes et al., 2015) caused by optical absorbers such as TiO/VO (Fortney et al., 2008). In the ultra-hot ($>2000\text{K}$) Jupiters, even water can be disassociated and H- becomes an important opacity source (Arcangeli et al., 2018; Fu et al., 2021; Lothringer et al., 2018; Parmentier et al., 2018).

WASP-76b is a unique target with an equilibrium temperature of 2200K and a puffy atmosphere. Recent work has shown the existence of atomic sodium absorption (von Essen et al., 2020) and evidence for atomic iron condensing on the day-to-night terminator (Ehrenreich et al., 2020). Here we present observations and modeling results that show heavy metals, H₂O and TiO absorption in the transmission spectrum. The eclipse emission spectrum shows CO emission feature in the Spitzer's 4.5 μm band with an inverted temperature pressure profile.

WASP-76b transit observations

	Grism/Filter	Visit 1	Visit 2	GO Program ID	PI
HST STIS	G430L	2016-11-16	2017-01-17	14767	López-Morales & Sing
HST STIS	G750L	2017-02-19		14767	López-Morales & Sing
HST WFC3	G141	2015-11-26		14260	Deming
Spitzer	IRAC 3.6	2017-05-04	2018-04-22	13038	Stevenson
Spitzer	IRAC 4.5	2017-04-16		13038	Stevenson

WASP-76b eclipse observations

	Grism/Filter	Visit 1	Visit 2	GO Program ID	PI
HST WFC3	G141	2016-11-03		14767	López-Morales & Sing
Spitzer	IRAC 3.6	2016-03-22		12085	Deming
Spitzer	IRAC 3.6	2017-05-04	2018-04-22	13038	Stevenson
Spitzer	IRAC 4.5	2016-04-01		12085	Deming

Table 2.1 A list of our 7 transit and 5 eclipse observations of WASP-76b.

2.3 Observations and Data Analysis

We observed a total of 7 transits and 5 eclipses of WASP-76b with HST and Spitzer in multiple filters (Table 3.1) ranging from 0.29 to 4.5 μm . HST STIS/WFC3 and Spitzer IRAC all have unique detector systematics that require specialized data analysis pipelines (Deming et al., 2015, 2013; Nikolov et al., 2014; Wakeford et al., 2017). Fortunately, as the main instruments used to characterize exoplanetary atmospheres in the past decade, robust custom data analysis methods have been developed to extract near photon-limited noise spectra (Zhou et al., 2017).

2.3.1 Companion Star & EXOFASTv2 Fit

WASP-76A has a companion star. WASP-76B was first discovered by (Wöllert and Brandner, 2015) through lucky imaging with a separation of $0.425'' \pm 0.012''$ and position angle of $216.9^\circ \pm 2.93^\circ$. Due to the small separation, light from WASP-76B is well mixed with WASP-76A in our HST spatial scan spectrum which causes a dilution effect on the extracted planet spectrum

(Crossfield et al., 2012). To correct for this dilution effect, the companion stellar spectral type needs to be determined, and the extra flux contribution removed. The temperature of WASP-76A is $6250 \pm 100\text{K}$ (West et al., 2016) and the updated distance from GAIA is 195.31 ± 6.03 parsecs. There are a total of three spatially resolved images of the WASP-76 system in the archive, taken with different filters (Table 3.1) using the Space Telescope Imaging Spectrograph (P.I.s: David Sing & Mercedes López-Morales), and Keck-AO with NIRC2 (P.I.: Brad Hansen), all shown in Figure 2.1. To determine the spectral type of WASP-76B, we performed a two-component SED fit (Rodríguez et al., 2019) for WASP-76 and we determine the radius and temperature of WASP-76B to be $R_{\star} = 0.795 \pm 0.055R$ and $T_{eff} = 4850 \pm 150\text{K}$ which we then used as the prior in a EXOFASTv2 (Eastman et al., 2019) global analysis. Within the EXOFASTv2 fit, the host star parameters are constrained using the MESA Isochrones and Stellar Tracks (MIST) stellar evolution models. For the EXOFASTv2 fit, we included six new light curves (Fig. 2.16) from EulerCAM (Ehrenreich et al., 2020), Hazelwood and MVRC observations in addition to the transit and RV data used in the discovery paper (West et al., 2016) to refine and update the system ephemeris.

With the best-fit radius and effective temperature for both WASP76A and WASP76B, we can then use PHEONIX stellar models to calculate the flux contribution from both stars and the dilution effect of transit and eclipse depth can be corrected as follows:

$$\text{Corrected depth} = \text{Measured depth} * \left(1 + \frac{F_B}{F_A}\right)$$

where F_B and F_A are the flux contribution from the companion and the primary star at a given wavelength range. Since the companion star is spatially resolved at different levels with being

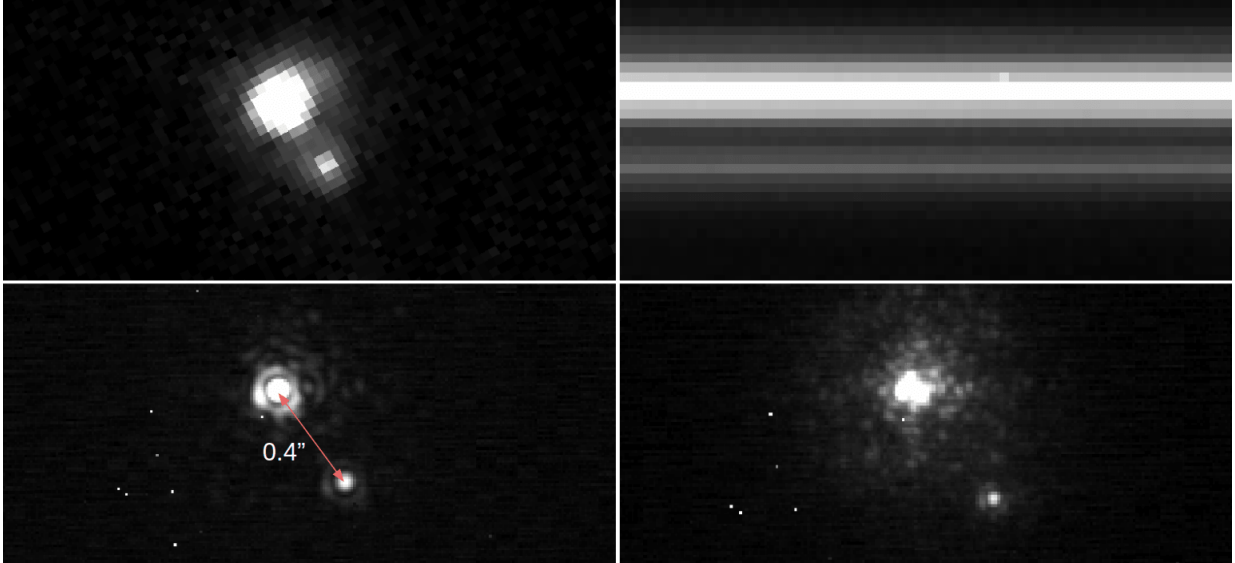


Figure 2.1 Resolved images of spectrum of the WASP-76 binary system, obtained with HST STIS F28X50LP (Top Left), G750L spectrum (Top Right), Keck-AO NIRC2 Brackett-gamma (Bottom Left) and J-Cont (Bottom Right).

mostly resolved in STIS spectra while completely blended in at Spitzer bands, we purposefully choose larger aperture sizes at all wavelength when extracting stellar spectra to ensure all companion flux contributions are included. Finally, the dilution is applied across the entire transit and eclipse spectra for consistent correction.

To propagate the uncertainties on the effective temperature of both stars into dilution factors and the final planet spectrum, we adopted the bootstrapping method used in (Stevenson et al., 2014a) by generating 10000 PHOENIX stellar models for each star with T_{eff} randomly sampled from a Gaussian distribution based on the T_{eff} uncertainty. By calculating the corresponding dilution factors for each PHOENIX model pair, we obtain a 10000 sample size distribution of dilution factors at each wavelength bin. The final dilution factors are the median values of each distribution and the uncertainties will be the corresponding one sigma values which are then propagated into the reduced planet transit and eclipse spectra.

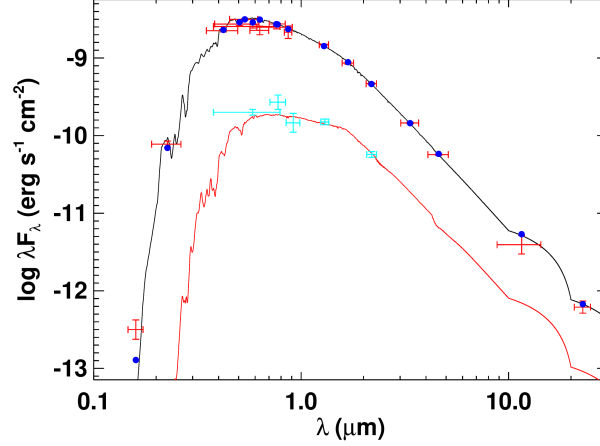


Figure 2.2 Two-component SED fit for WASP-76A (black) and WASP-76B (red) with the blue points as integrated fluxes and cyan points as spatially resolved flux measurements.

	STIS F28X50LP	i band	z band	J-Cont	Br gamma
Wavelength range (μm)	0.54 - 1	0.662 - 0.836	0.777 - 1.097	1.203 - 1.223	2.024 - 2.292
Δ mag	2.57	2.51	2.85	2.49	2.28
Δ mag error	0.02	0.25	0.33	0.01	0.01

Table 2.2 Measured flux ratio between WASP-76A and WASP-76B in 5 different bands from HST STIS, [Wöllert and Brandner \(2015\)](#) and KECK-AO NIRC2.

2.3.2 HST STIS G430L & G750L

We observed WASP-76b in transit with 2 visits using HST/STIS G430L and 1 visit using the G750L grating (Table 3.1). Both gratings were observed using the ACCUM mode with the 50X2 aperture to minimize any slit losses. CCD subarray of 128 x 1024 pixels was used to reduce readout time and maximize observing efficiency. Each frame has an exposure time of ~ 148 seconds and each orbit has ~ 16 exposures. The combination of these two gratings provided a complete wavelength coverage from 2900 to 10300 Å. One prominent source of systematics in STIS light curves comes from the orbital motion of the telescope during the observations ([Nikolov et al., 2014](#)). As the telescope orbits between the day side and night side of the Earth, it experiences thermal expansion and contraction. This effect manifests as a varying observed flux

as a function of telescope orbital phase.

Our data analysis process follows the standard methodology detailed in [Sing et al. \(2011\)](#) and [Nikolov et al. \(2014\)](#). We fit the STIS transit light curves using a combination of transit and instrument systematics models. The transit model is based on the analytic formula developed by [Mandel and Agol \(2002\)](#), and the systematics model is a fourth-order polynomial of the telescope orbital phase, a linear time term and wavelength shift for each frame. Orbital inclination and a/R_{star} are both fixed at the best-fit values derived in this paper during the fit. For limb darkening we calculate the relevant coefficients with ATLAS stellar models ([Jack et al., 2009](#)) in the same way as detailed in [Nikolov et al. \(2014\)](#). The raw, corrected light curves and corresponding residuals for all three visits are shown in Figures [2.6](#), [2.7](#) and [2.8](#).

2.3.3 HST WFC3 G141

We observed both transits and eclipses using HST/WFC3 G141 in spatial scan mode to maximize photon-collecting efficiency ([Deming et al., 2013](#)). All frames used SPARS10 and NSAMP=16, with an exposure time of ~ 104 seconds, and a forward and backward scan to maximize observing efficiency. Due to occultation of the telescope by the Earth, a ~ 45 min gap exists between every HST orbit. In total, there are 5 orbits per visit and ~ 19 spectra per orbit. Two orbits are pre-transit, two are in-transit, and one is post-transit.

The automatic CalWF3 pipeline does not include spatial scan mode, therefore additional processing is required before extracting the 1D spectra. We followed the standard procedures of background subtraction and energetic particle removal by flagging outliers relative to the median value along the vertical scan direction. Next, we corrected for the wavelength shift

of each spectrum in the horizontal direction. To calculate the sub-pixel level shifts between each frame, we first summed each frame in the vertical direction to obtain a 1D spectrum and normalized it by its own median flux. Then we used `scipy.interpolate.interp1d` function to interpolate normalized flux of each 1D spectrum in the wavelength direction relative to its pixel positions. Next we applied sub-pixel shifts to each 1D spectrum relative to a reference spectrum and calculated the shifts by minimizing the normalized flux differences between them. Finally we applied the calculated shifts on every 1D spectrum to obtain the wavelength shifts corrected 1D spectra. The hydrogen Paschen-beta line at $1.28 \mu\text{m}$ in the star is used to establish the zero-point of the wavelength calibration.

HST/WFC3 time series spectra often exhibit a ramp-like systematic shape when observing bright stars in high-cadence (Wilkins et al., 2014). This effect is attributed to charge trapping in the WFC3 HgCdTe infrared detector (Kreidberg et al., 2014a; Zhou et al., 2017). As initial photons arrive at the beginning of each orbit, some charge carriers can be trapped by impurities in the detector and cause lower readout signals. When all available traps are filled during the orbit, the measured signals asymptotically approach a constant level (Fig 2.4). The double-ramp shape per orbit is due to differences in exposure timing and telescope pointing between forward and backward scan. The timings for when each pixel receives light are different in forward and backward scan, and that can affect the ramp shape. Moreover, the illumination pattern on the pixel grid is slightly different from forward to backward scan. Since each pixel has a different number of charge traps, a constant offset in measured flux can occur when different portions of the detector are illuminated by forward and backward scan.

2.3.3.1 Satellite contamination

During the analysis of the transit data, we discovered two frames (Fig 2.3) that were contaminated by defocused Earth-satellite crossing events. The first satellite crosses the frame diagonally (see Fig 2.3(a)) leaving a broad bright strip which contaminates the spectrum in a wavelength-dependent fashion. The extra photons from the satellite significantly distort the ramp shape of the third orbit's white light transit curve (see Fig 2.4), because they rapidly populate large number of charge traps. This causes the decay-down as opposed to the ramp-up shape as extra persisting signals were measured in all subsequent frames of the orbit. The diagonal crossing of the satellite results in more contamination on the shorter wavelength end of the spectrum than the longer wavelength end. Consequently, the white light transit curve cannot be used as a template to correct for all wavelength channels. We decide to discard all remaining frames in the third orbit after the first satellite crossing. The second satellite crossing is much fainter and had negligible effect on the subsequent spectra in the fourth orbit, so we only discard the frame with the second satellite itself.

2.3.3.2 Ramp correction using RECTE

After removing satellite-contaminated exposures, we use the Ramp Effect Charge Trapping Eliminator (RECTE) algorithm developed by Zhou et al. (2017) to mitigate the ramp effect. RECTE is a physically motivated model based on detector charge trapping properties. For more detailed description of RECTE see (Zhou et al., 2017) and the online documentation¹. One major advantage of RECTE compared to other ramp-effect correcting methods based on template and

¹<https://recte.readthedocs.io>

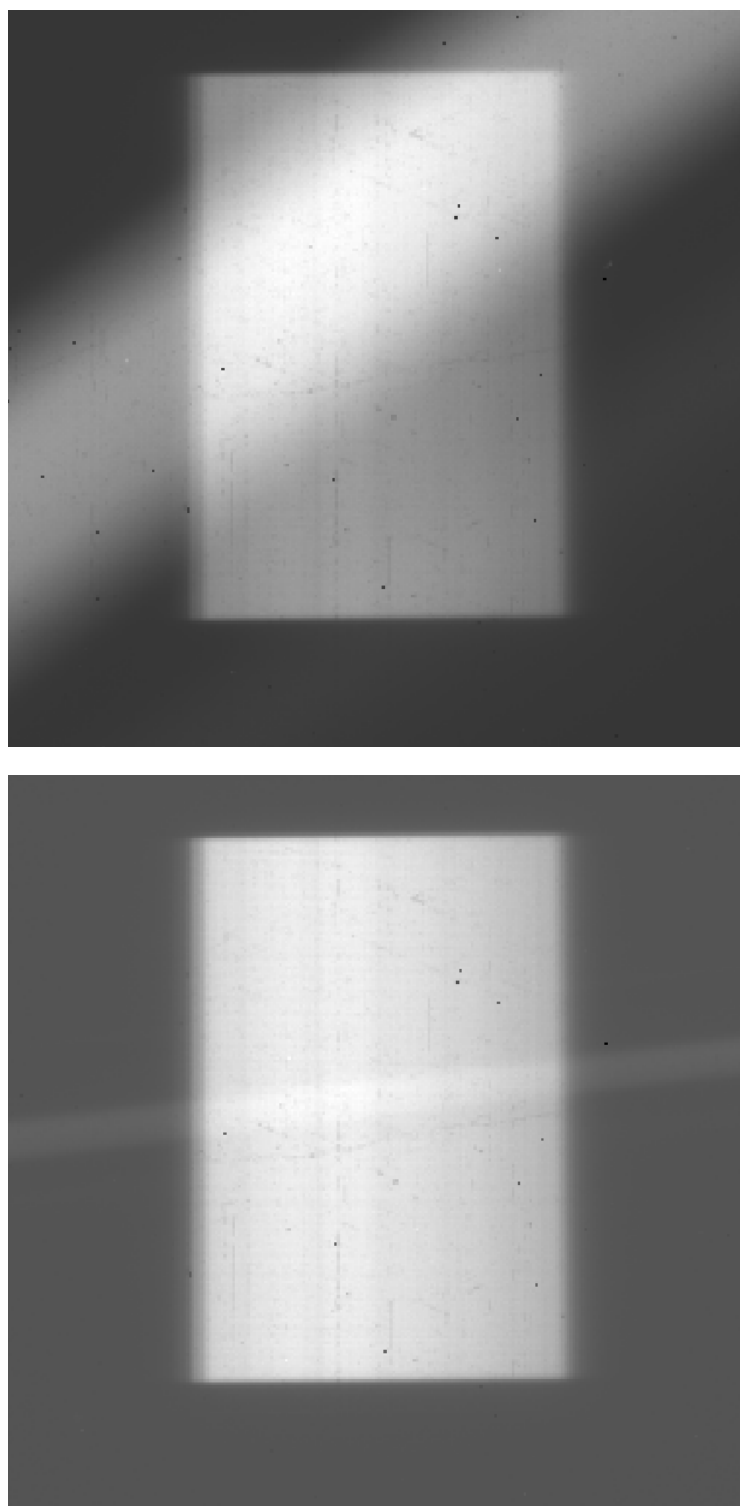


Figure 2.3 Satellite crossing contamination frames. Spatial scan is in the vertical direction and wavelength is in the horizontal direction.

fitting of empirical functions is the capability to correct for the first orbit of the observations. The first orbit has often been discarded in past analyses due to its extreme ramp shape comparing to the subsequent four orbits (Deming et al., 2013). Recovering that additional out-of-transit orbit allows us to better determine the baseline flux and obtain more precise transit depth values.

We used the BATMAN light curve model (Kreidberg, 2015) in combination with RECTE to measure the transit depth at each spectral bin. Orbital inclination and a/R_{star} were both fixed at the best-fit values derived in this paper during the fit. We calculated the relevant limb darkening coefficients with ATLAS stellar models the same way as the STIS dataset. There are five free parameters from RECTE: intrinsic flux (f), slow ($E_{s,tot}$), and fast ($E_{f,tot}$) charge traps populations, slow (η_s) and fast (η_f) charge trapping efficiency. Together they model the varying exponential ramp effect from the charge trapping process in the HST/WFC3 detectors. The slight vertical shift from forward and backward scans cause an observed flux difference between adjacent (Fig 2.4) exposures which is corrected through fitting a constant offset value. There is also a linear visit-long slope which is fit with two slope coefficients for forward and backward scans. Given our re-fit of the orbital parameters that determine the shape of the transit, the BATMAN fit has two free parameters, the transit center time and transit depth. Therefore, a total of 10 free parameters were used in the MCMC to fit for the white light transit. The transit center time from the white light fit is adopted when subsequently fitting transit curves at each wavelength.

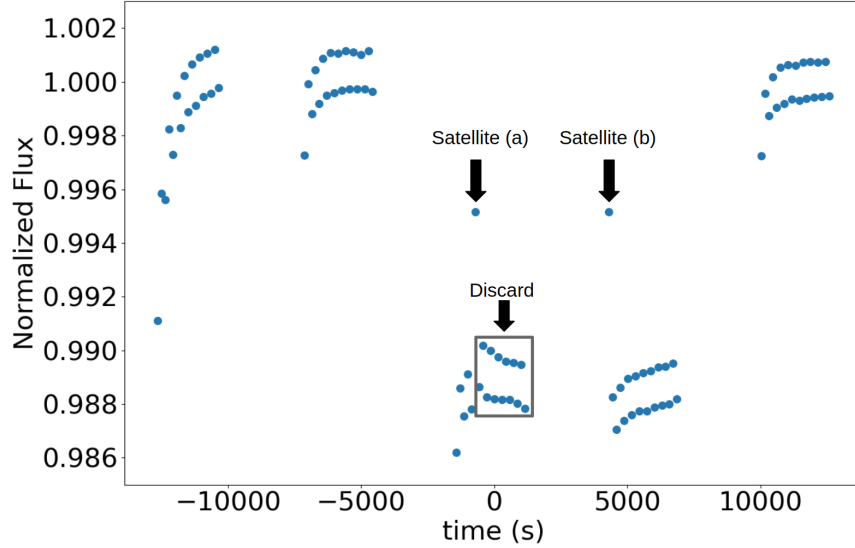


Figure 2.4 The effect of satellite crossing contamination on the white light transit curve. The two satellite contaminated data points have very high flux and were set to fixed values to show the timing of the events. Satellite crossing (a) was significantly more severe than satellite crossing (b) and distorted the ramp shape for the third orbit. We decided to discard the frames after satellite crossing (a), see text. The upper and lower sets of points are due to spectra vertical shifts during the forward versus backward scan.

2.3.4 Spitzer IRAC

We observed transits and eclipses of WASP-76b with Spitzer at 3.6 and 4.5 μm (Table 3.1). Unlike HST, Spitzer is able to continuously observe targets for the entire transit and eclipse duration. One eclipse at each of 3.6 and 4.5 μm are reported by Garhart et al. (2020), and we do not re-analyze those data here. We here analyze the transit data, and two additional eclipses at 3.6 μm from program 13038. Our analysis of two additional eclipses at 3.6 μm followed the exact same procedures used by Garhart et al. (2020), in fact the same codes (implemented by D.D.). The new eclipse depths are included in Table 2.3.

Spitzer’s primary systematic effect comes from intra-pixel sensitivity variations coupled to pointing jitter, overlaid by temporal ramps. We correct for this combination of systematic effects using the pixel-level decorrelation (PLD) technique developed by Deming et al. (2015), with

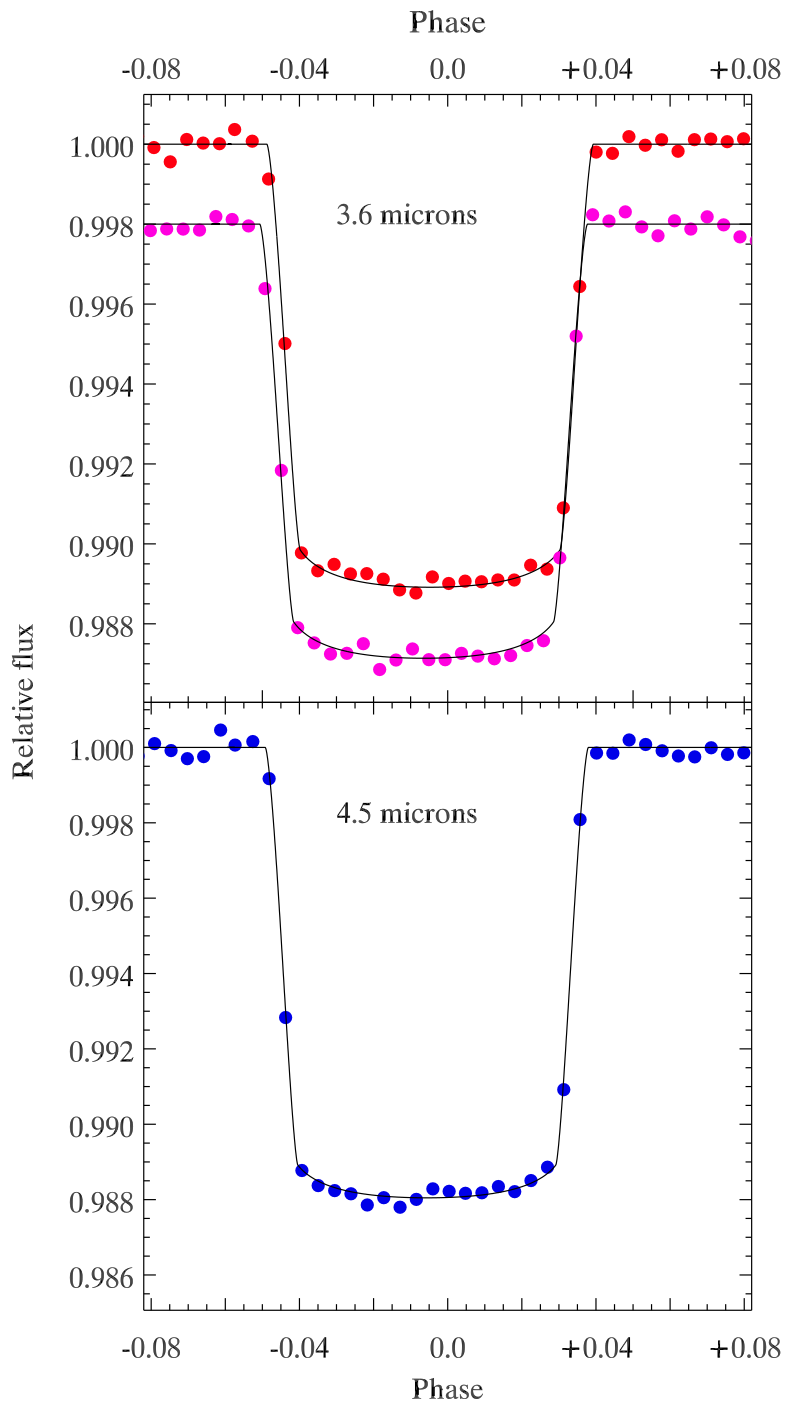


Figure 2.5 Spitzer transit light curves in 3.6 and 4.5 μm after systematic correction.

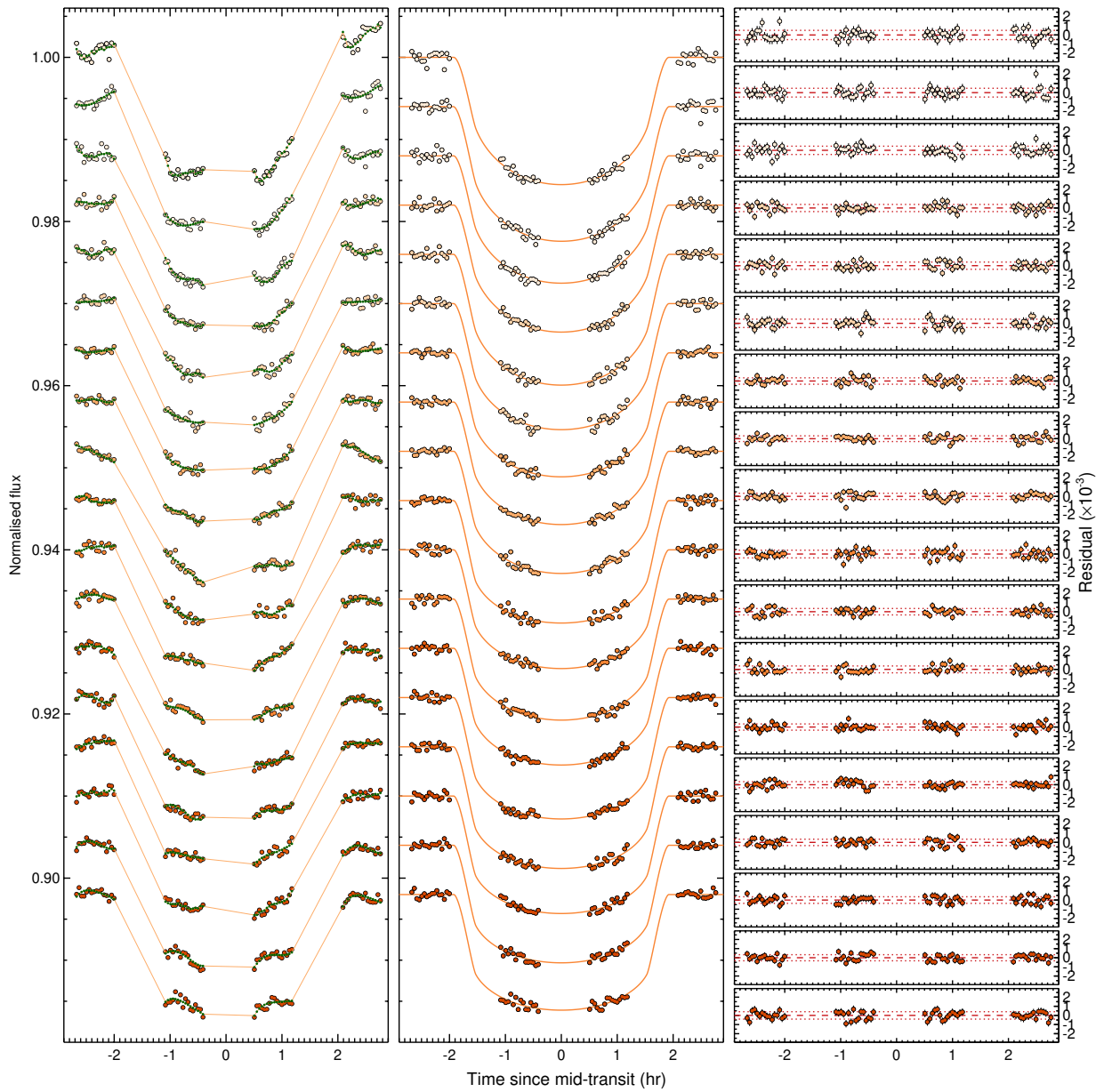


Figure 2.6 HST STIS G430L visit one light curves for each spectral channel. Left panel: raw light curves with evident systematics as a function of telescope orbital phase. Middle panel: Detrended light curves overplotted by the best-fitting transit models. Right panel: corresponding residual (data minus fit) for each spectral channel with the dotted lines showing the 1σ standard deviation.

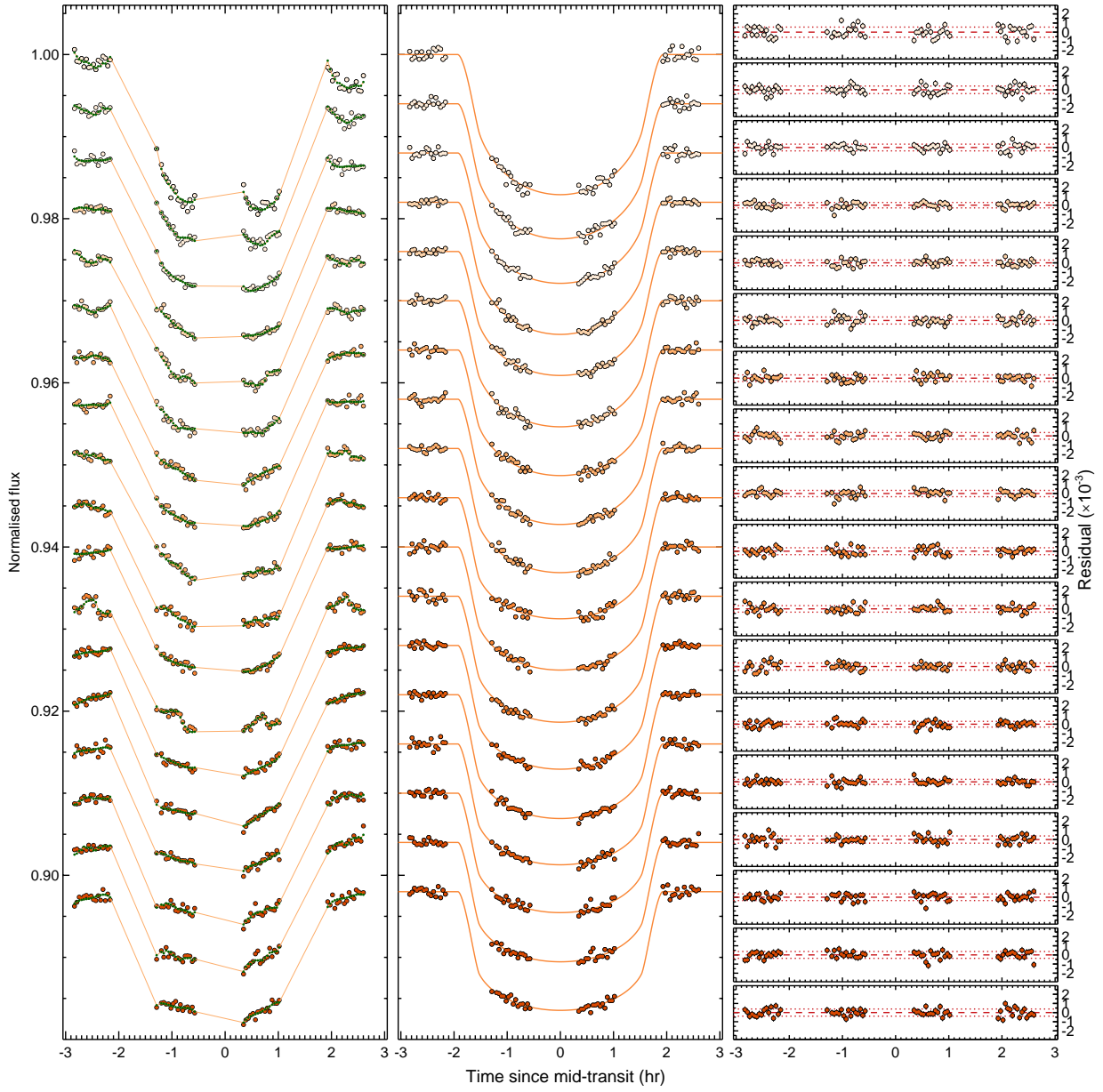


Figure 2.7 Same as Fig 2.6 but for HST STIS G430L visit 2.

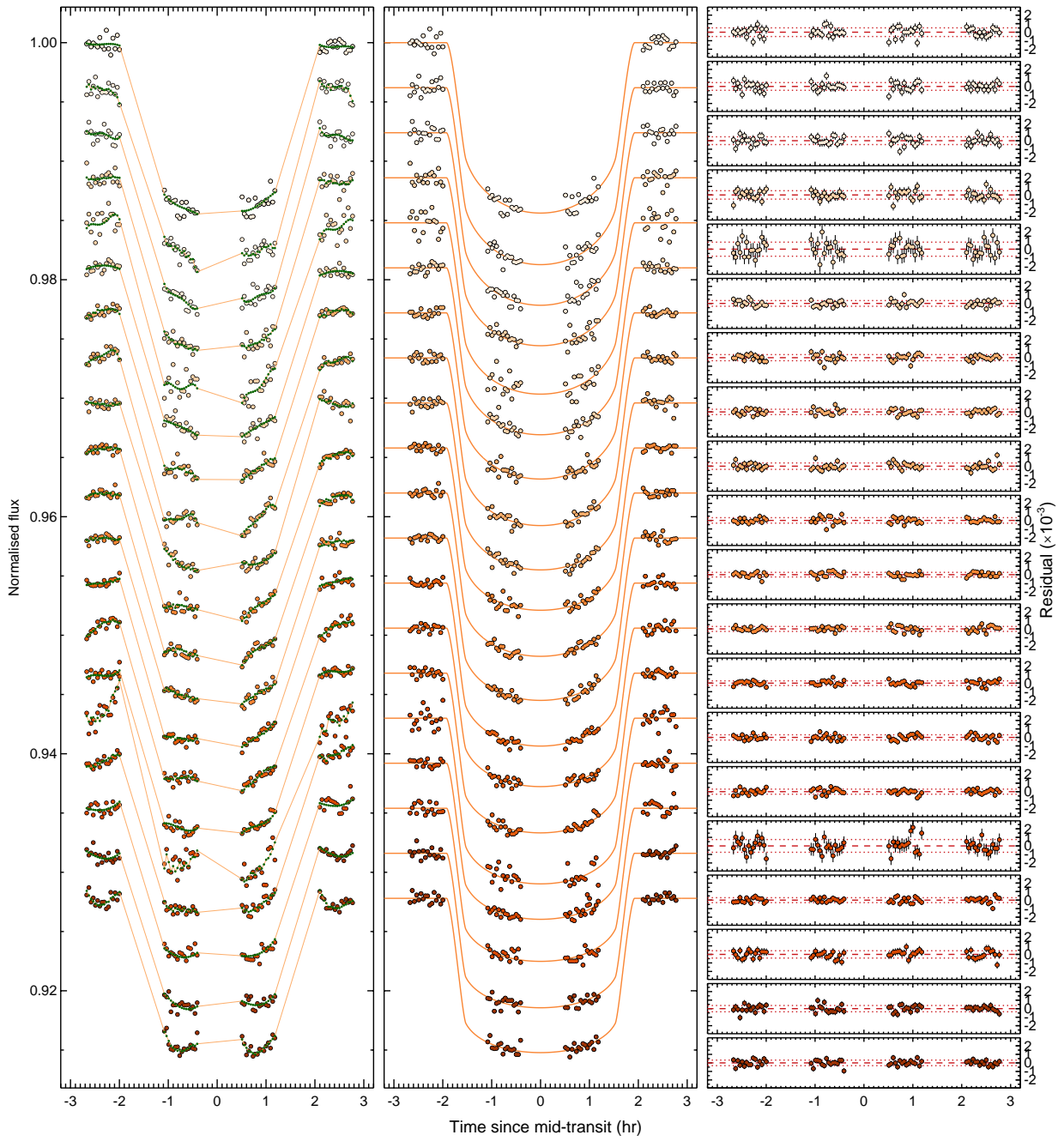


Figure 2.8 Same as Fig 2.6 but for HST STIS G750L.

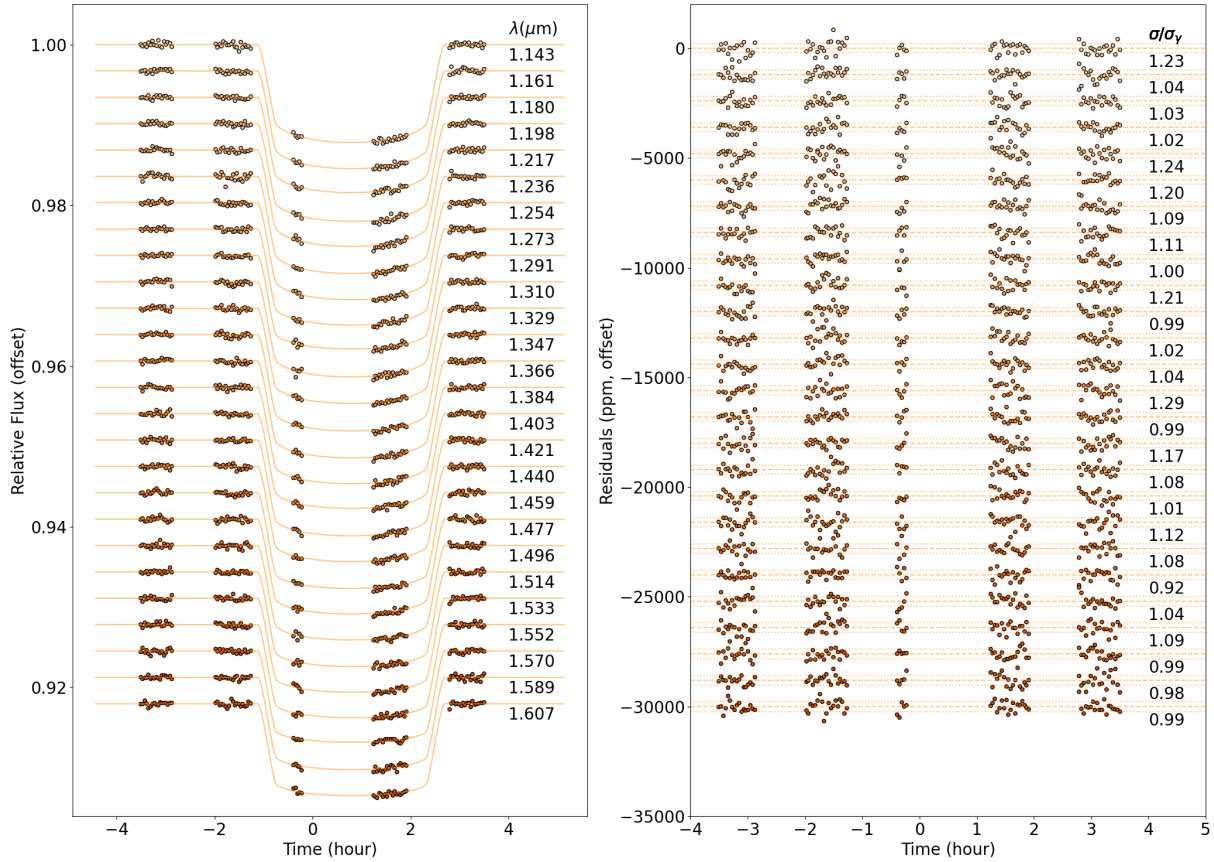


Figure 2.9 HST WFC3 G141 spectral bin transit lightcurves after ramp-effect correction using RECTE (left) and corresponding residuals (right). The dotted lines in the residual plot represent expected photon noise.

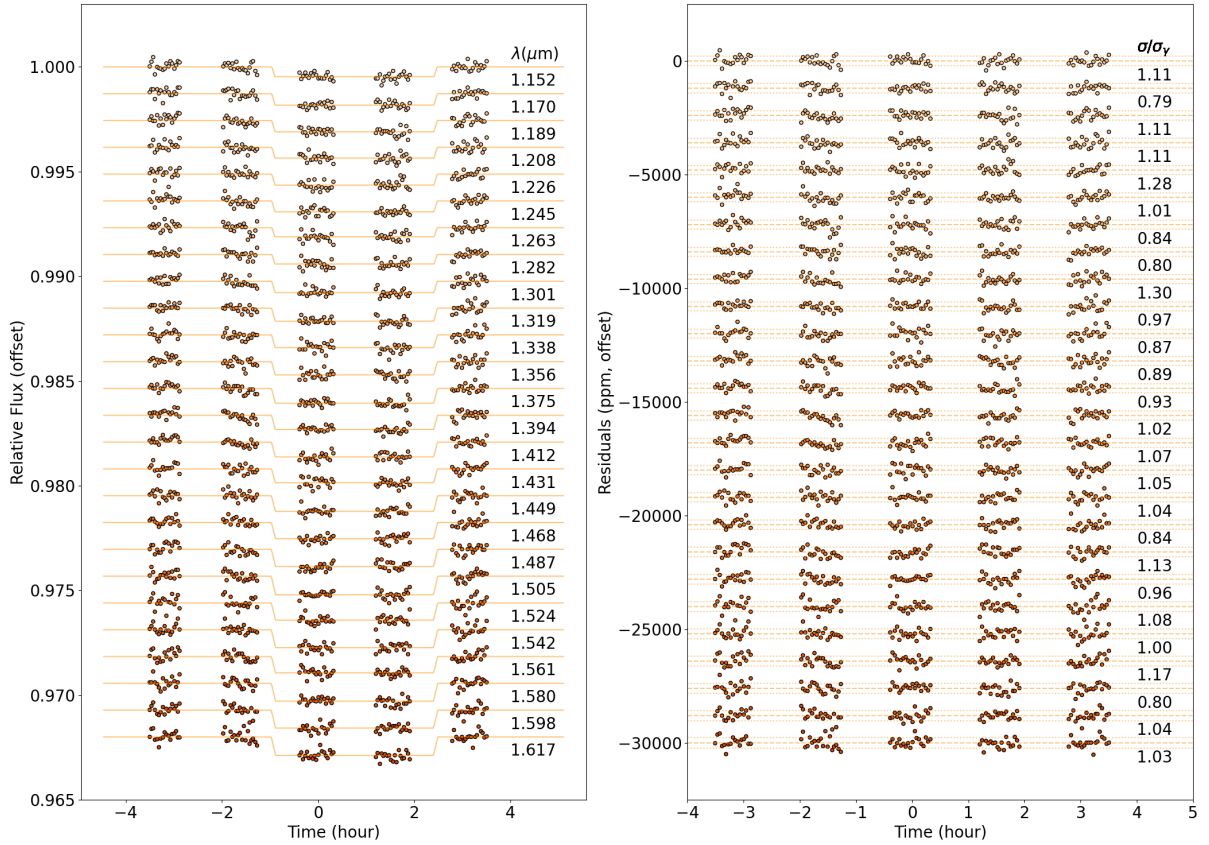


Figure 2.10 HST WFC3 G141 spectral bin eclipse light curves after ramp-effect correction using RECTE (left) and corresponding residuals (right). The dotted lines in the residual plot represent expected photon noise.

the implementation of the fit being the same as described by [Garhart et al. \(2020\)](#). PLD takes advantage of the total flux conservation within the aperture containing the star, and utilizes the relative flux contribution of individual pixels as basis vectors in the fit. This technique eliminates the need for finding the centroid position of the star while being capable of effectively removing red noise and flat-fielding inaccuracies.

Our solutions for the Spitzer transit depths incorporate quadratic limb darkening coefficients calculated for the Spitzer bands by [Claret et al. \(2013\)](#). These produce excellent agreement with the observed transit curves. Given that limb darkening is a minimal effect at Spitzer’s wavelengths, we adopt the Claret coefficients without further perturbation. Our initial procedure was to also freeze the orbital parameters at previously-determined values, since our experience with other data shows that this simple method usually produces excellent agreement with the shape of Spitzer’s observed transit curves. However, atmospheric characterization can be sensitive to alternate treatments of the orbital parameters ([Alexoudi et al., 2018](#)). Given also that we find some differences between the transit depths observed at 3.6- versus 4.5 μm , and between two transits at 3.6 μm , we explored other treatments of the orbital parameters. We used independent Gaussian priors for the two parameters that most affect the transit shape (orbital inclination and a/R_s), based on the discovery results from [West et al. \(2016\)](#). Those fits produced transit depths that differed minimally from fits that froze the orbital parameters at the [West et al. \(2016\)](#) values. Those differences (orbital priors minus orbital freeze), were 157 and 34 ppm in R_p^2/R_s^2 for the two transits at 3.6 μm , and -93 ppm at 4.5 μm . Our best-fit values of inclination and a/R_s differed from [West et al. \(2016\)](#) by less than 1σ . We also explored freezing the orbital parameters at the values derived in this paper, noting that our values for inclination and a/R_s are within 1σ of [West et al. \(2016\)](#). Those transit depths differed from our initial values by 84 and 3 ppm at 3.6 μm , and

Table 2.3 Transit and eclipse times and depths for WASP-76b in the Spitzer bands. These are "as observed" transit/eclipse depths, not corrected for dilution by the companion star. The two eclipses from GO 12085 (PI: Deming) were published in (Garhart et al., 2020) and therefore not included here.

Wavelength	Event	BJD(TDB)	Depth (ppm)
3.6 μm	Transit	2457877.915709 \pm 0.000163	10496 \pm 66
3.6 μm	Transit	2458230.840367 \pm 0.000145	10315 \pm 49
4.5 μm	Transit	2457859.815112 \pm 0.000181	11399 \pm 82
3.6 μm	Eclipse	2457877.01558 \pm 0.00067	2883 \pm 96
3.6 μm	Eclipse	2458229.93999 \pm 0.00056	3086 \pm 88

128 ppm at 4.5 μm .

In the various solutions for Spitzer transit depths described above, differences persist between 3.6 and 4.5 μm , and between the two transits observed at 3.6 μm . Those differences are minimized by our default solutions, i.e. freezing the orbital parameters at the values given by West et al. (2016) and solving for R_p^2/R_s^2 . Given that the orbital parameters we derive in this paper are closely consistent with West et al. (2016), we adopt our default solutions for transit depths. Those values are listed in Table 2.3, and the best-fit transit times are included. Figure 2.5 illustrates the fits, after removal of the systematic effects, and binning the data for visual clarity.

2.4 PHOTOMETRIC OBSERVATIONS OF WASP-76

The star can vary in brightness over time from changing starspots coverage. When the planet transits the relative brightness changes from the planet occultation will be different depending on the amount of starspots present at the time. Therefore spectra measured at different time could have offsets between them and mimic atmospheric features. To avoid this effect we need to monitor the star brightness over the periods when the observations are taken.

We acquired a total of 208 out-of-transit observations of WASP-76 during five recent

observing seasons, not including several transit observations each year, with the Tennessee State University (TSU) Celestron 14-inch (C14) automated imaging telescope (AIT) at Fairborn Observatory. The AIT uses an STL-1001E CCD camera from Santa Barbara Instrument Group (SBIG); all exposures were made through a Cousins R filter. Each observation consisted of 3–10 consecutive exposures on WASP-76 and several comparison stars in the same field of view. The individual frames were co-added and reduced to differential magnitudes – i.e. WASP-76 minus the mean brightness of seven constant comparison stars. Further details of our observing, reduction, and analysis techniques can be found in [Sing et al. \(2015\)](#).

The photometric observations are summarized in Table 2.4. Column 4 lists the yearly standard deviations of the observations from their seasonal means; these values are consistent with the precision of a single observation, as determined from the comparison stars. Our SBIG STL-1001E CCD camera suffered a gradual degradation during the 2017-18 observing season, resulting in the loss of data from that season. The camera was replaced with another SBIG STL-1001E CCD to minimize instrumental shifts in the data. Nonetheless, there appears to be a shift in the seasonal-mean differential magnitudes, given in column 5, of several milli-magnitudes between the third and fourth observing seasons. Otherwise, the night-to-night and year-to-year variability in columns 4 & 5 show that WASP-76 is constant on both time scales to the limit of our precision.

The complete WASP-76 data set is plotted in the top panel of Figure 3.4, where the data have been normalized so that each seasonal-mean differential magnitude is the same as the first observing season. This removes any year-to-year variability in the comparison stars as well as long-term variability in WASP-76, if any. The bottom panel shows the frequency spectrum of our complete data set (note the absence of the 2017-18 observing season) and gives no evidence for

Table 2.4 SUMMARY OF AIT PHOTOMETRIC OBSERVATIONS OF WASP-76

Observing Season	N_{obs}	Date Range (HJD - 2,400,000)	Sigma (mag)	Seasonal Mean (mag)
2014-15	44	56965-57089	0.0040	-2.7280
2015-16	51	57293-57451	0.0030	-2.7301
2016-17	28	57708-57810	0.0024	-2.7267
2018-19	42	58384-58522	0.0045	-2.7346
2019-20	43	58756-58906	0.0045	-2.7355

any coherent periodicity between 1 and 100 days, as expected from the lack of variability shown in Table 2.4.

Our data were observed during a three years period. If the star is variable, we will suffer constant offsets in transit and eclipse depth between data taken at different times. The long term photometric monitoring of WASP-76 with no detection of any periodicity on short timescales allows us to confirm features in the planet spectra are not caused by any short term stellar variability. However, this does not rule out longer term variability causing potential offsets between observations separated by longer than a year since we have normalized each seasonal mean flux level to the first season.

2.5 Comparison with previous studies

We have compared our reduced transit spectrum with previous studies (Edwards et al., 2020; von Essen et al., 2020) and we believe the major discrepancies come from the different approaches used for the satellite contaminated frames and the companion star dilution correction. For the WFC3 transit dataset we removed all frames in the second orbit after the satellite crossing and Edwards et al. (2020) only removed the satellite crossing frames themselves. Imperfect correction for the lingering extra flux (Fig 2.4) induced by the satellite will result in a smaller

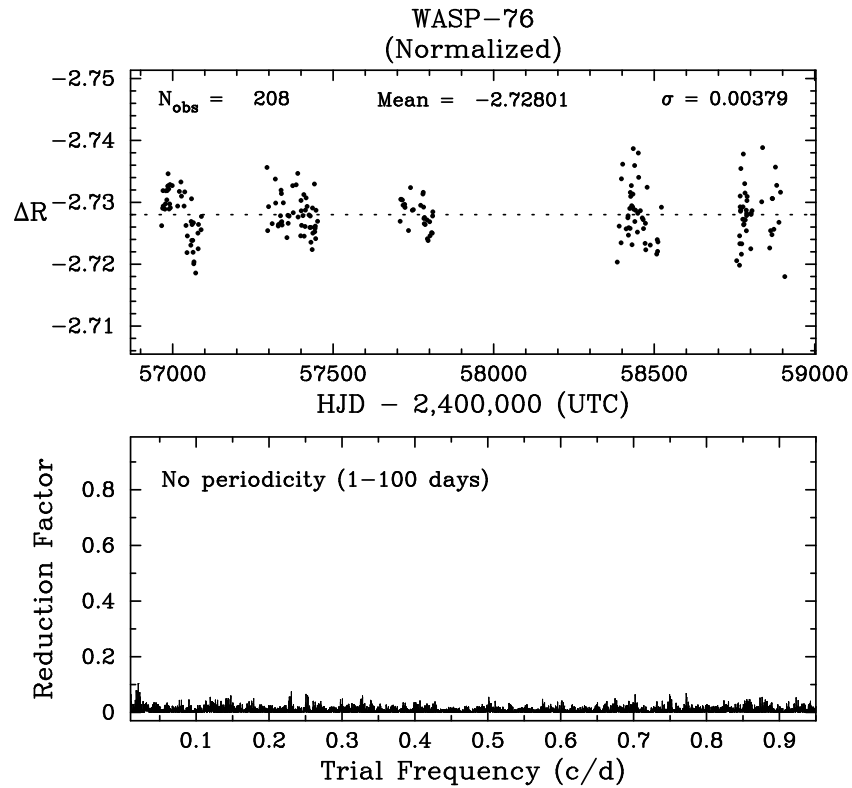


Figure 2.11 *Top*: AIT photometry of WASP-76 between 2014 and 2020 but lacking the 2017-18 observing season. The observations have been normalized so that all observing seasons have the same mean as the first season. *Bottom*: Frequency spectrum of the normalized observations showing the lack of any significant periodicity between 1 and 100 days.

transit depth. So we decided to adopt a more conservative approach to discard those frames.

For the dilution correction, [von Essen et al. \(2020\)](#) fitted two Gaussian functions to the STIS 2D spectral images at each wavelength and then subtract the companion flux contribution. [Edwards et al. \(2020\)](#) used the WFC3 simulator Wayne to model the companion star flux contribution based on the reported K band delta magnitude and stellar parameters from [Bohn et al. \(2020\)](#).

Our approach is different as discussed in section 2.1, we fit for the companion star SED based on the observed photometric data points and uniformly apply the resulting dilution factors to STIS, WFC3 and Spitzer spectra. Our approach avoids the need to customizing for instrument specific systematics when correcting for the companion flux contribution. We are also able to propagate the uncertainties from the companion star stellar parameters into the final transmission and emission spectra of the planet consistently across all wavelengths. As a result, our error bars on the final spectra are larger than reported in previous studies ([Edwards et al., 2020](#); [von Essen et al., 2020](#)). We believe our method of correcting for the dilution effect is well physically motivated based on our best knowledge of the companion star, consistent across all 3 instruments covering from 0.3 to 4.5 μm , and robust by integrating uncertainties on the parameters of the companion star.

2.6 Analysis & Interpretation

After obtaining both the transit and eclipse spectra of WASP-76b, the next step is to physically interpret the spectra. Given different sets of parameters such as radius, metallicity, C/O ratio, temperature and aerosol properties, a model transit or eclipse spectrum can be generated via forward radiative transfer models based on transit and eclipse light path geometry. Running

Table 2.5 ATMO transit retrieval priors & Posteriors

Parameter	Prior	Posterior
	\mathcal{U} for uniform prior	
$\log(Z/Z_{\odot})$	$\mathcal{U}(-2.8, 2.8)$	$-2.309^{+0.574}_{-0.187}$
$R_{pl}(\text{Jup})$	$\mathcal{U}(1.8565, 2.0519)$	$1.945^{+0.004}_{-0.003}$
$\log(K_{IR})$	$\mathcal{U}(-5, -0.5)$	$-2.198^{+0.004}_{-0.003}$
$\log(\gamma/IR)$	$\mathcal{U}(-4, 1.5)$	$-1.558^{+0.750}_{-0.785}$
beta	$\mathcal{U}(0, 1.25)$	$0.757^{+0.025}_{-0.026}$
$\log(C/C_{\odot})$	$\mathcal{U}(-2.8, 2.8)$	$-0.891^{+0.485}_{-0.656}$
$\log(O/O_{\odot})$	$\mathcal{U}(-2.8, 2.8)$	$-1.069^{+0.429}_{-0.481}$
$\log(\text{Na}/\text{Na}_{\odot})$	$\mathcal{U}(-2.8, 2.8)$	$0.649^{+0.511}_{-0.902}$
$\log(\text{Ti}/\text{Ti}_{\odot})$	$\mathcal{U}(-2.8, 2.8)$	$-0.365^{+0.819}_{-0.793}$
$\log(\text{V}/\text{V}_{\odot})$	$\mathcal{U}(-2.8, 2.8)$	$-0.713^{+0.510}_{-0.431}$
$\log(\text{Fe}/\text{Fe}_{\odot})$	$\mathcal{U}(-2.8, 2.8)$	$-0.275^{+0.866}_{-0.667}$

Table 2.6 ATMO eclipse retrieval priors & Posteriors

Parameter	Prior	Posterior
	\mathcal{U} for uniform prior	
$\log(Z/Z_{\odot})$	$\mathcal{U}(-2.8, 2.8)$	$-0.479^{+1.345}_{-1.169}$
$\log(K_{IR})$	$\mathcal{U}(-5, -0.5)$	$-1.396^{+0.914}_{-1.138}$
$\log(\gamma/IR)$	$\mathcal{U}(-4, 1.5)$	$0.459^{+0.522}_{-0.263}$
beta	$\mathcal{U}(0, 2)$	$1.226^{+0.064}_{-0.061}$
$\log(C/C_{\odot})$	$\mathcal{U}(-2.8, 2.8)$	$0.658^{+0.885}_{-1.347}$
$\log(O/O_{\odot})$	$\mathcal{U}(-2.8, 2.8)$	$-0.567^{+1.646}_{-1.155}$

atmospheric models numerous times while varying the input parameters based on the goodness of fit of each combination and obtaining the posterior distribution of all parameters in the Bayesian statistical framework is called a retrieval analysis (Line et al., 2014; Zhang et al., 2020; ?). It allows us to obtain the best-fit physical parameters and their corresponding uncertainties. However, retrieval could be computational expensive depending on the complexity of individual forward models. Approximations such as a parameterized temperature-pressure (TP) profile, cloud scattering property or low-resolution opacity library are usually adopted to speed up the forward model and the retrieval. We performed retrieval analysis on WASP-76b using ATMO (Sing et al., 2015) which is a Markov chain Monte Carlo (MCMC) algorithm based on forward radiative transfer models. In addition, we also ran a self-consistent PHOENIX (Lothringer et al., 2018) model grid which uses radiative and chemical equilibrium. We used these two different models to cross validate and confirm the physical interpretation of the spectra.

2.6.1 Strong metal absorbers in STIS G430L spectrum

The WASP-76b spectrum shows a steep slope in the G430L spectrum. In other cooler hot Jupiters, the STIS blue part of the spectrum has been used to probe the Rayleigh scattering in the atmosphere as it usually exhibits larger transit depths and slopes down into longer wavelengths. However, 0.3 to 0.4 μm of WASP-76b spectrum shows a much steeper slope compared to the rest of the spectrum which means one continuous Rayleigh scattering slope can not sufficiently explain the observed spectrum. To understand the origin of unexpected excess transit depth, we performed retrieval analysis with ATMO (Amundsen et al., 2014; Drummond et al., 2016; Goyal et al., 2018; Tremblin et al., 2016, 2015), which has been widely used before for retrieval analyses

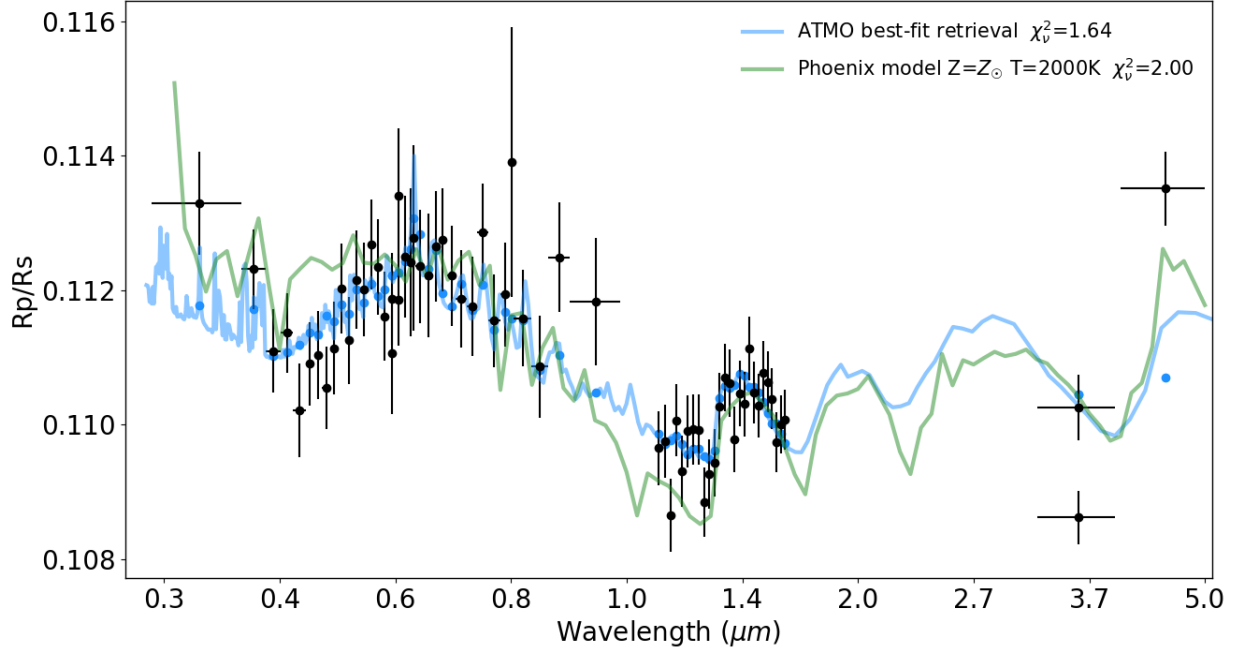


Figure 2.12 Transmission spectrum of WASP-76b overplotted two different best-fit models. The green line is the PHOENIX atmosphere model with equilibrium chemistry, solar metallicity and internal temperature of 200K. The blue line is the best-fit models from ATMO retrieval.

of transmission (Wakeford et al., 2017) and emission (Evans et al., 2017) spectra. We performed a cloud-free free-element equilibrium-chemistry retrieval with free abundance of specific species (C, O, Na, Ti, V, Fe) and a fitted TP profile (3.6). All other elements were varied with a single metallicity parameter. ATMO is able to fit the STIS blue part of the spectrum with a solar Fe abundance and the best-fit model has a χ^2_v of 1.64. However, the first observed point extending from 0.29 to 0.37 μm is still $\sim 2\sigma$ higher than the ATMO model.

The next modeling tool we applied is PHOENIX (Lothringer et al., 2018) atmosphere forward model, It self-consistently solves layer by layer radiative transfer assuming chemical and radiative-convective equilibrium based on the irradiation received at the top of the atmosphere from the host star (Lothringer and Barman, 2019). PHOENIX is equipped with a comprehensive EUV-to-FIR opacity database of atomic opacity due to their importance in modeling stellar

spectra, which makes it particularly suitable on predicting ultra-hot Jupiter atmospheres in the bluer wavelengths (Lothringer et al., 2020). We generated a grid of PHOENIX models with various metallicity, heat redistribution and internal temperatures. The best-fit model (Fig. 2.12) is at solar metallicity with a terminator temperature of 2000K which has a χ^2_ν of 2. With the additional opacity from metals and molecules (Fe I, Fe II, Ti I, Ni I, Ca I, Ca II, and SiO) included in the PHOENIX model, it is able to fully fit the short-wavelength slope. However, it predicts larger absorption depth between the 0.4 to 0.5 μm region which is likely due to the assumption of solar metallicity and elemental abundances. The lower than expected abundances of NUV absorbers such as TiO, V I and Fe I could be due to condensation and/or rain-out on the day-to-night terminator inferred by Ehrenreich et al. (2020).

This similar feature of steep slope in the NUV has also been observed in WASP-121b (Evans et al., 2017) with Sodium Hypochlorite (SH) proposed as the missing opacity source. With more recent observations (Sing et al., 2019) with STIS E230M from 228 and 307 nm, multiple atomic lines including Mg II and Fe II have been detected and resolved in WASP-121b. This indicates neutral and ionized atomic metal lines are more likely to be the cause of the strong NUV absorption signatures in the STIS G430L spectrum. With both WASP-76b and WASP-121b showing strong NUV absorption features, neutral and ionized metals may exist in many more ultra-hot Jupiter atmospheres (Lothringer et al., 2020).

2.6.2 Detection of TiO and H₂O

We detected TiO and H₂O in the transmission spectrum of WASP-76b. The 0.4 to 1 μm part of the spectrum where TiO opacity dominates shows significantly deeper transit depth (~ 500

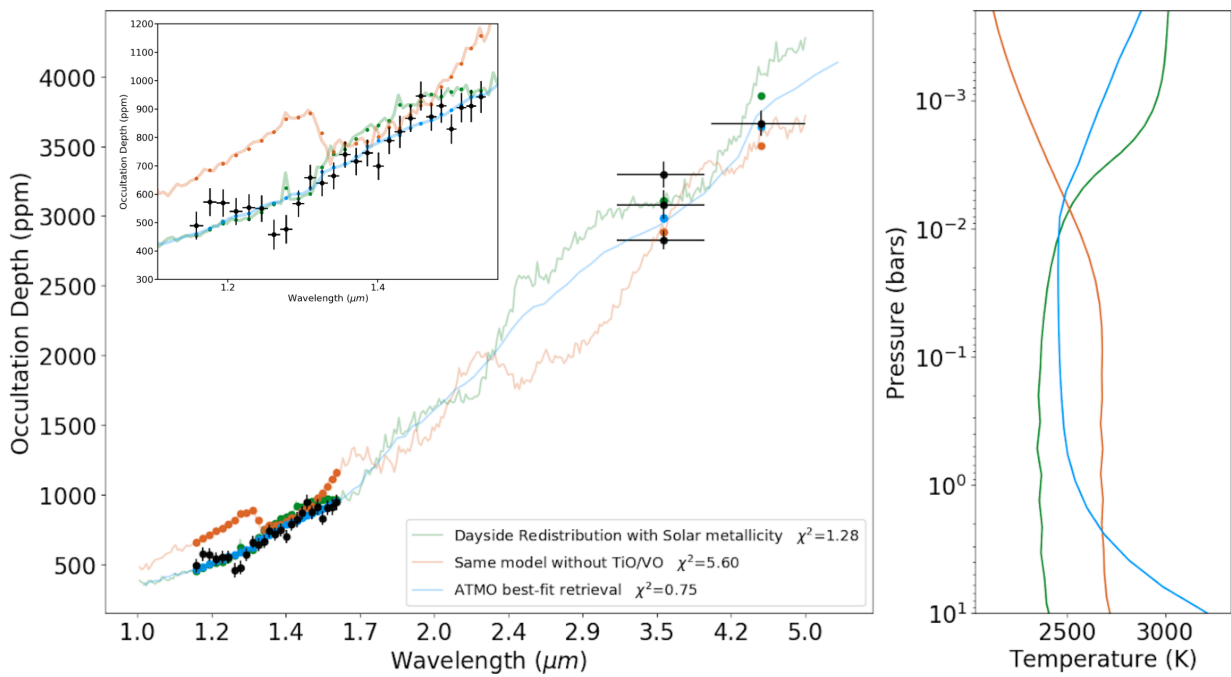


Figure 2.13 The eclipse spectrum (left panel) of WASP-76b overplotted with two PHOENIX (green and orange) models and one ATMO (blue) best-fit spectrum. The two PHOENIX models are both at solar metallicity with dayside heat redistribution, but one with TiO/VO and the other without. The comparison is to show the presence of TiO/VO is strongly favored by the data. The corresponding TP profiles are plotted in the right panel with matching colors to the three emission model spectra.

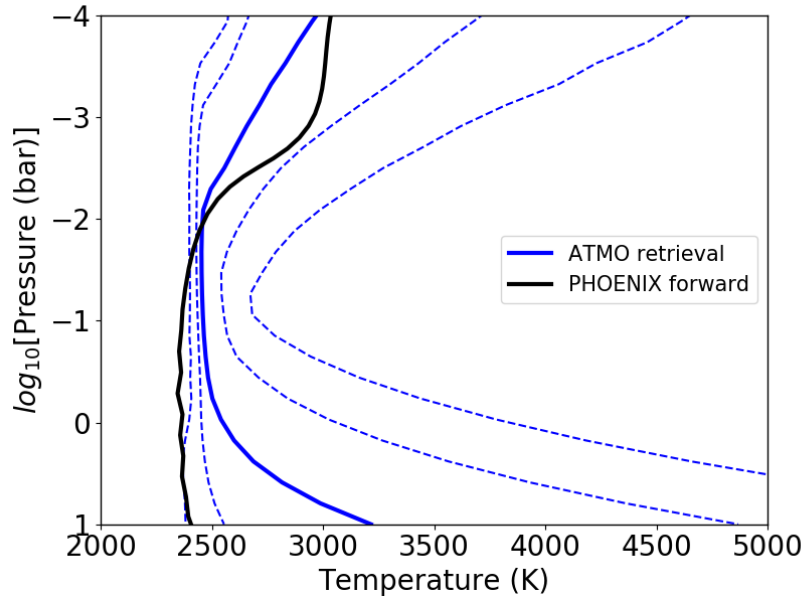


Figure 2.14 The TP profiles of ATMO retrieval (blue) and PHOENIX (black) atmosphere model for the emission spectrum. The dashed blue lines represent one and two sigma range for ATMO TP profiles.

ppm) compared to the WFC3/G141 spectrum. This feature is well explained by all two models with TiO absorption features. At this temperature range, TiO is expected to be in gaseous and abundant in the atmospheres as shown in the top-right panel of Fig. 2.15. Water vapor absorption feature at $1.4 \mu m$ has also been observed in the spectrum, which is expected as thermal dissociation of water starts at temperatures $>2500K$ (Bottom-left Fig. 2.15).

2.6.3 Emission spectrum

WASP-76b shows blackbody-like WFC3/G141 emission spectrum with muted water features but strong CO emission feature at Spitzer $4.5 \mu m$ band. The best-fit PHOENIX model shows dayside heat-redistribution and solar metallicity assuming equilibrium chemistry. We also ran a comparison PHOENIX model with the same setup but excluding TiO/VO to demonstrate the data

strongly favors the presence of gaseous TiO/VO, as the χ^2_ν is larger by 4.32, which is consistent with our finding in the transmission spectrum. In addition, we performed ATMO free-element equilibrium chemistry retrieval similarly to the transmission spectrum, though isotropic scattering was also included along with the thermal emission. The resulting ATMO best-fit model is highly consistent compared to the PHOENIX model with both models showing similar emission spectra and TP profiles (See Fig. 2.14). ATMO also favors solar metallicity in the retrieval posterior distribution (Fig. 2.18) but with less certainty at the C/O ratio since the muted water feature limits the constraints on the oxygen abundance. Both models favor a dayside temperature range of 2500 to 2600K around 1 bar and an inverted TP profile with temperature increasing to around 3000K at 0.1 mbars. Water starts to dissociate at such high temperature and low pressure region of the atmosphere as shown in Figure 2.15, therefore we do not see prominent water emission features. At deeper levels (~ 1 bar) of the atmosphere, water vapor should still survive, but any absorption features will be obscured by the hotter continuum emission in the upper atmosphere layers. On the other hand, CO is able to survive in much higher altitude and temperature due to the strong triple bond structure. Indeed, we see clear CO emission features in the Spitzer 4.5 μm band.

2.6.4 Temperature inversion

We found a clear temperature inversion (Figure 2.14) confirmed by ATMO and PHOENIX models. The Spitzer 4.5 μm CO emission feature strongly favors an inverted TP profile with higher temperature CO gas presence in the upper atmosphere. The transmission spectrum also favors an inverted TP profile as the retrievals need the higher temperature at the low pressures

to boost the scale heights and the size of spectral features to better match the data. Theories have indicated inversion is caused by a combination of optical absorbers such as TiO (Fortney et al., 2008) and atomic metal absorption heating the upper layers with the lack of cooling from molecules like water (Lothringer et al., 2018). Our observed spectrum supports this paradigm with detection of TiO and atomic metal opacity in the transmission and muted water emission feature due to thermal dissociation at the highest altitudes. The detection of TiO and temperature inversion in the emission spectrum is also consistent with the independent analysis from Edwards et al. (2020) which reported similar findings.

2.6.5 Model comparison

ATMO best-fit model has the lower χ^2_ν but PHOENIX generates a remarkable good fit in both transit and eclipse especially as only two parameters were varied in our grid of forward models. Retrieval frameworks find the best-fit spectrum through maximizing the likelihood which allows it to fine tune model parameters and better respond to smaller features in the data. Therefore, despite using an incomplete NUV opacity database, ATMO is able to produce better overall χ^2_ν best-fit spectrum than the PHOENIX forward model. However, it is more important that ATMO and PHOENIX show good agreement on the general physical parameters including temperature structure, C/O ratio and chemical abundance. This gives us increased confidence in our conclusion, as both the retrieval and forward modeling methods agree.

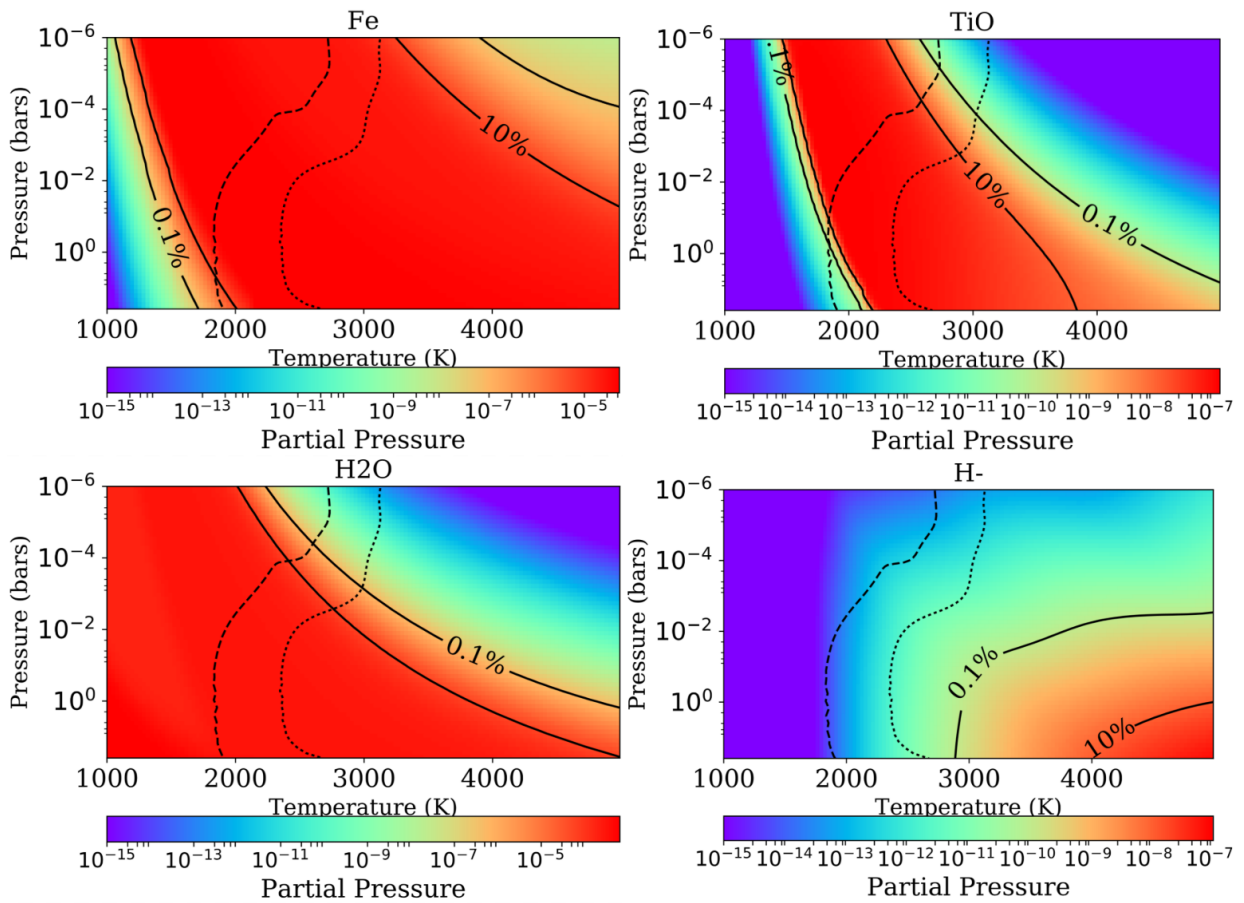


Figure 2.15 Partial pressure contours of four chemical species (Fe, TiO, H₂O and H⁻) overplotted with PHOENIX model TP profiles from transit (full heat redistribution, dashed lines) and eclipse (dayside heat redistribution, dotted lines) spectra. Gaseous Fe is abundant and present in both the terminator and dayside regions of the planet across all pressure levels. TiO and water vapor exist in higher pressure regions but begin to dissociate in higher temperature and altitude layers. H⁻ is limited in the cooler terminator but starts to show up on the hotter dayside.

2.7 Summary and Conclusions

We observed a total of 7 transits and 5 eclipses of the highly irradiated ultra-hot Jupiter WASP-76b using HST WFC3/STIS and Spitzer. After correcting for the dilution effect of a nearby companion star, and refitting the orbital parameters, we performed retrieval analysis on the transmission and emission spectra using ATMO and a PHOENIX grid. The results from these independent modeling tools are in generally good agreement with the biggest difference being the completeness of NUV opacity lines of each model. We demonstrated the importance of including all atomic and molecular metal lines in the NUV to fully explain the excess transit depth observed between 0.3 and 0.4 μm in WASP-76b (Lothringer et al., 2020). Water vapor and TiO have also been directly detected in the transmission spectrum from STIS and WFC/G141 observations. Both transit and eclipse spectrum favor an inverted TP profile which is confirmed by both ATMO and PHOENIX models. The detection of TiO and ionized metals at the same time with an inverted TP profile are consistent with the theory of temperature inversion in ultra-hot Jupiters being caused by high altitude strong UV and optical absorbers heating the upper layers. The lack of water emission due to dissociation at high temperature and altitude further drives the temperature inversion from the absence of cooling.

This study of WASP-76b supports some of our current understanding of ultra-hot Jupiter such as their thermal structure while poses new questions about their heavy metals composition that have previously been mostly ignored. It is evident more NUV atmosphere observations of ultra-hot Jupiters are needed for a more complete understanding of these unique planets. HST is currently the only observatory capable of observing in the NUV wavelength which will not be accessible with JWST. WASP-76b along with other ultra-hot Jupiters will be great targets for

future detailed NUV studies with HST.

2.8 Appendix

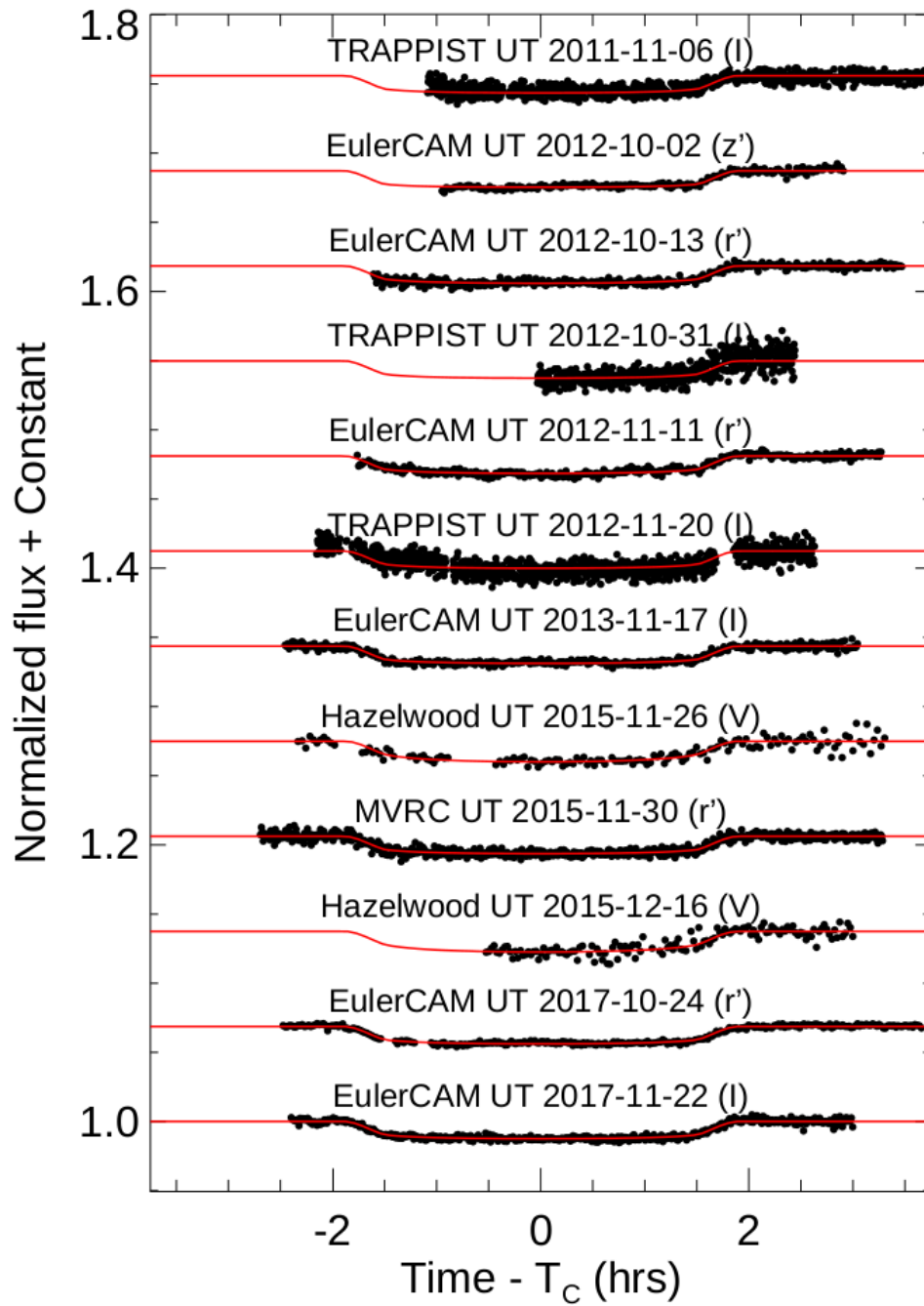


Figure 2.16 Transit lightcurves used in EXOFASTv2 fit.

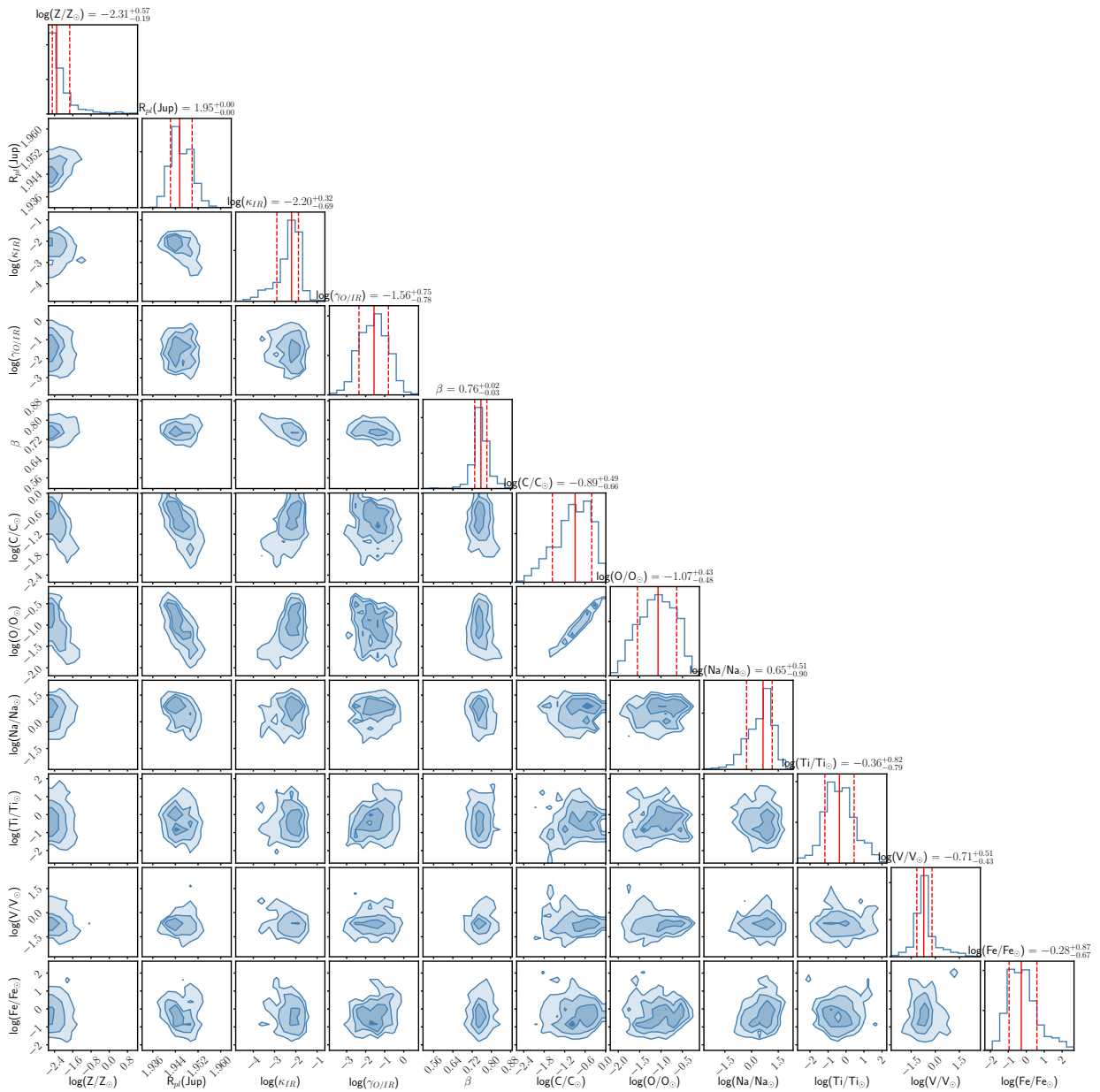


Figure 2.17 The posterior distribution of ATMO retrieval of the transmission spectrum. Six chemical elements (C, O, Na, Ti, V, Fe) are allowed to vary freely with everything else scale to solar metallicity. All retrieved elemental abundance are consistent with solar value to one sigma.

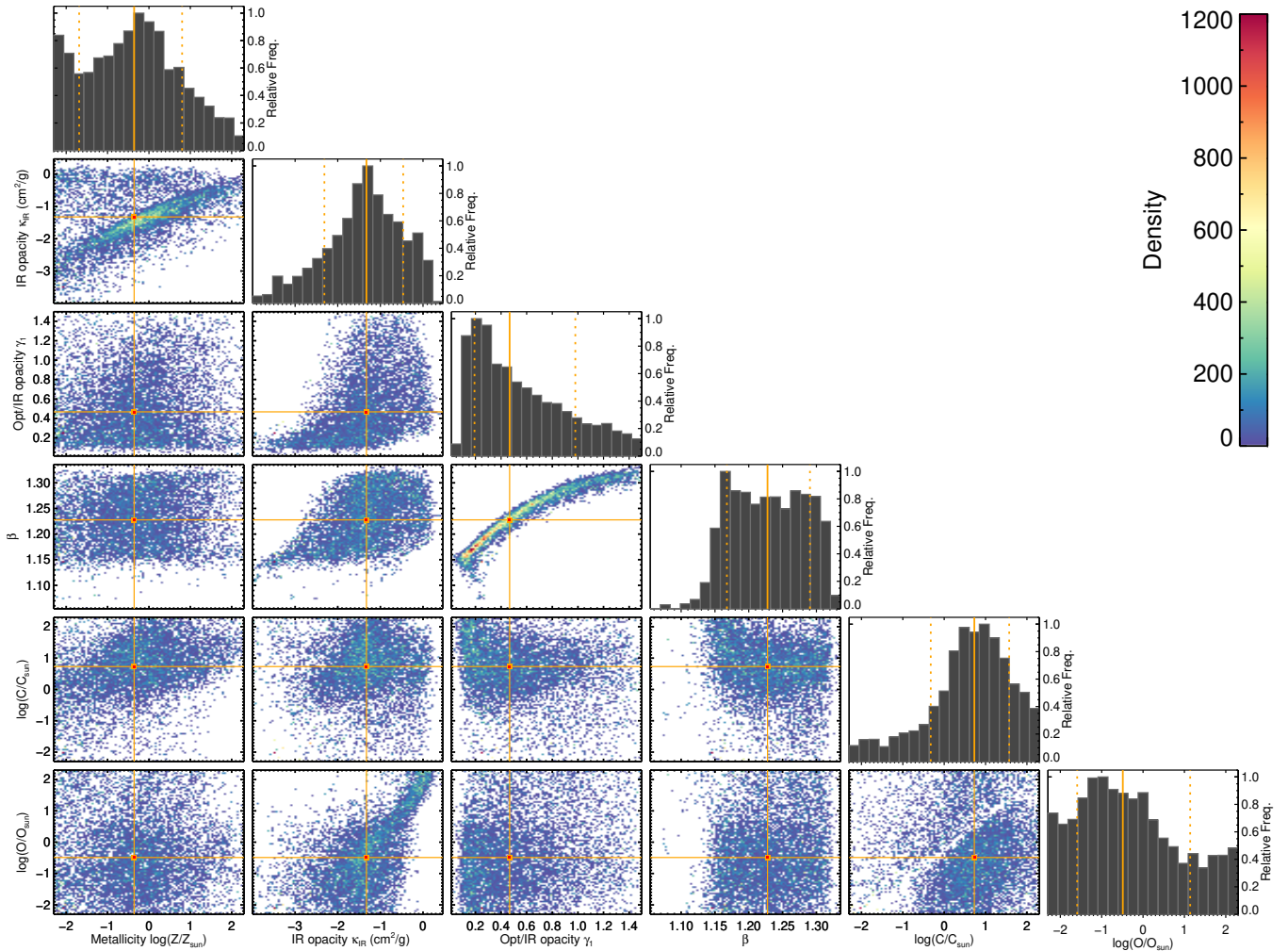


Figure 2.18 The posterior distribution of ATMO retrieval of the emission spectrum. The carbon and oxygen abundances are poorly constrained due to a muted water feature in the WFC3/G141 band. Retrieved solar metallicity is consistent with results from the transmission spectrum and the PHOENIX models.

Chapter 3: Transit and Eclipse Spectroscopy of the Hot Jupiter WASP-74b

3.1 Overview

Planets are like children with each one being unique and special. A better understanding of their collective properties requires a deeper understanding of each planet. Here we add the transit and eclipse spectra of hot Jupiter WASP-74b into the ever growing dataset of exoplanet atmosphere spectral library. With six transits and three eclipses using the HST and Spitzer, we present the most complete and precise atmospheric spectra of WASP-74b. We found no evidence for TiO/VO nor super-Rayleigh scattering reported in previous studies ([Mancini et al., 2019](#)). The transit shows a muted water feature with strong Rayleigh scattering extending into the infrared. The eclipse shows a featureless blackbody-like WFC3/G141 spectrum and a weak methane absorption feature in the Spitzer 3.6 μm band. Future James Webb Space Telescope (JWST) follow up observations are needed to confirm these results.

3.2 Introduction

With the many recent studies of hot Jupiter atmospheres, we are starting to see a highly diverse landscape of atmospheric chemical composition and thermal structure. Some ultra-hot ($T_{eq} > 2000K$) Jupiters have shown significant gaseous heavy metal absorption ([Fu et al., 2021](#);

Lothringer et al., 2020) while other cooler hot Jupiters exhibit high metallicity (Colón et al., 2020; Lewis et al., 2020; Sheppard et al., 2021) and aerosols coverage (Alam et al., 2020). We have also detected absorption and emission features of various chemical species such as water, sodium, CO/CO₂, metals and metal oxides (TiO and VO) (Evans et al., 2017; Fu et al., 2021; Kreidberg et al., 2018b). With this ever growing library of exoplanet atmosphere spectra, we are starting to understand the chemical and physical processes taking place in these hot Jupiters. For example, statistical studies (Fu et al., 2017; Sing et al., 2016) have provided valuable insights into how aerosol presence varies in different atmospheric conditions and were later supported by detailed aerosol modeling (Gao et al., 2020). Comparative studies (Baxter et al., 2021; Garhart et al., 2020; Parmentier et al., 2018; Wallack et al., 2021; Zhang et al., 2018) have furthered our understanding of exoplanet thermal structures and heat circulation (Kataria et al., 2016). A large library of measured high quality high precision exoplanetary spectra will be essential to our future studies of exoplanet atmospheres.

Here we present a uniformly analyzed transmission and emission spectrum of hot Jupiter WASP-74b (Table 3.3) ranging from 0.3 to 4.5 μm in wavelength using multiple instruments on the HST and Spitzer. We have also compared our transit spectrum with previous ground based observations and other independent analyses. We found a muted water absorption feature with a significant aerosol scattering slope in the transit spectrum, and a featureless blackbody-like WFC3/G141 eclipse spectrum with absorption feature in the Spitzer 3.6 μm bands.

WASP-74b transit observations

	Grism/Filter	Visit	GO Program ID	PI
HST STIS	G430L	2017-05-04 & 07-20	14767	Sing & López-Morales
HST STIS	G750L	2017-06-20	14767	Sing & López-Morales
HST WFC3	G141	2016-10-06	14767	Sing & López-Morales
Spitzer	IRAC 3.6	2017-01-14	13044	Deming
Spitzer	IRAC 4.5	2017-01-16	13044	Deming

WASP-74b eclipse observations

	Grism/Filter	Visit	GO Program ID	PI
HST WFC3	G141	2017-05-02	14767	Sing & López-Morales
Spitzer	IRAC 3.6	2017-01-15	13044	Deming
Spitzer	IRAC 4.5	2017-02-12	13044	Deming

Table 3.1 A list of our 6 transit and 3 eclipse observations of WASP-74b.

WASP-74b parameters

Equilibrium Temperature	T_{eq} (K)	1926^{+21}_{-21}
Radius	R_p (R_{Jup})	$1.404^{+0.018}_{-0.012}$
Mass	M_p (M_{Jup})	$0.826^{+0.015}_{-0.014}$
Period	P_{orb} (days)	$2.1377445^{+0.0000018}_{-0.0000018}$
Semi-major axis	a (au)	$0.03443^{+0.00022}_{-0.00029}$
Inclination	i (degree)	$79.86^{+0.21}_{-0.21}$

Table 3.2 Parameters are from (Mancini et al., 2019).

3.3 Observations

We observed a total of six transits and three eclipses of WASP-74b using multiple instrument modes on HST and Spitzer (Table. 3.1). The data comprises two observation programs and some parts of the data were published in previous studies (Garhart et al., 2020; Luque et al., 2020; Mancini et al., 2019). We have uniformly analyzed the full dataset including new HST/STIS transit, HST/WFC3 and Spitzer eclipse. All the data are reduced using the same orbital parameters and limb darkening coefficients from the same 3D stellar model.

3.4 Data analysis

3.4.1 HST STIS data reduction

HST orbits the earth every 90 minutes which results in an observing gap of ~ 45 minutes when the target is not in the continuous viewing zone. Combined with the thermal breathing of HST, this leads to an orbital-dependent systematics of the lightcurve. Various detrending techniques (Nikolov et al., 2014; Sing et al., 2011) have been developed to correct for this effect. Sing et al. (2019) used the time-tagged engineering information from the jitter files for each exposure to construct a parametric model. Jitter files record the telescope movements during the observation. This new jitter decorrelation method was shown to improve the photometric performance of HST STIS time series observations compared to previous used methods (Sing et al., 2019).

The STIS data reduction pipeline we used in this paper is identical to the jitter decorrelation method detailed in Sing et al. (2019) except it is applied on G430L and G750L data instead of NUV-MAMA detector with E230M echelle grating. The orbital parameters (Table. 3.3) have been fixed to the values used in Mancini et al. (2019). For limb darkening (Table 3.13), we used the 3D stellar model from the Stagger-grid (Magic et al., 2015) with the parameters $T_{eff}=6000\text{K}$, $\log g=4$, $[\text{Fe}/\text{H}]=0$. The systematics corrected light curves and residuals for two G430L visits and one G750L visit are shown in Figures 3.10, 3.11 and 3.12.

3.4.2 HST WFC3 data reduction

The HST WFC3 data reduction pipeline is exactly the same as detailed in Chapter 2 for both transit and eclipse. We used a combination of the `BATMAN` lightcurve model (Kreidberg, 2015) with the `RECTE` charge trapping systematics model (Zhou et al., 2017) for lightcurve detrending. The orbital parameters (Table. 3.3) have been fixed to the values used in Mancini et al. (2019) and the limb darkening coefficients are from the same stellar model used for the STIS data reduction.

3.4.3 Spitzer data reduction

Two transits and eclipses of WASP-74b were observed with Spitzer’s InfraRed Array Camera (IRAC Fazio et al., 2004), at both 3.6 and 4.5 (PI: D. Deming, Program ID 13044). Table 3.1 includes the observation dates for these events. Each event used an exposure time of 0.4 seconds and covered approximately 7 hours total. For data reduction and analysis we use the Photometry for Orbits, Eclipses, and Transits pipeline (POET Campo et al., 2011; Cubillos et al., 2013; Stevenson et al., 2012).

Spitzer IRAC photometry has been the major instrument mode used to investigate exoplanet atmospheres in the infrared (Deming and Knutson, 2020). The raw data is usually dominated by instrumental systematics due to intrapixel sensitivity variations on the detector in both 3.6 and 4.5 μm channels (Deming et al., 2015). During the past decade we have developed multiple methods (Deming et al., 2015; Stevenson et al., 2012) to mitigate this effect. Recently, (May et al., 2021; May and Stevenson, 2020) generated a new Gaussian centroided intrapixel sensitivity map based on years of archival Spitzer calibration data. Here we use this fixed sensitivity map (May and Stevenson, 2020) to analyze the 4.5 μm Spitzer datasets while using standard BLISS Mapping

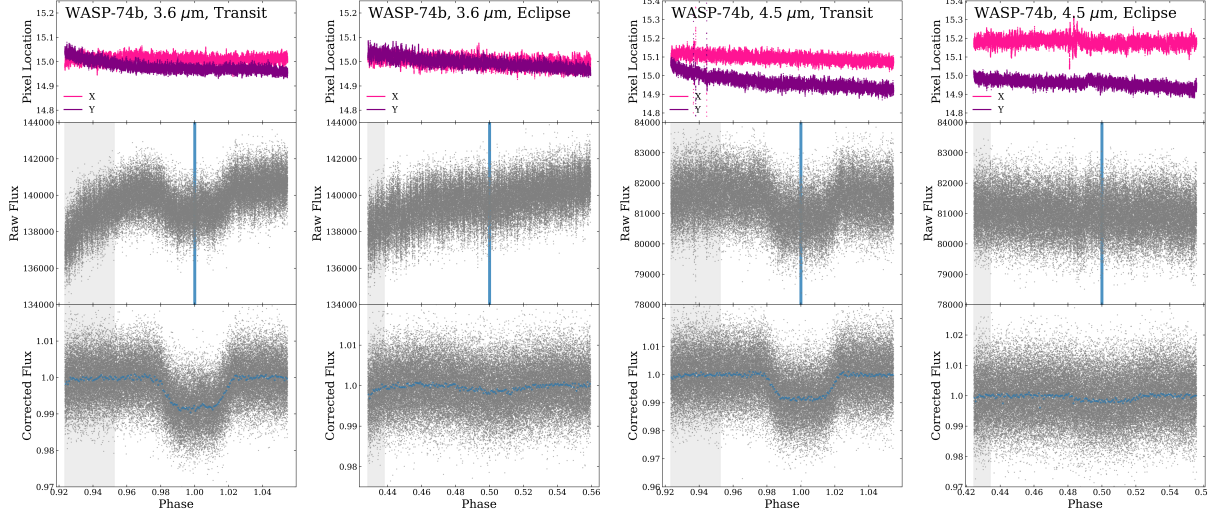


Figure 3.1 Centroids (top panels), raw flux (middle panels) and corrected flux (bottom panels) as a function of phase for all four Spitzer IRAC data sets as labeled. One can see that the 3.6 μm data sets are more heavily affected by a visit-long ramp, in combination with a stronger initial ramp for the 3.6 μm transit event. The trimmed parts of the lightcurves are shaded in grey.

at 3.6 μm . At 3.6 μm we also find that the inclusion of a second-order function with respect to the widths derived from 2D Gaussian fits (PRF-FWHM) is optimal. Figure 3.1 shows the x and y pixel locations and raw flux for all Spitzer IRAC data sets analyzed here.

For the astrophysical signal, we fit transits using the BATMAN (Kreidberg, 2015) with limb darkening coefficients fixed to values taken from the same stellar models as those used for the optical data reductions. Eclipses are modeled using the analytical model in Mandel and Agol (2002). All orbital parameters (Table. 3.3) are fixed to the same values used in the HST STIS and WFC3 data reduction to minimize systematic offsets between the data sets.

At the beginning of the observation, instrument systematics are the strongest due to the time needed for the telescope pointing to stabilize and the detector to fill up the charge traps. Therefore, the resulting ramp effect at the beginning is challenging to model and the first portion of the data has usually been discarded (Baxter et al., 2021; Garhart et al., 2020; Stevenson et al.,

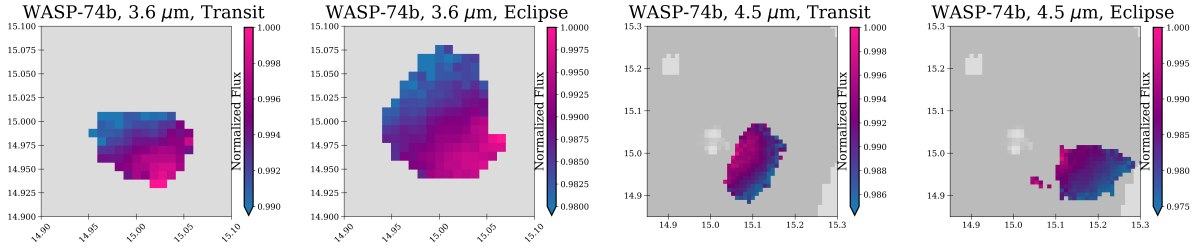


Figure 3.2 BLISS maps from best fits for all 4 Spitzer IRAC events as labeled. For the $4.5 \mu m$ maps, the darker grey regions denote where the fixed sensitivity map exists. Axis units are in sub-pixels. The BLISS map shown here is the subset of the fixed sensitivity map at the locations of the data centroids. It is not generated from this $4.5 \mu m$ dataset.

2012). For this work, we have experimented varying the amount of data points to trim at the beginning of the observation from 0 to 120 minutes while fitting the remaining lightcurve with four different ramp models (Fig. 3.3, left panels show transits and right panels show eclipses).

As expected, because the fixed sensitivity map is not dependent on other modeling choices like a standard BLISS map, its use at $4.5 \mu m$ results in minimal variations of the measured eclipse and transit depths with the amount of data trimmed from the beginning (bottom two panels of Figure 3.3), while the free BLISS map used for $3.6 \mu m$ results in transit and eclipse depths which are heavily dependent on the amount of data trimmed and ramp model used. In Figure 3.3 we also denote the ramp that has the lowest Bayesian Information Criterion (BIC) (May and Stevenson, 2020) at each trim level with a black circle around the data point. This further demonstrates that the $4.5 \mu m$ data sets are no longer beholden to the whims of the systematic removal with the best-fit ramp the same across all trim levels, while the $3.6 \mu m$ events best-fit ramp depends on the trim level. To address this, we select trimming that results in all ramps measuring the approximately the same depths based on the $3.6 \mu m$ events, and adopt the same trimming at $4.5 \mu m$ for consistency. We select 90 minutes of trimming for the transits, and 30 minutes of trimming for the eclipses.

Our final fits use a linear ramp and 2^{nd} order PRF-FWHM and standard BLISS map

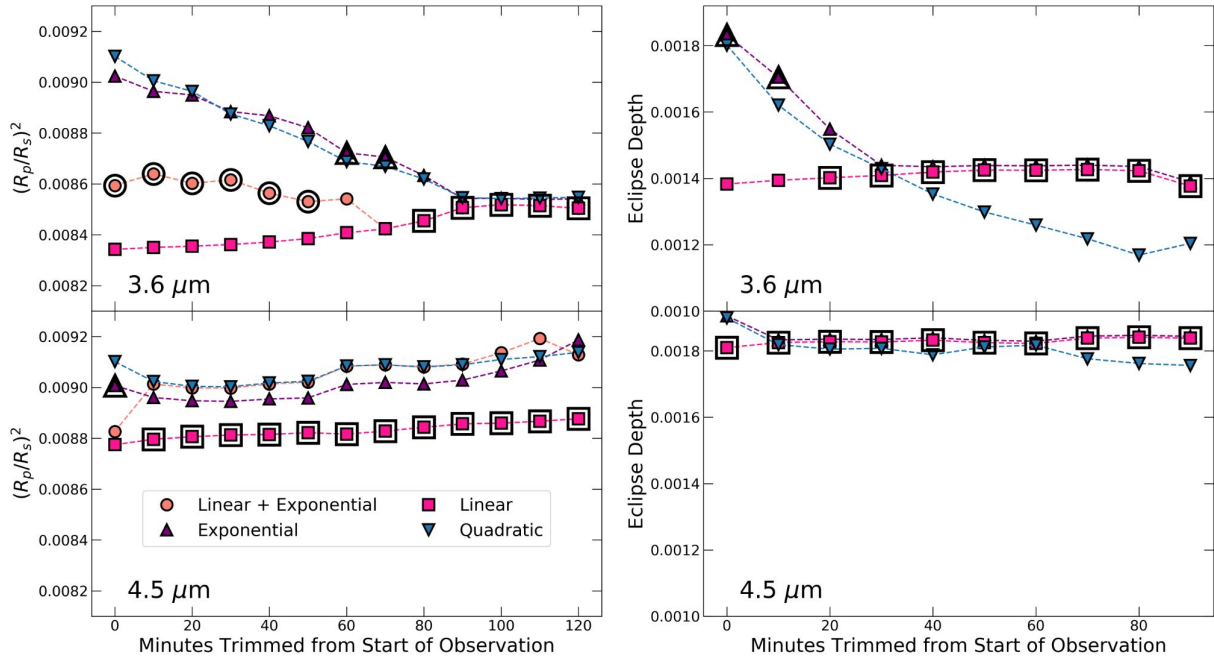


Figure 3.3 Demonstration of the dependence on ramp choice and amount of data trimmed from the start of events. The $3.6 \mu m$ and $4.5 \mu m$ events are shown on the same scale for ease of comparison. Left: Transits, Right: Eclipses. Top: $3.6 \mu m$, Bottom: $4.5 \mu m$. Our use of the fixed sensitivity map for systematic removal at $4.5 \mu m$ results in a consistent eclipse and transit depth regardless of pre-trimming and ramp model, while the $3.6 \mu m$ events are heavily dependent on the choice of these parameters due to the flexibility of the BLISS map.

detrending at $3.6 \mu m$ with a 90 minute trim for the transit and a 30 minute trim for the eclipse.

Our $4.5 \mu m$ fits use a linear ramp and fixed sensitivity map detrending for both events, with the same trimming as $3.6 \mu m$.

3.5 Simultaneous ground-based photometric monitoring

To search for the presence of magnetic activity in WASP-74, we performed nightly photometry on the star during the 2018–2021 observing seasons with the Tennessee State University Celestron 14-inch (C14) automated imaging telescope (AIT) located at Fairborn Observatory in southern Arizona (e.g., Henry et al., 2000; Oswalt, 2003). The AIT is equipped with an SBIG STL-

1001E CCD camera and uses a Cousins R filter. Each observation consists of 3–5 consecutive exposures on WASP-74 and several surrounding comparison stars in the same CCD field of view. The individual frames are co-added and reduced to differential magnitudes in the sense WASP-74 minus the mean brightness of the comparison stars. Further details of our observing, reduction, and analysis techniques can be found in [Sing et al. \(2015\)](#).

A total of 245 good nightly observations were collected between 2018 March 4 and 2021 June 18 (plus a few transit observations that we discarded). The observations are summarized in Table 3.3. The standard deviation of the individual nightly observations from the mean of the complete data set is 0.00262 mag, which is close to the typical precision of a single observation with the C14. The seasonal means agree to within 0.0007 mag. Thus, we confirm the findings of [Hellier et al. \(2015\)](#) that WASP-74 is magnetically inactive and photometrically constant.

The photometric observations are plotted in the top panel of Figure 3.4 where the vertical dotted lines mark the beginning of each calendar year. WASP-74 comes to opposition in late July; this means we lose the central part of each seasonal light curve because we must shut down our telescopes during the summer "monsoons" of southern Arizona (typically early July to early September). The summer gap is visible in the 2018, 2019, and 2020 observing seasons, but not in 2021 since the latest observations end at the shutdown. A frequency spectrum, based on least-squares fitting of sine curves, is shown in the bottom panel of Figure 3.4. No significant periodicity is seen in the range 1–100 days. Separate analyses of the individual observing seasons similarly showed no significant periodicities.

We phased the nightly observations to the radial-velocity period and computed a new least-squares sine fit. The formal peak-to-peak amplitude of the photometry is 0.00093 ± 0.00047 magnitude, consistent with zero to better than one mmag. This confirms that radial velocity

Table 3.3 SUMMARY OF AIT PHOTOMETRIC OBSERVATIONS OF WASP-74

Observing Season	N_{obs}	Date Range (HJD - 2,400,000)	Sigma (mag)	Seasonal Mean (mag)
2018	119	58182–58477	0.00242	-2.32081
2019	69	58572–58832	0.00243	-2.32147
2020	28	58925–59182	0.00338	-2.32104
2021	29	59281–59383	0.00302	-2.32146

variations in WASP-74 are indeed due to planetary reflex motion and not line-profile variations due to spots (e.g., [Paulson et al., 2004](#); [Queloz et al., 2001](#)).

We did not detect any strong stellar variability with our three-years ground-based photometric monitoring campaign. Therefore any offsets in transit and eclipse depth between different observations are unlikely to be caused by changing in host star brightness from stellar activities such as varying starspots coverage.

3.6 Comparison with previous studies

We have compared our transmission spectrum (Table. [3.12](#)) with previous studies from [Luque et al. \(2020\)](#); [Mancini et al. \(2019\)](#) which include multiple ground-based photometric points with WFC3 G141 and Spitzer datasets (Fig. [3.5](#)). System parameters (Table. [3.3](#)) used in data reduction for this work were fixed to the same exact values used in [Mancini et al. \(2019\)](#) to avoid any offsets from lightcurve fitting.

Our STIS spectrum sits between the ground-based photometry points in transit depth reported in [Mancini et al. \(2019\)](#) and [Luque et al. \(2020\)](#). The tension between STIS and ground-based results could come from the different treatments used in reducing noisy ground-based lightcurves detailed in [Luque et al. \(2020\)](#). We find no evidence supporting neither strong TiO/VO absorption indicated by increased transit depth in the optical ($\sim 500 - 700\text{nm}$) ([Mancini et al., 2019](#)) nor

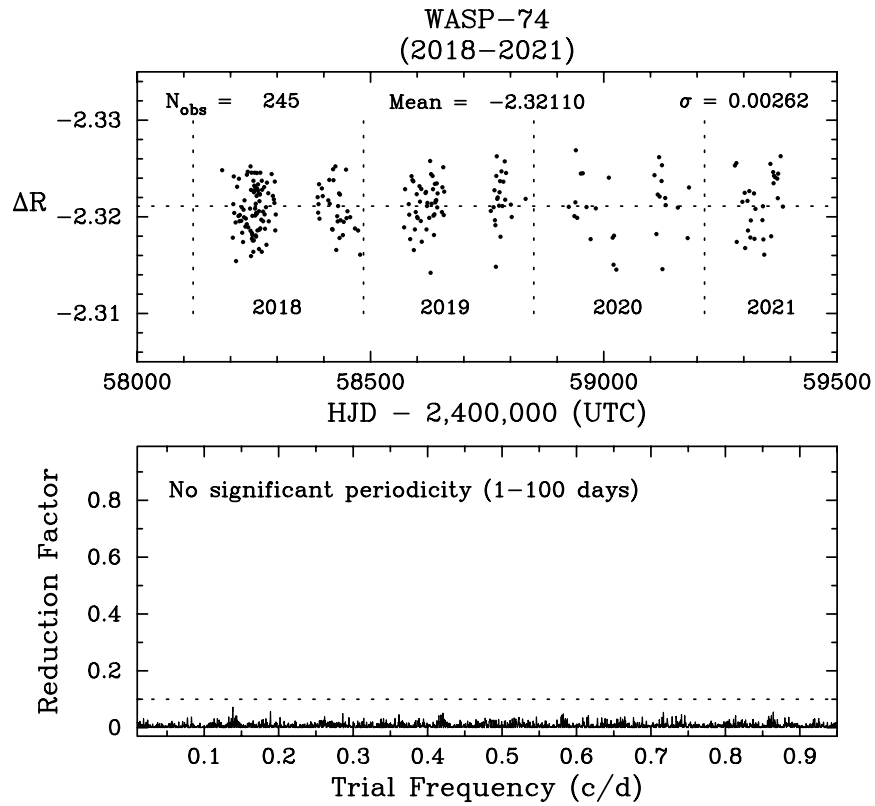


Figure 3.4 *Top*: The Cousins R band photometry of WASP-74 from 2018–2021, acquired with the C14 automated imaging telescope (AIT) at Fairborn Observatory. The star is constant on night-to-night and year-to-year time scales to the limit of our precision. *Bottom*: Frequency spectrum of the complete data set shows no significant periodicity between 1 and 100 days. The horizontal dashed line in the bottom panel represents the noise limit below which reliable periods are not found in multi-color photometry (Henry et al., 2011).

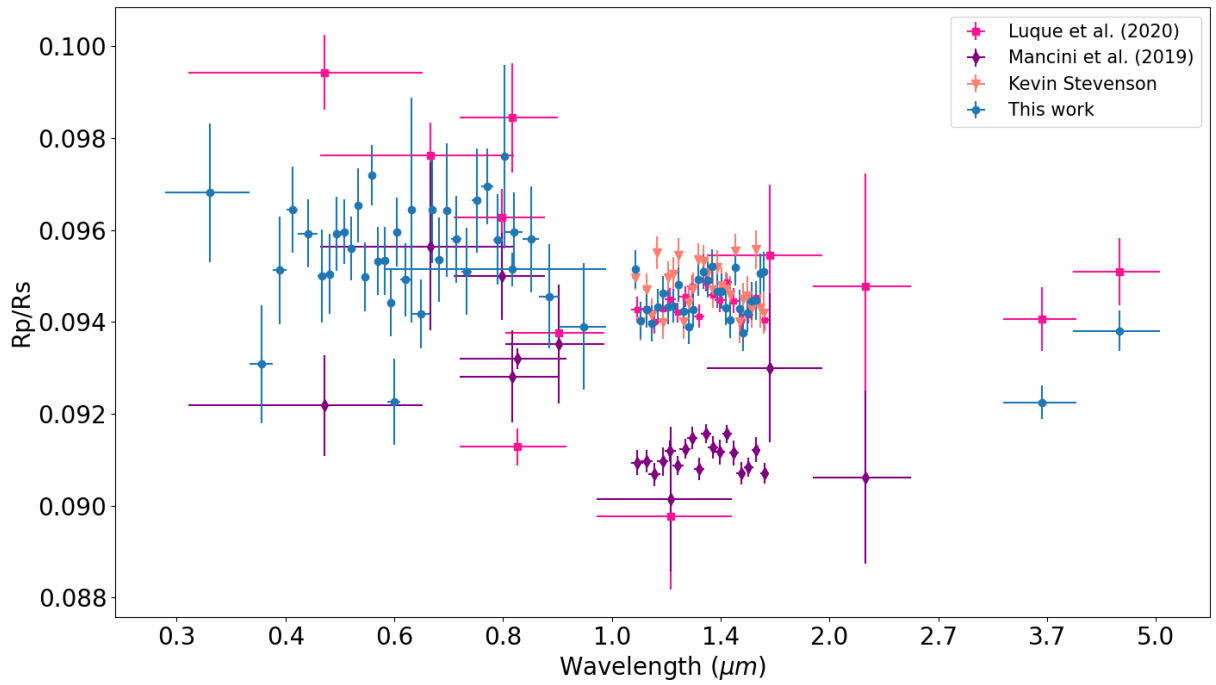


Figure 3.5 Comparison of transit spectra from this study to previous studies. We have fixed all orbital parameters to the exactly values as used in (Mancini et al., 2019).

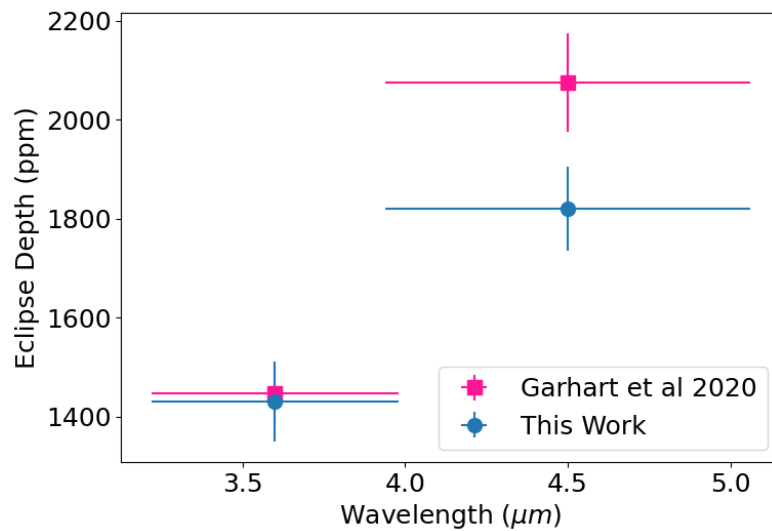


Figure 3.6 Comparison of Spitzer eclipse spectra from this study to (Garhart et al., 2020). We have fixed all orbital parameters to the exactly values as used in Mancini et al. (2019).

super-Rayleigh scattering (Luque et al., 2020).

The reduced WFC3 G141 transit spectrum has a large offset compared to Mancini et al. (2019). Luque et al. (2020) took the exact same WFC3 G141 spectrum from Mancini et al. (2019) and added an offset parameter in their PLATON retrieval. Our WFC3 G141 spectrum is highly consistent with the WFC3 offset version 2 reported in Luque et al. (2020). Kevin Stevenson (KS hereafter) also performed an independent analysis for the WFC3 G141 spectrum (Fig. 3.5) with procedures detailed in Stevenson et al. (2014b); Stevenson and Fowler (2019) using the same exact orbital parameters used in (Mancini et al., 2019) and this work. Independently analyzed WFC3 G141 spectrum from KS is consistent with this work and WFC3 offset 2 version from Luque et al. (2020) and also has a large offset compared to Mancini et al. (2019).

Our Spitzer points are lower than reported in Luque et al. (2020) with channel 1 ($\sim 3\sigma$ lower) having a larger offset than channel 2 ($\sim 2\sigma$ lower). This could be due to the different choices of the minutes of data trimmed at the start of the observation and the ramp models. As shown in Figure 3.3, we have extensively explored the different combinations of minutes to trim and ramp models. Our Spitzer spectrum represents transit depths from the best fitted lightcurves.

We also compared our Spitzer eclipse spectrum with Garhart et al. (2020). While the $3.6 \mu m$ point is in agreement, our $4.5 \mu m$ point is lower by $\sim 2.5\sigma$. Garhart et al. (2020) used orbital parameters from the discovery paper (Hellier et al., 2015) and we used the ones from Mancini et al. (2019) to be consistent with the rest of this study.

Table 3.5.

Parameter	Priors	Posteriors	Best fit
T	$\mathcal{U}(950, 1900)$	1288^{+282}_{-228}	1557
$R_{pl}(\text{Jup})$	$\mathcal{U}(1.1232, 1.404)$	$1.33^{+0.02}_{-0.03}$	1.34
$\log f_{scatter}$	$\mathcal{U}(0, 10)$	$6.68^{+1.50}_{-1.89}$	3.97
$\log(Z/Z_{\odot})$	$\mathcal{U}(-1, 1)$	$0.03^{+0.61}_{-0.65}$	-0.37
C/O ratio	$\mathcal{U}(0.05, 2)$	$0.85^{+0.72}_{-0.51}$	0.19
$\log P_{cloudtop}$ (Pa)	$\mathcal{U}(0, 8)$	$4.29^{+2.39}_{-2.39}$	7.08
error multiple	$\mathcal{U}(0.5, 5)$	$1.25^{+0.11}_{-0.10}$	1.23
scatter slope	$\mathcal{U}(0, 10)$	$2.81^{+0.94}_{-0.78}$	2.27

Table 3.7.

Parameter	Priors	Posteriors	Best fit
T	$\mathcal{U}(950, 1900)$	1413^{+333}_{-276}	1458
$R_{pl}(\text{Jup})$	$\mathcal{U}(1.1232, 1.404)$	$1.35^{+0.02}_{-0.05}$	1.37
$\log f_{scatter}$	$\mathcal{U}(0, 10)$	$3.79^{+1.68}_{-1.32}$	2.82
$\log(Z/Z_{\odot})$	$\mathcal{U}(-1, 1)$	$-0.08^{+0.66}_{-0.59}$	-0.21
C/O ratio	$\mathcal{U}(0.05, 2)$	$0.67^{+0.76}_{-0.40}$	0.81
$\log P_{cloudtop}$ (Pa)	$\mathcal{U}(0, 8)$	$4.33^{+2.27}_{-2.44}$	7.41
error multiple	$\mathcal{U}(0.5, 5)$	$1.15^{+0.11}_{-0.09}$	1.07
scatter slope	$\mathcal{U}(0, 10)$	$2.23^{+1.33}_{-0.90}$	1.56

Table 3.9.

Parameter	Priors	Posteriors	Best fit
$\log f_{scatter}$	$\mathcal{U}(0, 3)$	$1.0^{+0.79}_{-0.64}$	1.16
$\log(Z/Z_{\odot})$	$\mathcal{U}(-1, 3)$	$-0.30^{+0.66}_{-0.46}$	-0.76
C/O ratio	$\mathcal{U}(0.1, 2)$	$1.31^{+0.41}_{-0.26}$	0.90
β	$\mathcal{U}(0, 1.25)$	$0.88^{+0.13}_{-0.16}$	0.46
$\log \kappa_{IR}$	$\mathcal{U}(-4, -0.5)$	$-1.80^{+0.44}_{-0.68}$	-1.20
$\log \gamma$	$\mathcal{U}(-3, 0.5)$	$-0.80^{+0.28}_{-0.37}$	-2.01

Table 3.11.

Parameter	Priors	Posteriors	Best fit
$\log f_{scatter}$	$\mathcal{U}(0, 3)$	$1.03^{+0.74}_{-0.62}$	0.86
$\log(Z/Z_{\odot})$	$\mathcal{U}(-1, 3)$	$-0.28^{+0.86}_{-0.49}$	0.03
C/O ratio	$\mathcal{U}(0.1, 2)$	$0.92^{+0.30}_{-0.06}$	0.92
β	$\mathcal{U}(0, 1.25)$	$0.86^{+0.16}_{-0.18}$	0.87
$\log \kappa_{IR}$	$\mathcal{U}(-4, -0.5)$	$-1.86^{+0.45}_{-0.70}$	-2.09
$\log \gamma$	$\mathcal{U}(-3, 0.5)$	$-0.88^{+0.33}_{-0.43}$	-0.86

3.7 PLATON retrieval

3.7.1 Transit retrieval

We performed a retrieval analysis with PLATON (Zhang et al., 2020) on both uniformly analyzed transit (Table. 3.12) and eclipse (Table. 5.1) spectra of WASP-74b. All retrievals were conducted with opacity sampling at $R=1000$ and 1000 live points. Our setup for the transit retrieval is shown in Table 3.6 with seven free parameters assuming equilibrium chemistry and including condensation. The best-fit PLATON retrieval model with a χ^2_{ν} of 1.59 is shown in Figure 3.7. The model shows a very muted $1.4 \mu m$ water feature accompanied with a strong scattering slope extending from the optical to infrared.

We found metallicity and C/O ratio consistent with solar values (Figure 3.15). The retrieved limb averaged temperature from the transit spectrum based on 1D models is typically lower compared to the equilibrium temperature in hot Jupiters. This is because atmospheric circulation causes an always colder western limb to the eastern limb (Showman et al., 2009) and 1D models retrieve a single uniform temperature for both limbs which could be biased towards lower temperature by several hundred degrees (MacDonald et al., 2020). In the colder western limb, aluminum and

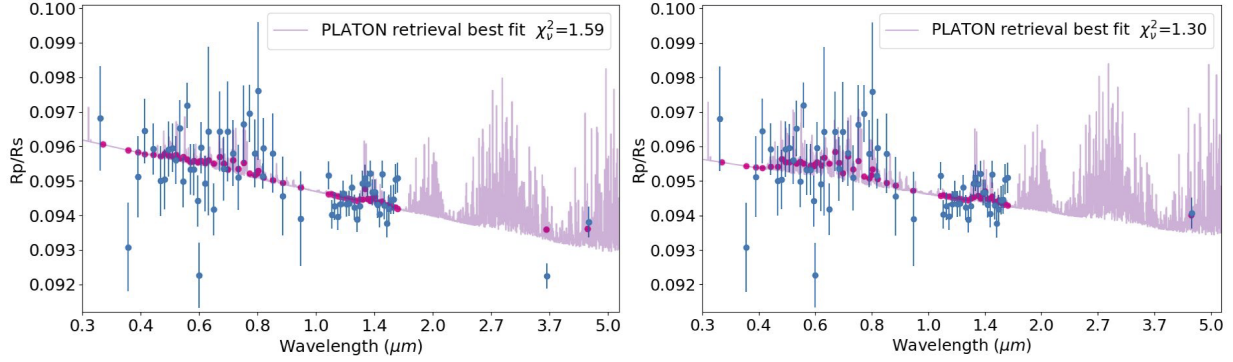


Figure 3.7 Best-fit PLATON retrieval of WASP-74b transit spectrum. Purple line is the full resolution model with pink dots for corresponding binned model. Left panel uses the full spectrum and the right panel excludes the $3.6 \mu m$ point. We see strong scattering with muted water feature and no evidence for TiO absorption or super-Rayleigh scattering in both retrievals. However, the low $3.6 \mu m$ point does drive up the cloud scattering factor.

silicate based aerosols can form under these cooler environments which lead to strong scattering effect and muted molecular absorption features (Muñoz and Isaak, 2015; Parmentier et al., 2016).

We also performed a retrieval using the same priors but without the $3.6 \mu m$ Spitzer point (Figure 3.7). The Spitzer channel 1 transit depth can vary by several hundred ppm based on the trimming choice at the beginning of the lightcurve (Figure 3.3). Excluding the $3.6 \mu m$ point allows us to investigate if our retrieval result hinges on this one data point. The low transit depth of the $3.6 \mu m$ point does drive up the retrieved log scattering factor (Table 3.6 & 3.6) from $3.79^{+1.68}_{-1.32}$ to $6.68^{+1.50}_{-1.89}$ as expected since a stronger scattering is needed to fit for the steeper slope. However, all other retrieved parameters stay consistent with or without the $3.6 \mu m$ point.

3.7.2 Eclipse retrieval

For the eclipse retrieval we also assumed equilibrium chemistry with a total of six free parameters (Table 4.5) including three TP profile parameters (Line et al., 2013). The T_{int} is set to 100K. The best-fit model with a χ^2_ν of 1.47 is shown in Figure 3.6 and the TP profile is shown in

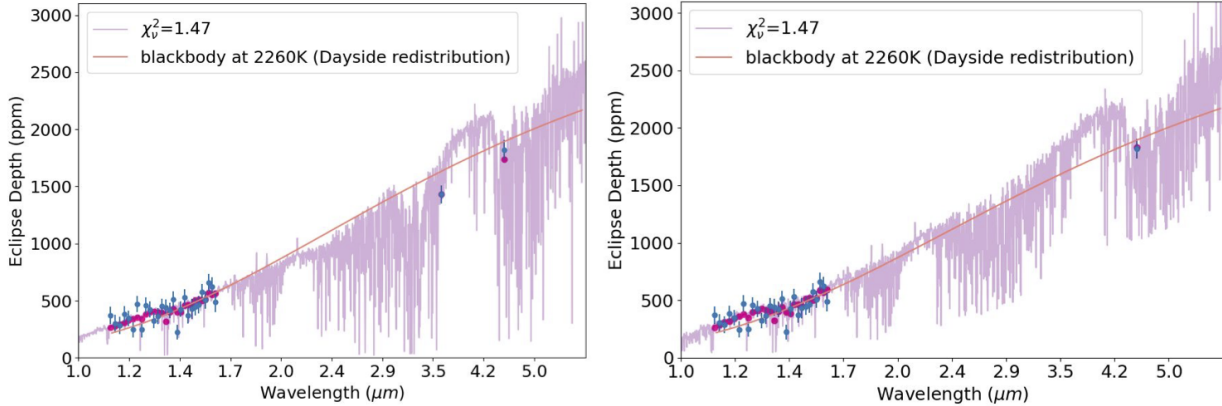


Figure 3.8 Best-fit PLATON retrieval of WASP-74b eclipse spectrum. Left panel uses the full spectrum and the right panel excludes the $3.6 \mu m$ point. Purple line is the full resolution model with pink dots for corresponding binned model and overplotted with blackbody at 2260K in orange represent dayside only heat redistribution. In the full spectrum (left), we see a featureless blackbody-like WFC3/G141 spectrum with a methane absorption feature at $3.6 \mu m$ band. Without the $3.6 \mu m$ point (right), the methane absorption feature disappears and the retrieved C/O ratio drops significantly.

Figure 3.9 with dash lines indicating one sigma uncertainty. The WFC3/G141 emission spectrum is very close to blackbody-like with a potentially weak water absorption feature. The Spitzer $3.6 \mu m$ point is $\sim 3\sigma$ lower than a blackbody of 2260K assuming dayside heat redistribution which indicates a possible molecular absorption features. The strongest opacity source covered by the $3.6 \mu m$ band is CH_4 . Although large quantities of methane is unlikely to exist under a dayside temperature $> 2000K$, some amount could be present in the higher altitude and cooler environment combined with a high C/O ratio atmosphere (Moses et al., 2013).

The emission spectrum probes deeper into the atmosphere at around 1-5 bar and the retrieved decreasing TP profile at those pressure levels is consistent within one sigma compared to what we expect from dayside heat redistribution (2260K) on WASP-74b. The retrieved high C/O ratio of 1.31 is surprising since it would indicate very low water abundance with high abundance carbon bearing species such as CO and CH_4 . We believe this high C/O ratio is driven by the featureless

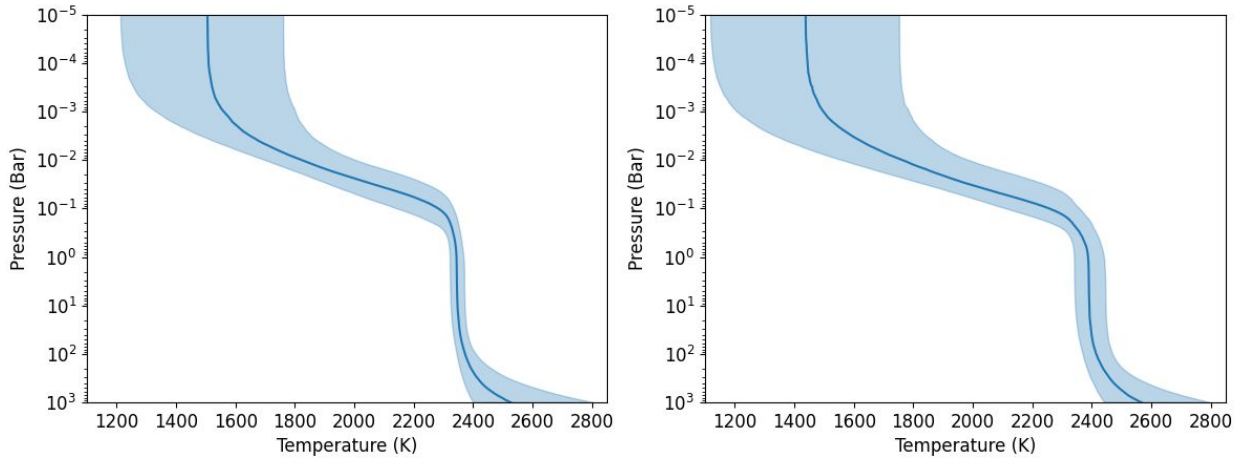


Figure 3.9 TP profile from PLATON eclipse retrieval with the solid line as the median values and shaded regions representing one sigma uncertainty. Left panel uses the full spectrum and the right panel excludes the $3.6 \mu m$ point. The TP profiles are highly consistent showing the thermal structure is not sensitive to the one $3.6 \mu m$ point.

G141 spectrum combined with the low Spitzer $3.6 \mu m$ point. This combination led to a low water abundance solution which suppresses the water absorption feature one would expect in a decreasing TP profile while maintaining the methane absorption feature in the Spitzer channel 1 band.

We believe three potential causes could have explained this unusually high C/O ratio indicated by the emission spectrum. One would be the reliability of Spitzer $3.6 \mu m$ point which has been shown to be challenging to analyze due to the more complex instrument systematics compared to the $4.5 \mu m$ channel (May and Stevenson, 2020). A higher $3.6 \mu m$ point with no methane absorption feature would indicate a more isothermal TP profile which would not need an extremely low water abundance to fit the featureless G141 spectrum. Another cause could be the present of an unknown opacity source in the G141 band masking out the water absorption feature. We know H- can have this effect (Arcangeli et al., 2019; Lothringer et al., 2018; Parmentier et al., 2018), but it only exists in ultra-hot Jupiters ($>2500K$) and WASP-74b is not hot enough for H-

to become a dominant opacity source. We have ran the retrievals with H- turned on and off and there are no changes on the retrieval results. High C/O ratio could also be due to planet formation beyond the snowline where the oxygen was locked up in the water ice while carbon was still free as CO in the gaseous phase (Madhusudhan, 2012; Oberg et al., 2011).

We also performed a retrieval on the emission spectrum without the 3.6 μm point to see how much this one data point affects the retrieval result. The C/O ratio drops significantly (Table 4.5 & 3.6) from $1.31^{+0.41}_{-0.26}$ to $0.92^{+0.30}_{-0.06}$ showing the low 3.6 μm point is driving up the methane abundance and thus the C/O ratio. All other parameters and the TP profile stayed consistent.

3.8 Follow up observations with JWST

The surprisingly high C/O ratio retrieval from the eclipse spectrum calls for JWST follow up observations with extended wavelength coverage. Eclipse observations with NIRSpec G235 and G395 would cover multiple infrared features from CH₄, H₂O, CO, and CO₂ which would allow us to precisely constrain the C/O ratio. For the transit spectrum, NIRISS SOSS will be able to confirm the strong scattering slope which extends from the optical into the infrared and better characterize the aerosol properties.

WASP-74b sits in an interesting transition parameter space between hot Jupiters and ultra-hot Jupiters where molecular features are not yet fully diminished by thermal dissociation and continuum opacity sources like H-, but high altitude aerosols can still linger to flatten the spectrum. Follow up studies of WASP-74b with JWST will better our understanding of hot Jupiters atmospheres in general and how their atmospheres change as they transition into ultra-hot Jupiters.

3.9 Conclusion

We observed 6 transits and 3 eclipses of the hot Jupiter WASP-74b with HST STIS/WFC3 and Spitzer. All datasets were uniformly analyzed with the same orbital parameters and limb darkening coefficients to ensure the consistency between different instruments. We have compared our transit spectrum with previous studies and we found no evidence for neither strong TiO/VO absorption in the optical as reported in [Mancini et al. \(2019\)](#) nor super-Rayleigh scattering slope from [Luque et al. \(2020\)](#). Instead we found a muted water feature with strong aerosol scattering extending from the optical into the infrared. Both metallicity and C/O ratio are consistent to the solar values within one sigma.

The eclipse retrieval results were more surprising with the preferred high C/O driven by possible CH₄ absorption feature in the Spitzer 3.6 μm band. However, this result is highly sensitive to a single Spitzer data point and future JWST follow-up observations are needed for further investigations. WASP-74b exhibits significantly different spectra compared to WASP-76b showing temperature as a determining factor for exoplanet atmospheres. As temperature decreases, aerosols start to mute atmospheric features and heavy metals condense out of the atmosphere.

3.10 Appendix

The appendix includes the reduced lightcurves with final spectrum and PLATON retrieval posteriors for both transmission and eclipse observations. For the transmission, we have two visits of STIS G430L (Fig. [3.10](#), [3.11](#)), one visit of STIS G750L (Fig. [3.12](#)) and WFC3 G141

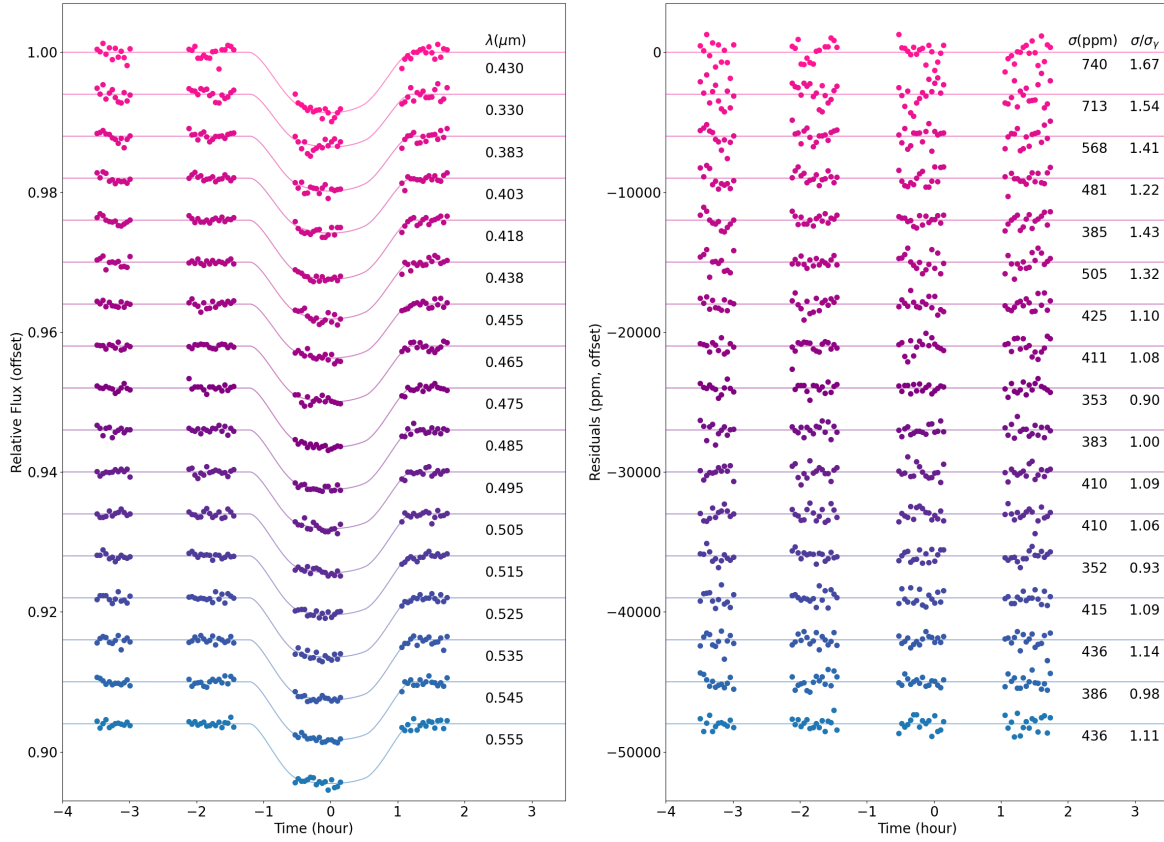


Figure 3.10 HST STIS G430L visit 1 spectral bin transit lightcurves after systematics correction using jitter decorrelation (left) and corresponding residuals (right).

(Fig. 3.13). The final transmission spectrum and limb darkening coefficients are listed in Table 3.12 and Table 3.13. The PLATON retrieval posteriors for transmission spectra with and without the Spitzer 3.6 μm point are shown in Figure 3.15 and 3.16. For the eclipse, we have one visit of WFC3 G141 (Fig. 3.14). The final eclipse spectrum is listed in Table 5.1. The PLATON retrieval posteriors for eclipse spectra with and without the Spitzer 3.6 μm point are shown in Figure 3.17 and 3.18.

Table 3.12: WASP-74b transit spectrum

Wavelength midpoint (μm)	Bin width (μm)	Rp/Rs	Rp/Rs uncertainty (1 sigma)
0.330	0.0400	0.0968	0.001516
0.382	0.0125	0.0931	0.001286

0.403	0.0082	0.0951	0.001172
0.418	0.0069	0.0964	0.000934
0.438	0.0125	0.0959	0.000745
0.455	0.0050	0.0950	0.001013
0.465	0.0050	0.0950	0.000868
0.475	0.0050	0.0959	0.000803
0.485	0.0050	0.0960	0.000705
0.495	0.0050	0.0956	0.000694
0.505	0.0050	0.0965	0.000807
0.515	0.0050	0.0950	0.000749
0.525	0.0050	0.0972	0.000655
0.535	0.0050	0.0953	0.000738
0.545	0.0050	0.0953	0.000743
0.555	0.0050	0.0944	0.000738
0.560	0.0100	0.0923	0.000937
0.565	0.0050	0.0960	0.000748
0.579	0.0089	0.0949	0.000797
0.589	0.0012	0.0964	0.002440
0.605	0.0148	0.0942	0.000749
0.625	0.0050	0.0964	0.001160
0.637	0.0075	0.0954	0.000921
0.652	0.0075	0.0964	0.001451
0.670	0.0100	0.0958	0.000948
0.690	0.0100	0.0951	0.000946
0.710	0.0100	0.0966	0.001130
0.733	0.0125	0.0969	0.000826
0.755	0.0098	0.0958	0.000977
0.769	0.0047	0.0976	0.001994
0.788	0.2425	0.0951	0.000368
0.791	0.0190	0.0960	0.000856
0.830	0.0200	0.0958	0.001150
0.875	0.0250	0.0946	0.001138
0.965	0.0650	0.0939	0.001373
1.119	0.0093	0.0952	0.000404
1.138	0.0093	0.0940	0.000406
1.156	0.0093	0.0943	0.000401
1.175	0.0093	0.0940	0.000392
1.194	0.0093	0.0943	0.000384
1.212	0.0093	0.0946	0.000375
1.231	0.0093	0.0943	0.000371
1.249	0.0093	0.0943	0.000370
1.268	0.0093	0.0948	0.000371
1.287	0.0093	0.0942	0.000367
1.305	0.0093	0.0939	0.000373
1.324	0.0093	0.0943	0.000369

1.342	0.0093	0.0949	0.000368
1.361	0.0093	0.0951	0.000377
1.380	0.0093	0.0949	0.000386
1.398	0.0093	0.0952	0.000374
1.417	0.0093	0.0947	0.000371
1.435	0.0093	0.0947	0.000382
1.454	0.0093	0.0943	0.000379
1.473	0.0093	0.0940	0.000391
1.491	0.0093	0.0952	0.000395
1.510	0.0093	0.0943	0.000403
1.528	0.0093	0.0938	0.000407
1.547	0.0093	0.0942	0.000406
1.566	0.0093	0.0944	0.000411
1.584	0.0093	0.0945	0.000426
1.603	0.0093	0.0951	0.000436
1.621	0.0093	0.0951	0.000433
3.600	0.3800	0.0922	0.000369
4.500	0.5600	0.0938	0.000448

Table 3.13: Transit spectrum LD coefficients

Wavelength midpoint (μm)	C1	C2	C3	C4
0.330	0.2705	0.3265	0.6655	-0.3603
0.382	0.4105	0.0432	0.8133	-0.3888
0.403	0.3063	0.3801	0.4784	-0.2826
0.418	0.2976	0.4093	0.3791	-0.2082
0.438	0.4077	0.3480	0.2256	-0.1518
0.455	0.3666	0.2493	0.5645	-0.3223
0.465	0.3696	0.3956	0.2662	-0.1798
0.475	0.3562	0.5642	-0.0569	-0.0223
0.485	0.4561	0.4177	0.0456	-0.0988
0.495	0.4121	0.4911	-0.0624	-0.0201
0.505	0.4444	0.3578	0.0620	-0.0501
0.515	0.3952	0.3677	0.1715	-0.1388
0.525	0.4643	0.3587	0.0349	-0.0625
0.535	0.4823	0.3079	0.1146	-0.1165
0.545	0.4839	0.3177	0.0417	-0.0598
0.555	0.5090	0.2242	0.1408	-0.0968
0.560	0.5141	0.2312	0.1016	-0.0735
0.565	0.5190	0.2377	0.0652	-0.0518
0.579	0.5348	0.2233	0.0450	-0.0415
0.589	0.5811	-0.0467	0.5043	-0.2957
0.605	0.5625	0.1408	0.1077	-0.0683

0.625	0.5922	0.0536	0.1836	-0.1021
0.637	0.5855	0.0663	0.1626	-0.0940
0.652	0.6241	0.0128	0.1621	-0.0985
0.670	0.6058	0.0120	0.1747	-0.0921
0.690	0.6179	-0.0367	0.2073	-0.1001
0.710	0.6250	-0.0672	0.2241	-0.1041
0.733	0.6208	-0.0718	0.2233	-0.1084
0.755	0.6350	-0.1154	0.2477	-0.1146
0.769	0.6357	-0.1366	0.2639	-0.1211
0.788	0.6053	-0.0234	0.1975	-0.0987
0.791	0.6397	-0.1459	0.2567	-0.1149
0.830	0.6343	-0.1428	0.2275	-0.1000
0.875	0.6555	-0.2478	0.3210	-0.1341
0.965	0.6439	-0.2223	0.2747	-0.1175
1.119	0.6370	-0.2190	0.1870	-0.0668
1.138	0.6340	-0.2280	0.1960	-0.0718
1.156	0.6280	-0.1970	0.1500	-0.0514
1.175	0.6390	-0.2200	0.1660	-0.0594
1.194	0.6250	-0.1740	0.1070	-0.0324
1.212	0.6280	-0.1790	0.0984	-0.0258
1.231	0.6290	-0.1670	0.0776	-0.0201
1.249	0.6350	-0.1770	0.0841	-0.0242
1.268	0.6390	-0.1690	0.0600	-0.0120
1.287	0.6680	-0.2030	0.0294	0.0052
1.305	0.6460	-0.1590	0.0220	0.0075
1.324	0.6520	-0.1700	0.0268	0.0075
1.342	0.6630	-0.1770	0.0152	0.0147
1.361	0.6660	-0.1820	0.0128	0.0171
1.380	0.6910	-0.2130	0.0192	0.0190
1.398	0.7010	-0.2280	0.0178	0.0241
1.417	0.7210	-0.2570	0.0378	0.0165
1.435	0.7290	-0.2800	0.0469	0.0187
1.454	0.7500	-0.3260	0.0930	-0.0039
1.473	0.7880	-0.3770	0.1120	-0.0026
1.491	0.7960	-0.4150	0.1440	-0.0102
1.510	0.8280	-0.4930	0.2160	-0.0380
1.528	0.8600	-0.5370	0.2280	-0.0310
1.547	0.8810	-0.6060	0.2970	-0.0573
1.566	0.8890	-0.6450	0.3380	-0.0694
1.584	0.8270	-0.5490	0.2740	-0.0540
1.603	0.9480	-0.8340	0.5450	-0.1550
1.621	0.9440	-0.7890	0.4750	-0.1210
3.600	0.4958	-0.4478	0.3558	-0.1170
4.500	0.4255	-0.3651	0.2867	-0.0945

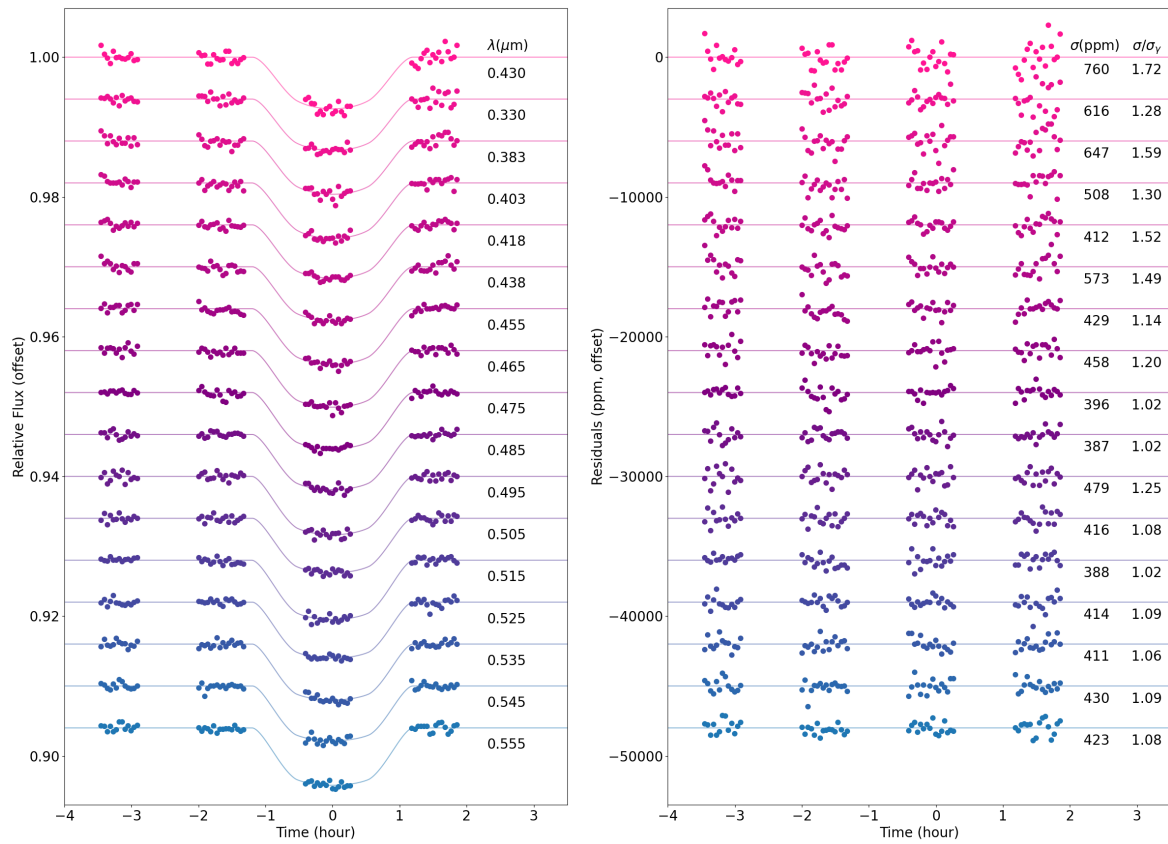


Figure 3.11 HST STIS G430L visit 2 spectral bin transit lightcurves after systematics correction using jitter decorrelation (left) and corresponding residuals (right).

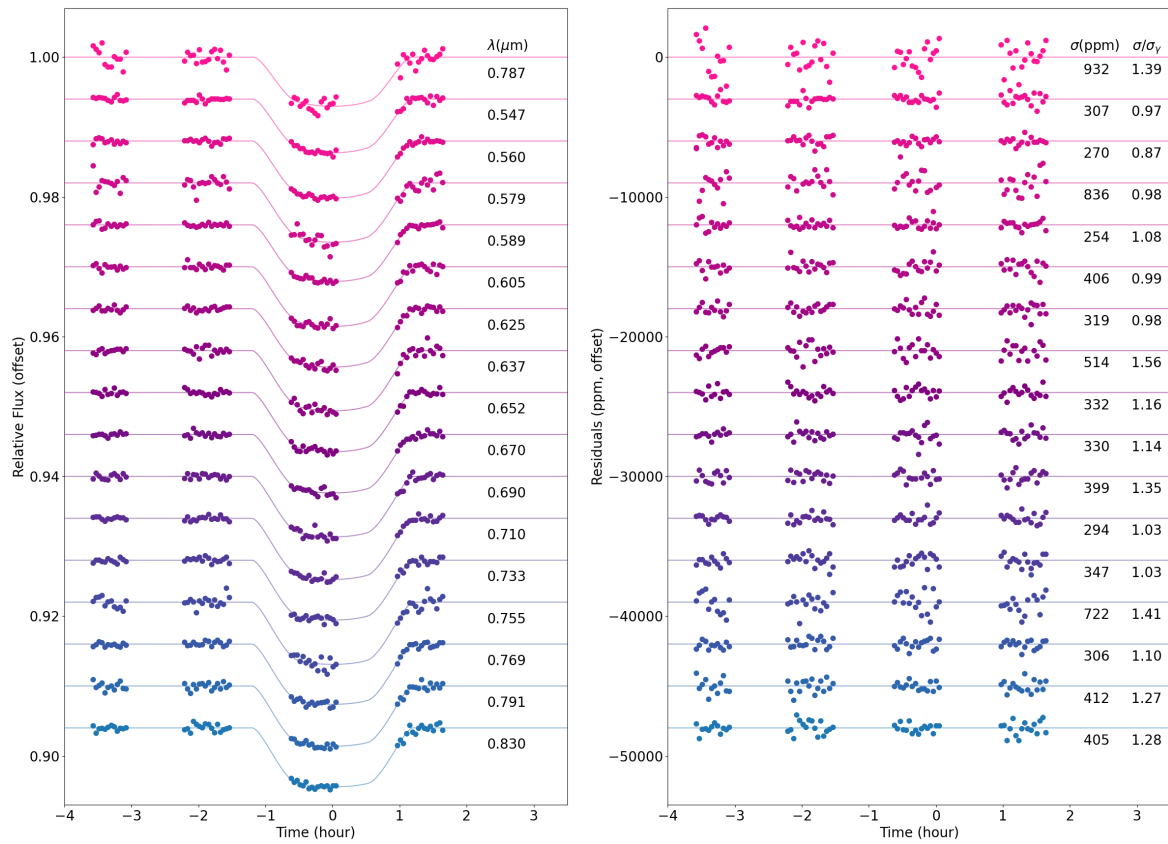


Figure 3.12 HST STIS G750L spectral bin transit lightcurves after systematics correction using jitter decorrelation (left) and corresponding residuals (right).

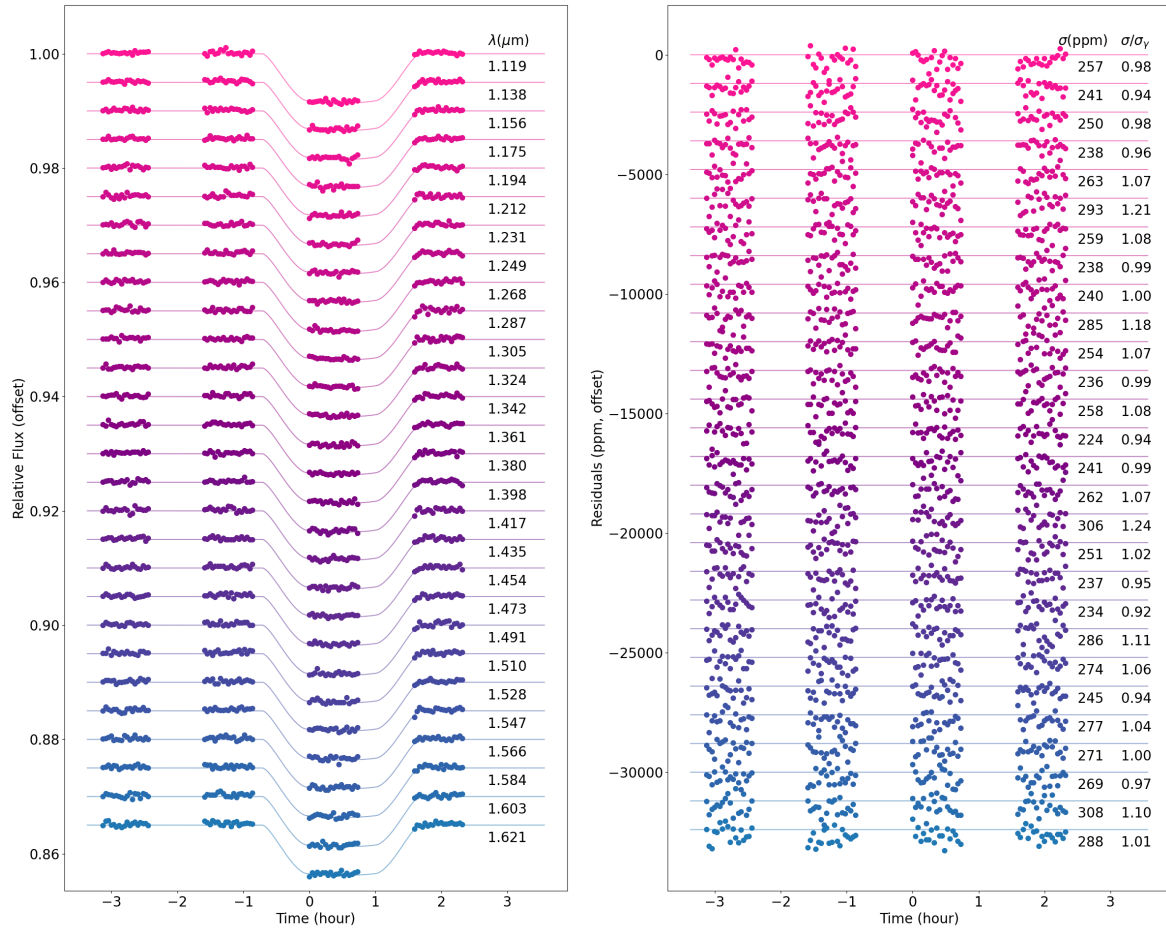


Figure 3.13 HST WFC3 G141 spectral bin transit lightcurves after ramp-effect correction using RECTE (left) and corresponding residuals (right).

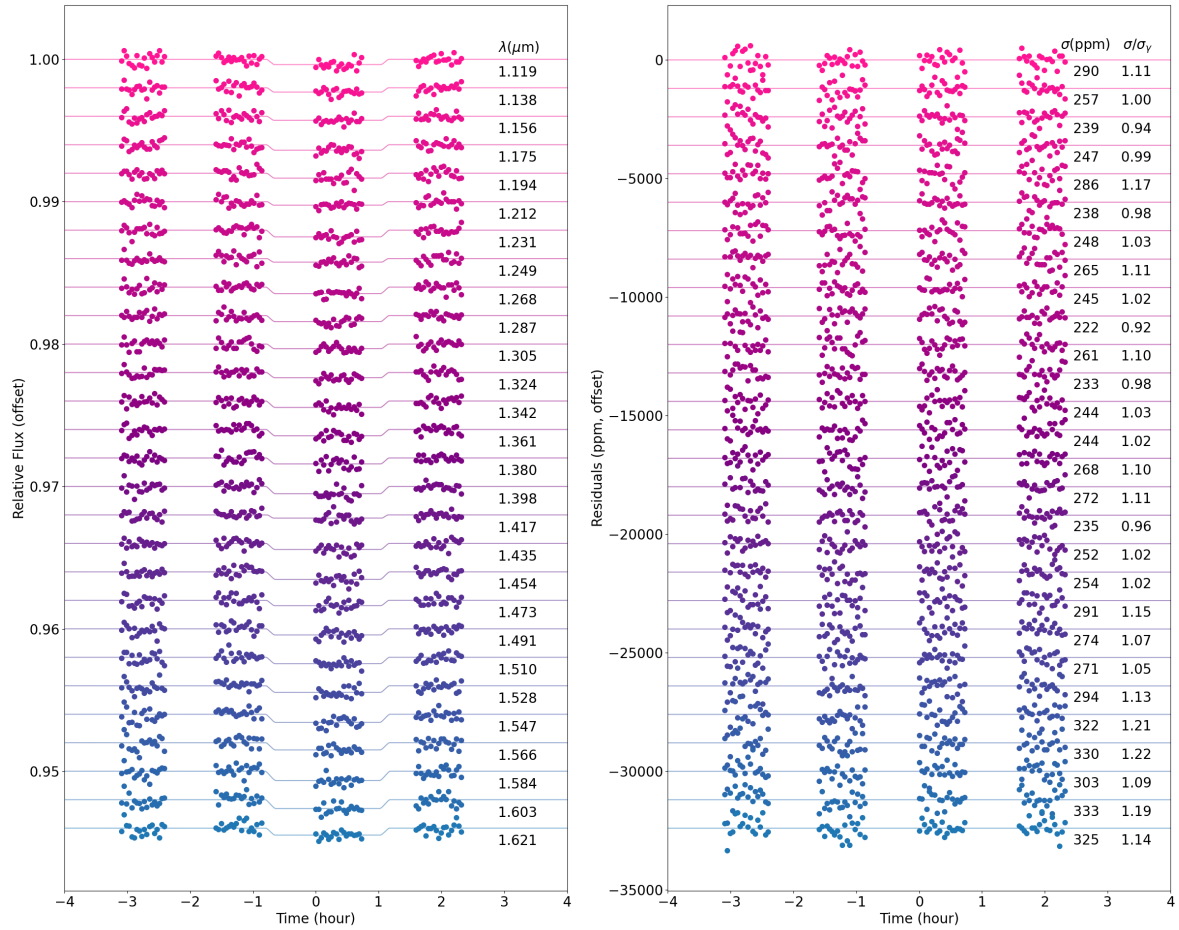


Figure 3.14 HST WFC3 G141 spectral bin eclipse lightcurves after ramp-effect correction using RECTE (left) and corresponding residuals (right).

Table 3.14: WASP-74b eclipse spectrum

Wavelength midpoint (μm)	Bin width (μm)	Occultation Depth (ppm)	Uncertainty 1-sigma (ppm)
1.1193	0.0093	372	76
1.1379	0.0093	302	73
1.1564	0.0093	284	74
1.1751	0.0093	385	70
1.1937	0.0093	346	68
1.2123	0.0093	246	70
1.2309	0.0093	473	69
1.2494	0.0093	247	67
1.2681	0.0093	460	68
1.2867	0.0093	426	70
1.3053	0.0093	326	67
1.3238	0.0093	365	69
1.3424	0.0093	452	68
1.3611	0.0093	442	73
1.3797	0.0093	418	67
1.3982	0.0093	513	69
1.4168	0.0093	224	63
1.4354	0.0093	427	68
1.4541	0.0093	529	71
1.4727	0.0093	373	71
1.4912	0.0093	431	87
1.5098	0.0093	448	74
1.5284	0.0093	465	75
1.5471	0.0093	574	75
1.5656	0.0093	506	75
1.5842	0.0093	659	79
1.6028	0.0093	624	79
1.6214	0.0093	489	85
3.6000	0.3800	1430	81
4.5000	0.5600	1820	85

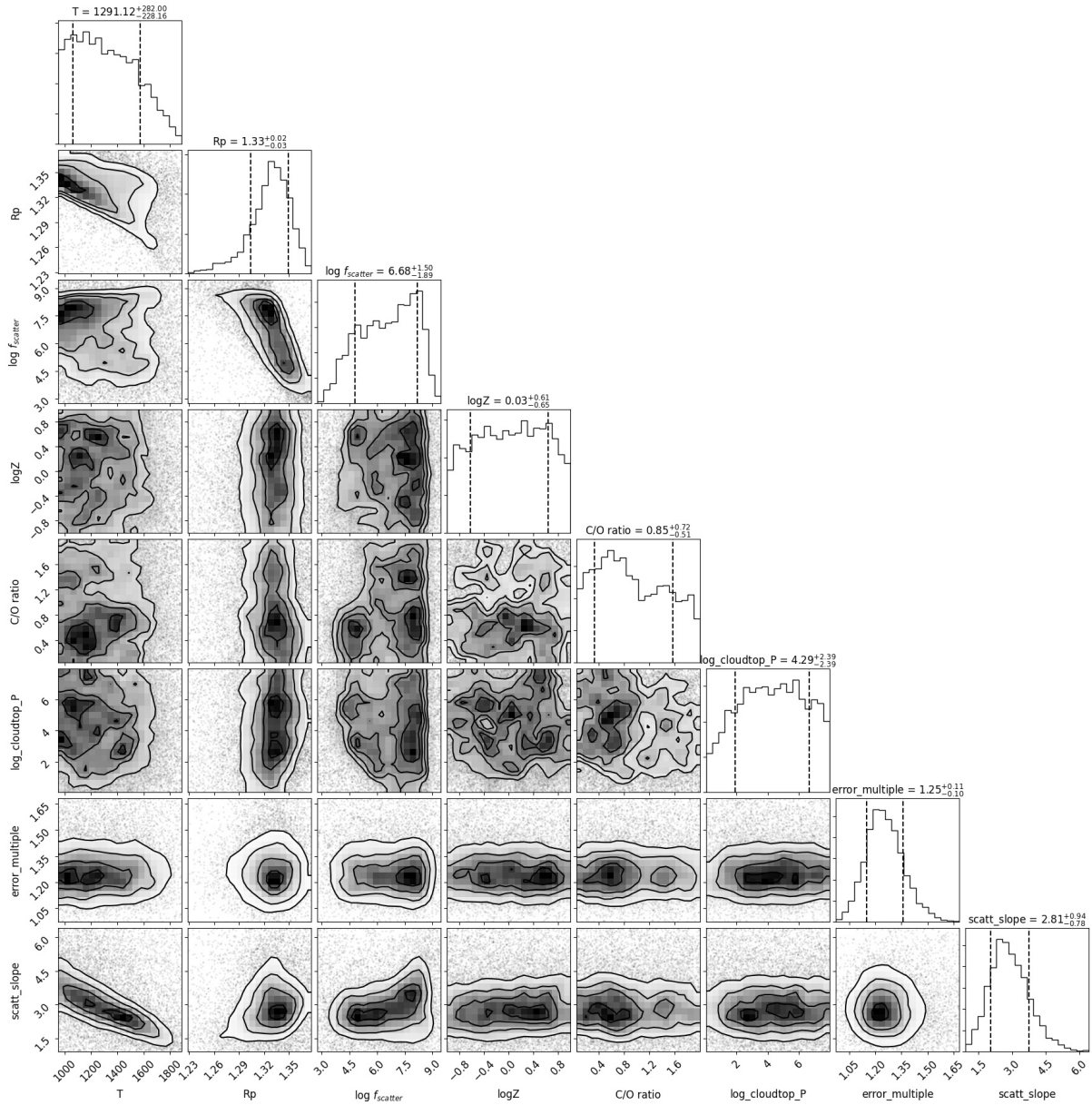


Figure 3.15 Posterior distribution of PLATON retrieval on the transit spectrum.

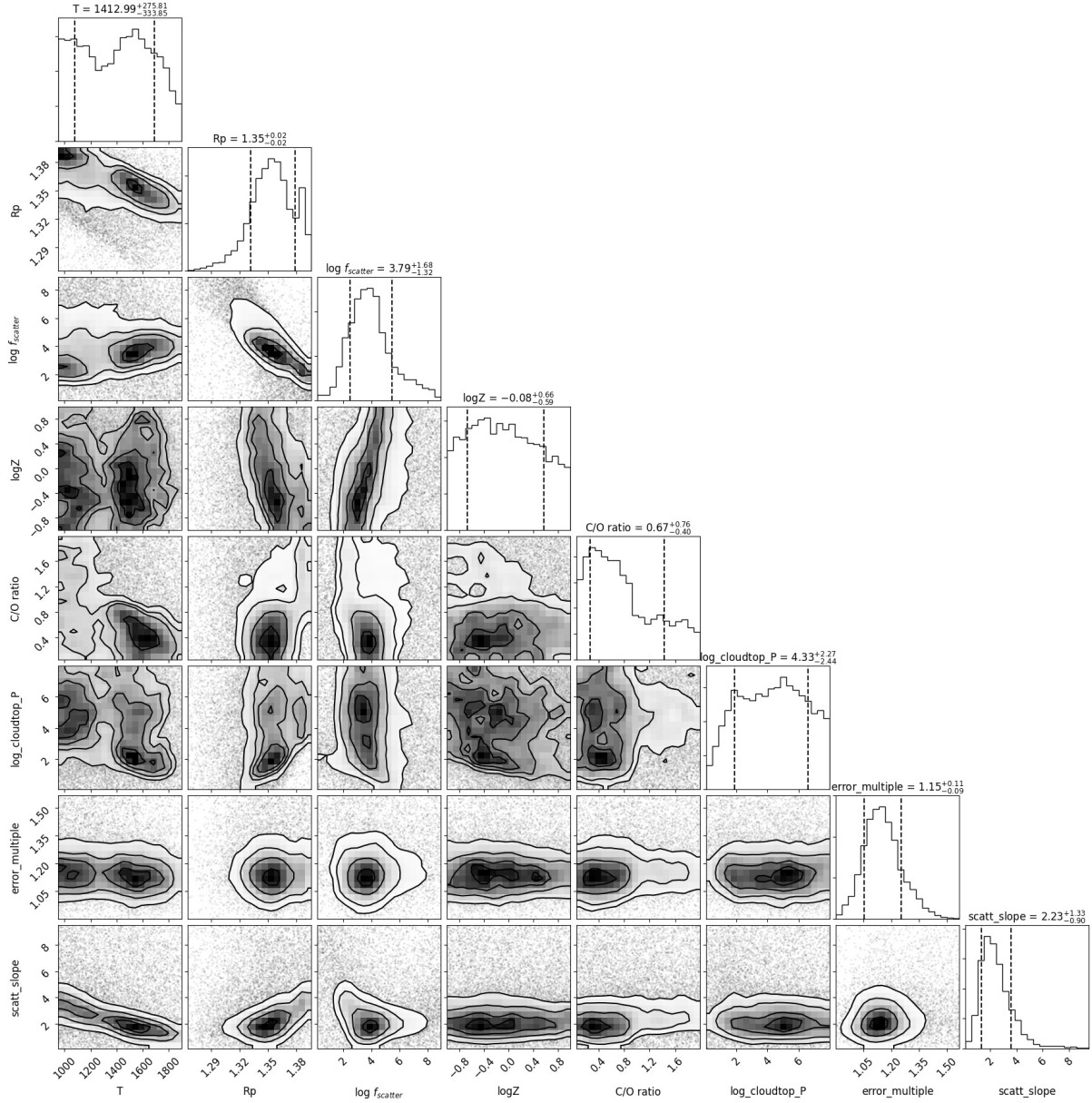


Figure 3.16 Posterior distribution of PLATON retrieval on the transit spectrum without the Spitzer $3.6 \mu\text{m}$ point.

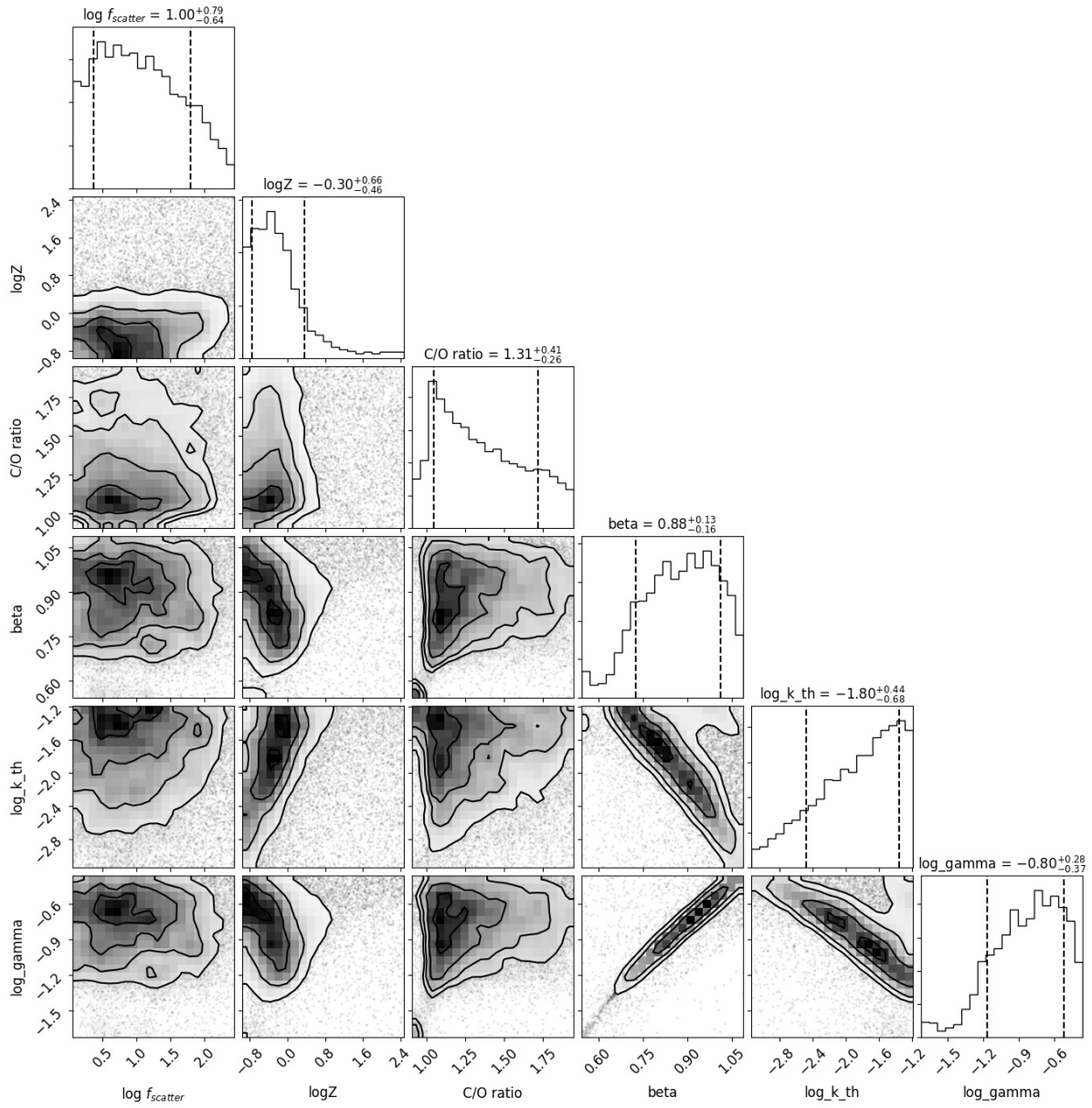


Figure 3.17 Posterior distribution of PLATON retrieval on the eclipse spectrum.

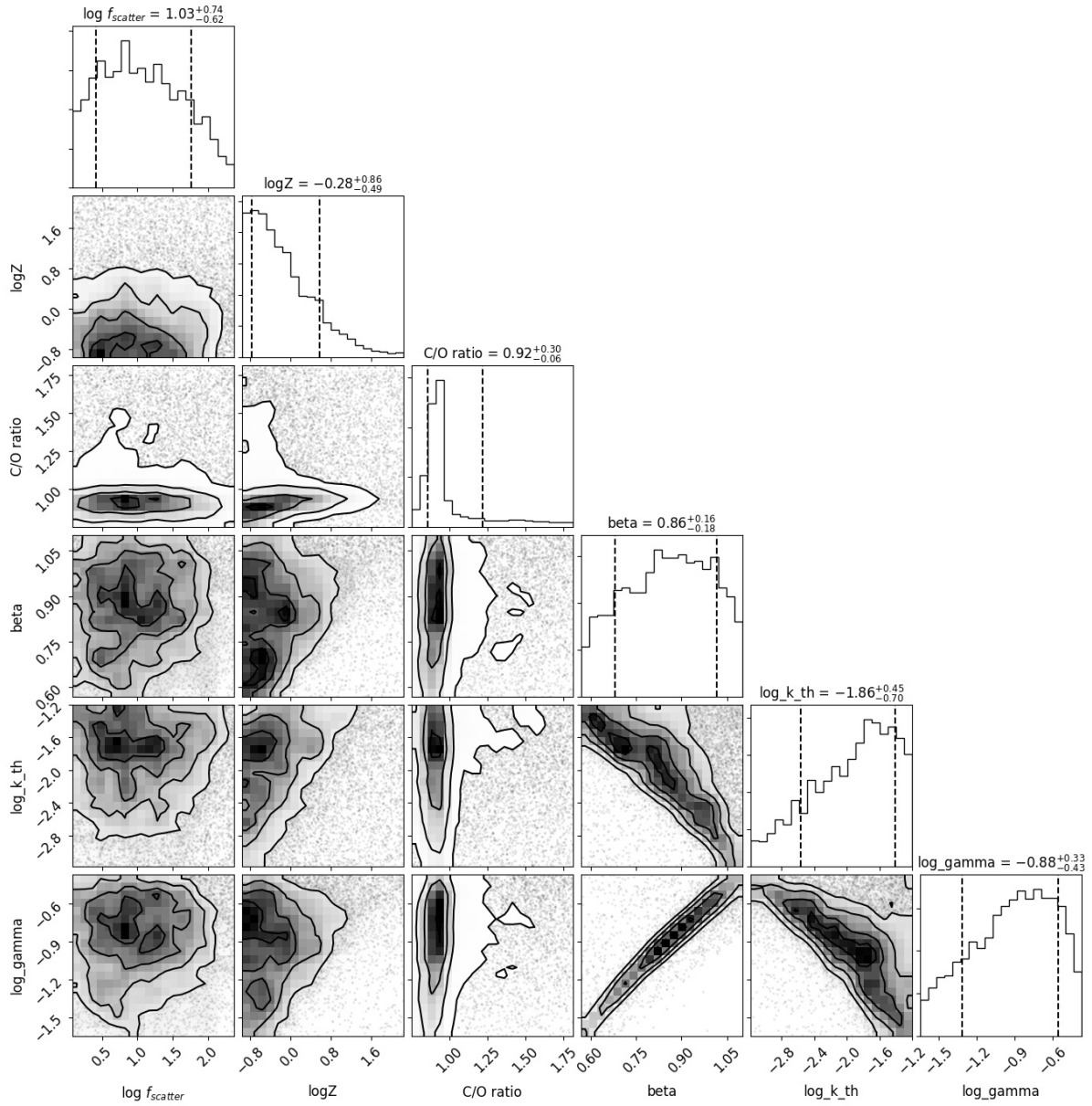


Figure 3.18 Posterior distribution of PLATON retrieval on the eclipse spectrum without the Spitzer $3.6 \mu m$ point.

Chapter 4: Emission spectrum of hot Jupiter HAT-P-41b

4.1 Overview

We present the most complete emission spectrum for inflated hot Jupiter HAT-P-41b combining new HST WFC/G141 spectrum from the Hubble Panchromatic Comparative Exoplanet Treasury (PanCET) program with archival Spitzer eclipse observations. We found a near blackbody-like emission spectrum which is best fitted with an isothermal temperature-pressure (TP) profile that agrees well with the dayside heat redistribution scenario assuming zero Bond albedo. The non-inverted TP profile is consistent with the non-detection of NUV/optical absorbers in the transit spectra. We do not find any evidence for significant H^- opacity nor a metal-rich atmosphere. HAT-P-41b is an ideal target that sits in the transitioning parameter space between hot and ultra-hot Jupiters, and future JWST observations will help us to better constrain the thermal structure and chemical composition.

4.2 Introduction

Emission spectroscopy is sensitive to the self-emission of the exoplanetary atmosphere which allows us to probe into the deeper layers (1-10 bar) of the dayside atmosphere compared to transmission spectroscopy which is sensitive to optical depth and measures the upper layers

(~ 1 mbar) of the planetary limbs. The difference in the radiative transfer path geometry means the emission spectrum is much more sensitive to the vertical thermal structure of the planet. Depending on the atmospheric chemical composition and the temperature-pressure profile, molecular absorption or emission features can be imprinted onto the emission spectrum. Notably, water features at $1.4 \mu\text{m}$ (Fu et al., 2017) has been the most robustly detected in both absorption (Kreidberg et al., 2014b) and emission (Evans et al., 2017; Fu et al., 2022b). The presence of H- continuum opacity was inferred in multiple ultra-hot Jupiters (Arcangeli et al., 2019). In the longer wavelength, the CO/CO₂ features were indicated by the deviations of Spitzer photometric points in $3.6 \mu\text{m}$ and $4.5 \mu\text{m}$ channels from the blackbody approximation (Fu et al., 2021; Garhart et al., 2020).

HAT-P-41b is an inflated hot Jupiter ($R=1.685^{+0.076}_{-0.051}R_{Jup}$ $M=0.8^{+0.1}_{-0.1}M_{Jup}$ $T_{eq}=1940^{+38}_{-38}\text{K}$) (Hartman et al., 2012) with detailed atmospheric characterization via transmission spectroscopy (Lewis et al., 2020; Sheppard et al., 2021; Wakeford et al., 2020). The planet shows a high metallicity (Sheppard et al., 2021; Wakeford et al., 2020) atmosphere with increased H- opacity abundance (Lewis et al., 2020). With a dayside temperature of $\sim 2300\text{K}$, HAT-P-41b sits between hot and ultra-hot Jupiters where physical processes such as molecular dissociation and H- opacity are starting to become important (Parmentier et al., 2018). HAT-P-41b allows us to pinpoint the transitional parameter space of various atmospheric processes which makes it a valuable data point in our understanding of hot Jupiter atmospheres on a population level (Baxter et al., 2021; Mansfield et al., 2021). Here we present the 1.1 to $4.5 \mu\text{m}$ emission spectrum of HAT-P-41b with combined data from HST/WFC3 G141 and Spitzer channel 1 and 2.

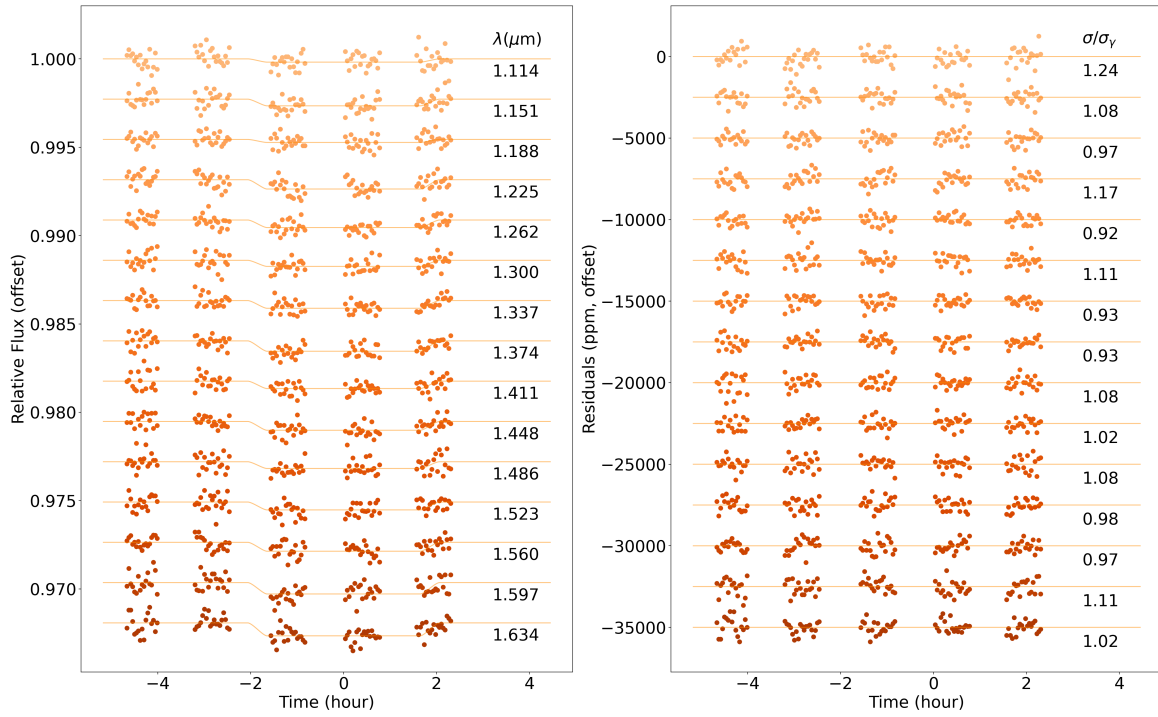


Figure 4.1 HST WFC3 G141 spectral bin transit lightcurves after ramp-effect correction using RECTE (left) and corresponding residuals (right) with their relative ratios to the photon-limit noise (σ/σ_γ) levels.

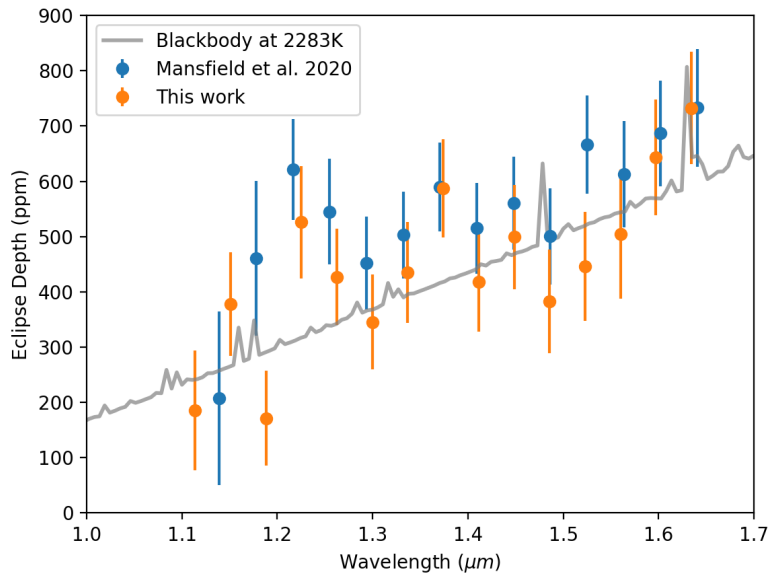


Figure 4.2 The WFC3/G141 emission spectrum of HAT-P-41b is in excellent agreement with Mansfield et al. (2021).

4.3 Observations

The *Hubble* WFC3/G141 dataset was observed as a part of the Panchromatic Exoplanet Treasury Survey (PanCET GO 14767, PIs: Sing & Lopez-Morales) on 2016-10-09 and the *Spitzer* dataset was published in (Garhart et al., 2020). The WFC3/G141 eclipse observation was taken in spatial scan mode for five consecutive HST orbits. Each frame was taken with the 256×256 pixel subarray in the SPARS10 and NSAMP=12 settings. The forward scanning rate is $0.065 \text{ arcsec s}^{-1}$ and the exposure time is 81 seconds.

4.4 HST WFC3 data reduction

All the orbital parameters for the WFC3/G141 data reduction have been fixed to the same values used in (Sheppard et al., 2021) which are identical to what were used in the (Garhart et al., 2020) *Spitzer* analysis.

The data reduction process starts with applying the standard flat field, background subtraction and bad pixels, cosmic rays removal on the ima frames (Fu et al., 2021). Then we extract the non-destructive reads from each frame (Deming et al., 2013). There is a spatially resolved companion star (Sheppard et al., 2021) located 3.6 arcseconds away. Due to the large spatial separation, the non-destructive reads of spatial scan from the two stars do not overlap which allows for clean removal of the companion star spectra. The companion star removed reads are then combined to the complete spatial scan frames. Next we summed each frame in the vertical direction for the 1D spectrum and normalized it by its own median flux to calculate the wavelength shifts. We then used `scipy.interpolate.interp1d` function to interpolate the 1D spectrum in the wavelength

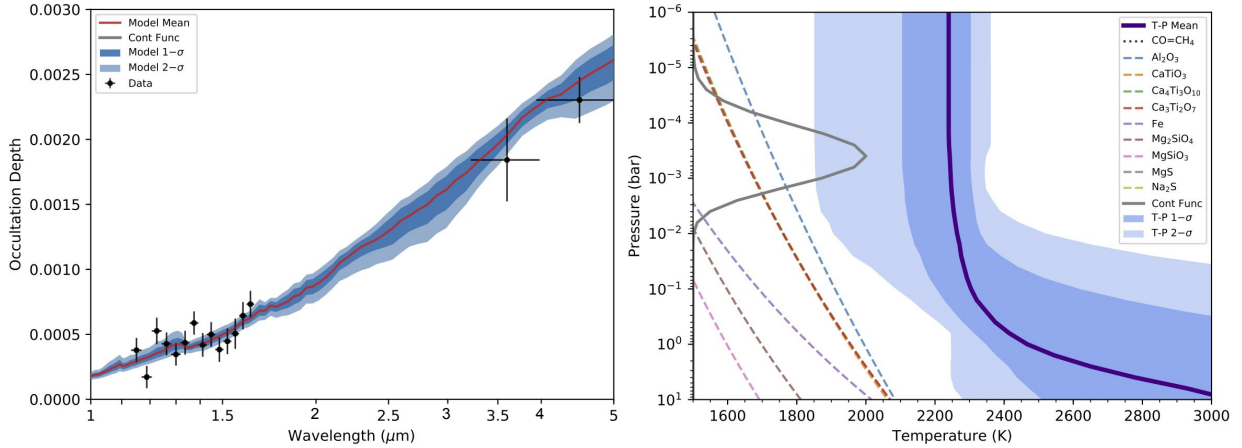


Figure 4.3 ATMO retrieval of HAT-P-41b emission spectrum. The featureless blackbody-like spectrum (left) is best fitted with an isothermal TP profile (right).

direction and calculated the relative sub-pixel level shifts of each frame. The largest shift between any two frames is under 0.1 pixel which does not induce any excessive systematics (Stevenson and Fowler, 2019). Wavelength shifts corrected non-normalized frames were then summed in all wavelength channels to form the whitelight eclipse lightcurve. The lightcurve is then fitted with a combination of BATMAN (Kreidberg, 2015) with the RECTE charge trapping systematics model (Zhou et al., 2017), 2nd order polynomial of the HST orbital phase and the wavelength shifts. Each wavelength channel is then fitted using the same method but with the mid-transit time fixed to the best-fit whitelight value. The best-fit lightcurves of each wavelength channel and corresponding residuals are shown in Figure 4.1.

4.5 Retrieval analysis

We performed the retrieval analysis on the reduced HAT-P-41b emission spectrum (Table. 5.1) with ATMO (Amundsen et al., 2014; Drummond et al., 2016; Goyal et al., 2018; Tremblin et al., 2016, 2015; Wakeford et al., 2017). The retrieval setup is equilibrium chemistry with a fixed

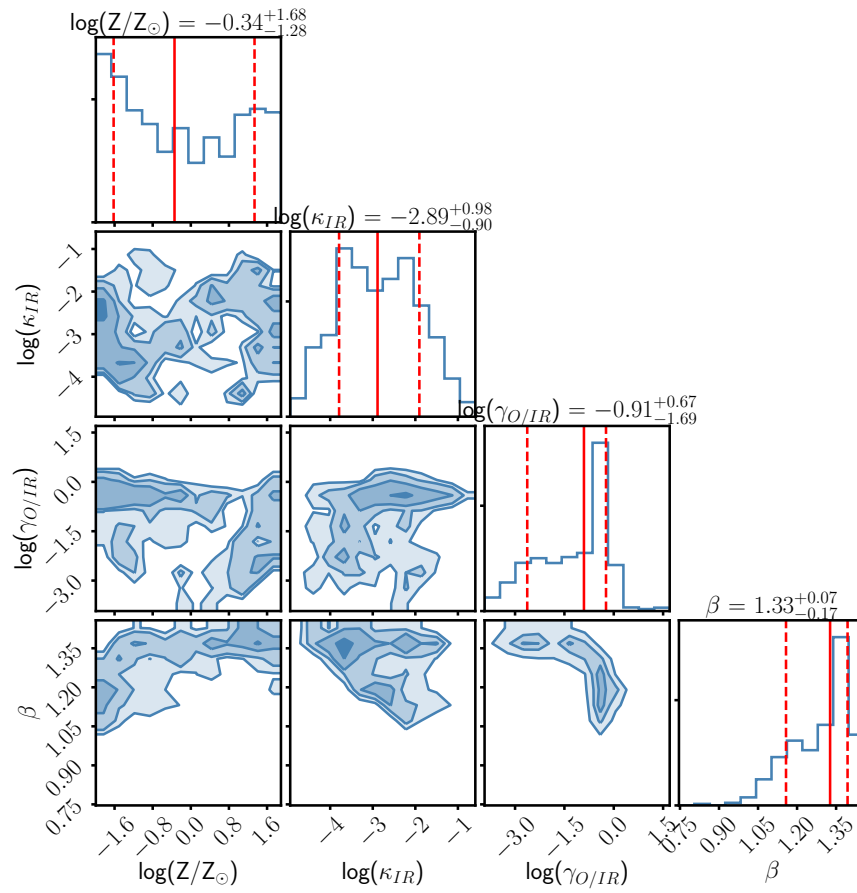


Figure 4.4 Posterior distribution of the ATMO retrieval for HAT-P-41b. The metallicity is mostly unconstrained due to a lack of features within the emission spectrum.

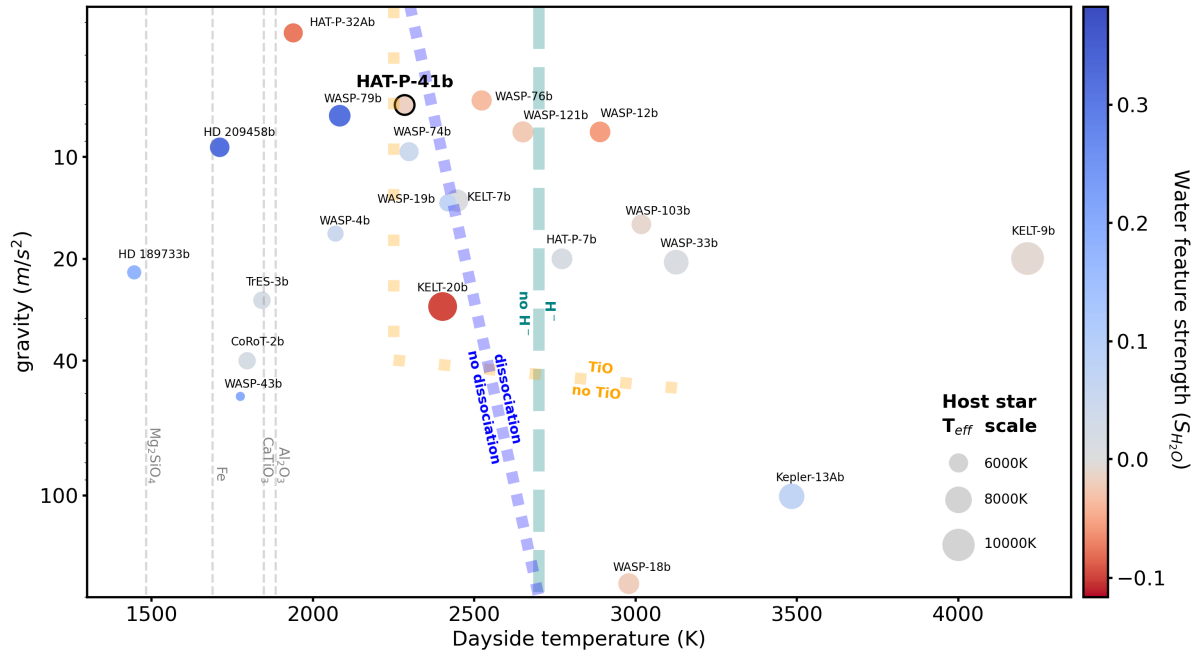


Figure 4.5 HAT-P-41b WFC3/G141 emission spectrum compared with other hot Jupiters. The water feature strength index (S_{H_2O}) (Mansfield et al., 2021) measures the $1.4 \mu m$ water band feature size relative to the blackbody model based on the out-of-band spectrum. Centered at zero being the blackbody-like featureless spectrum. Increasing negative values (redder color) represent stronger emission, features and increasing positive values (bluer color) represent stronger absorption features. The circle size scales with the host star temperature (T_{eff}). The grey vertical dash lines are condensation lines for various metals at 100 mbar assuming solar metallicity. We see mostly featureless spectra at higher dayside temperatures ($>2700K$) where H^- continuum opacity is expected to dominate (Parmentier et al., 2018). At the lower temperature side, we see mostly water absorption features where the atmosphere is too cool for gaseous heavy metal absorbers such as TiO to form and drive thermal inversion. HAT-P-41b sits at this in-between transitional region where planets can have absorption, emission or featureless spectra. Further observations of HAT-P-41b in the longer wavelength with JWST will help us to precisely determine its thermal structure and understand what causes thermal inversion in hot Jupiters atmospheres.

Table 4.2.

Parameter	Priors	Posteriors
$\log(Z/Z)$	$\mathcal{U}(-2.8, 2.8)$	$-0.342^{+1.677}_{-1.277}$
$\log(K_{IR})$	$\mathcal{U}(-5, -0.5)$	$-2.887^{+0.982}_{-0.907}$
$\log(\gamma/IR)$	$\mathcal{U}(-4, 1.5)$	$-0.907^{+0.672}_{-1.716}$
beta	$\mathcal{U}(0, 2)$	$1.326^{+0.068}_{-0.168}$

solar C/O ratio. There is a total of 4 free fitting parameters (Table. 4.5) including metallicity (Z) and three parameters κ_{IR} , $\gamma_{O/IR}$ and β for the temperature-pressure (TP) profile as defined in Line et al. (2013). We fixed the C/O ratio to the solar value due to the lack of constraint this dataset has on the carbon-bearing species. Also, the transit spectra retrieval (Lewis et al., 2020; Sheppard et al., 2021) results were all consistent with the solar C/O values.

The best-fit model to the emission spectrum from the ATMO retrieval (Figure. 4.3) gives a χ^2_ν of 1.24 (4 degrees of freedom) with a near-isothermal TP profile. The best-fit blackbody temperature using the PHOENIX stellar model (Husser et al., 2013) grid ($\log g = 4.5$ and $\log Z = 0$) interpolated to $T_{eff} = 6390$ K is 2283 ± 64 K with a χ^2_ν of 1.23 (1 degree of freedom). Based on the formalism described in (Cowan and Agol, 2011), this dayside temperature would suggest a circulation efficiency ε of 0.44 assuming zero Bond albedo and the predicted nightside temperature would be 1572K. $\varepsilon=0$ represents the no-circulation limit where the nightside temperature is 0K and $\varepsilon=1$ represents the full-circulation scenario where nightside temperature is the same as the dayside. The measured dayside temperature is consistent with the dayside-only heat redistribution scenario. The retrieved metallicity is consistent with the solar value (Figure. 5.3). While Sheppard et al. (2021) retrieved metallicity $\sim 1\sigma$ higher than solar, Lewis et al. (2020) reported values consistent with solar metallicity. Considering the large uncertainties on metallicity from all three studies, the current datasets can not well constrain the models.

[Lewis et al. \(2020\)](#) found H- abundance several orders of magnitude larger than equilibrium chemistry is needed to best fit the transmission spectrum. We did not find evidence for significant H⁻ opacity from the emission spectrum and we believe this could be due to: (1) The blackbody-like emission spectrum and near-isothermal TP profile make the abundances largely unconstrained. (2) The H- constraint in [Lewis et al. \(2020\)](#) comes from a combination of WFC3 G280 and G141 data. [Wakeford et al. \(2020\)](#) did not find evidence for H- solely based on the G280 optical dataset. Therefore any uncorrected offsets between G280 and G141 spectra can potentially lead to high H- abundance. (3) [Sheppard et al. \(2021\)](#) did not retrieve significant H- abundance with both G280 and G141 datasets using a different retrieval code. So it could also be due to different forward model assumptions.

Heavy metals such as Fe I, Fe II, and molecules like TiO are considered major optical absorbers that can induce temperature inversion in hot Jupiter atmospheres ([Fortney et al., 2008](#); [Lothringer et al., 2020](#)), and they have been detected in the optical transit spectrum with HST/STIS G430L and G750L ([Fu et al., 2021](#)). There are no significant NUV heavy metals nor optical TiO absorption detected in both STIS ([Sheppard et al., 2021](#)) and UVIS ([Lewis et al., 2020](#); [Wakeford et al., 2020](#)) transmission spectra for HAT-P-41b. The non-inverted TP profile retrieved in this HAT-P-41b emission spectrum is consistent with the non-detection of NUV/optical absorbers in the transit spectra.

4.6 Compared with other hot Jupiter atmospheres

To quantify the WFC3/G141 emission spectra from various hot Jupiters and compare HAT-P-41b to them, we took the $1.4\mu m$ water feature strength index (S_{H_2O}) reported in [Mansfield](#)

et al. (2021) and plotted them in the dayside temperature versus gravity parameter space (Figure 4.5) first introduced in Parmentier et al. (2018). The important physical transitions including TiO, H⁻, and molecular dissociation are also the same as shown in Parmentier et al. (2018). The larger negative S_{H_2O} values (redder) represent stronger water emission features while the larger positive values (bluer) indicate more prominent water absorption features. The index is centered at zero for a blackbody-like featureless spectrum. In addition, we also scale the size of each point based on the host star temperature (T_{eff}) to reflect the effect of increased FUV/UV radiations from earlier type stars (Fu et al., 2022b; Lothringer and Barman, 2019).

We have only seen strong water absorption features among cooler hot Jupiter ($T_{day} < 2200\text{K}$) atmospheres (Kreidberg et al., 2014b; Line et al., 2016) driven by their decreasing TP profiles. This is due to heavy metal absorbers condensing out of the atmosphere at low temperatures. On the other hand, when the atmosphere becomes too hot ($T_{day} > 2700\text{K}$), water molecule dissociates and H⁻ continuum opacity starts to dominate. As a result, we have only observed featureless emission spectra among the hottest planets. In between the two regions ($\sim 2200\text{K}$ to 2700K) we see a transitional parameter space where atmospheres can be inverted (Evans et al., 2017; Fu et al., 2022b) or isothermal (Fu et al., 2021; Mansfield et al., 2021). HAT-P-41b sits in the middle of this transitional space. Its mostly featureless WFC3/G141 emission spectrum is similar to that of WASP-76b, WASP-74b, WASP-19b and KELT-7b. However, it is different from WASP-121b and KELT-20b where we saw evidence for water emissions. Although previous models have indicated multiple important physical transitions (Parmentier et al., 2018) happening at this temperature and gravity range, it is not yet well understood what exact physical processes drive the different thermal structures and emission spectra of these planets. In addition, host star type could be another important determining factor since strong FUV/UV radiations from the host star

can strengthen atmospheric thermal inversion (Fu et al., 2022b; Lothringer and Barman, 2019) as they deposit significant energy into the upper layers of the planetary atmospheres. This is supported by the large emission features seen in KELT-20b which orbits an A-type star. The lack of FUV/UV flux from F-type host star of HAT-P-41b could be another cause for its isothermal atmosphere.

4.7 Conclusion

We present the most complete emission spectrum for inflated hot Jupiter HAT-P-41b. The spectrum is close to blackbody-like with no significant molecular absorption or emission features. The best-fit *ATMO* model shows an isothermal TP profile agreeing with the dayside heat redistribution scenario and a metallicity value consistent with the solar value. The non-inverted TP profile is consistent with the non-detection of NUV/optical absorbers in the transit spectra. Significant H^- opacity suggested in Lewis et al. (2020) is not required in the model to adequately fit the emission spectrum. We also do not retrieve a metal-rich atmosphere as indicated in (Sheppard et al., 2021). However, the emission spectrum does not well constrain the atmosphere metallicity due to the limited wavelength coverage. The featureless emission spectrum of HAT-P-41b indicates planets with a dayside temperature around 2300K may have relatively isothermal TP profiles in the absence of heavy metal absorbers and strong host star FUV/UV radiations to drive thermal inversions. The comparison of HAT-P-41b to other similar hot Jupiters paints a murky picture of how atmospheric physical properties transition from cooler to hotter planets. The combined effect of surface gravity, thermal dissociation, H^- opacity, heavy metal absorbers, and host star type is yet to be disentangled. Future observations of more similar planets and follow-up JWST infrared

measurements of HAT-P-41b will be the key to solving the mystery of hot Jupiter atmospheres.

Table 4.3: HAT-P-41b eclipse spectrum

Wavelength midpoint (μm)	Bin width (μm)	Rp/Rs	Rp/Rs uncertainty (1 sigma)
1.1137	0.0186	186	108
1.1509	0.0186	378	94
1.1881	0.0186	171	86
1.2253	0.0186	526	102
1.2625	0.0186	427	87
1.2997	0.0186	346	86
1.3369	0.0186	435	91
1.3741	0.0186	587	89
1.4113	0.0186	419	91
1.4485	0.0186	499	95
1.4857	0.0186	383	94
1.5229	0.0186	446	99
1.5601	0.0186	505	117
1.5973	0.0186	643	105
1.6345	0.0186	733	102
3.6000	0.3800	1842	319
4.5000	0.5600	2303	177

Chapter 5: Strong H₂O and CO emission features in the spectrum of KELT-20b driven by stellar UV irradiation

5.1 Overview

Know thy star, know thy planetary atmosphere. Every exoplanet with atmospheric measurements orbits a star, and the stellar environment directly affects the planetary atmosphere. Here we present the emission spectrum of ultra-hot Jupiter KELT-20b which provides an observational link between host star properties and planet atmospheric thermal structure. It is currently the only planet with thermal emission measurements in the $T_{eq} \sim 2200\text{K}$ range that orbits around an early A-type star. By comparing it with other similar ultra-hot Jupiters around FGK stars, we can better understand how different host star types influence planetary atmospheres. The emission spectrum covers 0.6 to 4.5 μm with data from TESS, HST WFC3/G141, and Spitzer 4.5 μm channel. KELT-20b has a 1.4 μm water feature strength metric of $S_{H_2O} = -0.097 \pm 0.02$ and a blackbody brightness temperature difference of 528K between WFC3/G141 ($T_b = 2402 \pm 14\text{K}$) and Spitzer 4.5 μm channel ($T_b = 2930 \pm 59\text{K}$). These very large H₂O and CO emission features combined with the A-type host star make KELT-20b a unique planet among other similar hot Jupiters. The abundant FUV, NUV, and optical radiation from its host star ($T_{eff} = 8720 \pm 250\text{K}$) is expected to be the key that drives its strong thermal inversion and prominent emission features

based on previous PHOENIX models calculations.

5.2 Introduction

Hot Jupiters (HJs) with atmospheric thermal inversions are expected to have spectral emission features. Almost all hot Jupiter emission spectra observed to date have shown muted (Mikal-Evans et al., 2020) or non-existent $1.4 \mu m$ water emission features (Fu et al., 2021; Mansfield et al., 2021; Parmentier et al., 2018). Thermal dissociation of water and H- abundance (Arcangeli et al., 2018; Parmentier et al., 2018) are both expected to increase with temperature starting $\sim 2200K$ which will weaken the $1.4 \mu m$ water emission feature. Indeed, despite detection of thermal inversions, water emission features have not been seen for planets with dayside temperatures above $\sim 2800K$ (Arcangeli et al., 2018; Beatty et al., 2017; Haynes et al., 2015; Kreidberg et al., 2018a; Stevenson et al., 2014a). Host star spectral type has been predicted to be another determining factor of the HJ emission spectrum where increasing host star temperature strengthens planetary spectral emission features. This is due to absorption of the stronger FUV/UV flux from A-type stars by atomic metals and metal oxides (e.g., Fe I, Mg I, Ca I, TiO, VO, etc) which heats the upper planetary atmospheric layers (> 1 mbar) and drives stronger thermal inversions (Lothringer and Barman, 2019; Mansfield et al., 2021; Yan et al., 2020). Based on the combination of physical effects listed above, we expect planets orbiting A-type stars with low dayside temperatures to show the largest spectral emission features. The detection of large emission features on KELT-20b demonstrates that even planets with relatively low dayside temperatures can exhibit strong thermal inversions and emission features, driven by the abundant host star FUV/UV flux.

5.3 Observations and data reduction

The KELT-20b emission spectrum consists of observations from TESS, WFC3/G141, and Spitzer 4.5 μm channel. The TESS dataset includes 17 eclipses from observations in sectors 14, 40, and 41. The WFC3/G141 dataset was collected on 2021-09-20 as part of the GO 16307 (PI: Guangwei Fu) program. The Spitzer 4.5 μm channel eclipses come from archival data observed on 2019-02-21 as part of the GO 14059 (PI: Jacob Bean) program. All of the orbital parameters used for the TESS, WFC3, and Spitzer data reductions come from [Lund et al. \(2017\)](#).

5.3.1 HST Analysis

The WFC3/G141 eclipse dataset includes observations covering five consecutive HST orbits taken in spatial scan mode. Each frame was taken with the 512×512 pixel subarray in SPARS25 and NSAMP=5 setting. The forward scanning rate is $0.7 \text{ arcsec } s^{-1}$ and the exposure time is 69.6 seconds.

A spatially scanned 2D spectrum is first extracted from each frame and cleaned to remove any hot pixels and energetic particle events. It is then summed vertically to obtain the 1D spectrum. Next, we normalize each 1D spectrum by its median flux and use the `scipy.interpolate.interp1d` function to interpolate the 1D spectrum in the wavelength direction. The relative sub-pixel level horizontal shifts are then calculated based on the average of all spectra. Wavelength shifted corrected 1D spectra are then summed in the wavelength direction to form the white light eclipse lightcurve, which is fitted using `emcee` ([Foreman-Mackey et al., 2013](#)) with a combination of BATMAN ([Kreidberg, 2015](#)), the RECTE charge trapping systematics model ([Zhou et al., 2017](#)), HST orbital phase and a 2nd order polynomial of the wavelength shifts. Each wavelength channel

eclipse lightcurve is then fit with the same routine but with a fixed best-fit whitelight eclipse time at a 0.5 orbital phase.

5.3.2 TESS Analysis

We collected 4, 7, and 6 eclipse visits of KELT-20b from the TESS sector 14, 40, and 41 datasets correspondingly. Each eclipse visit was cut out of the TESS lightcurve including 4 hours before and after the mid-eclipse point. Then we fit the cut-out eclipse lightcurve with a combination of a linear slope and the `BATMAN` model. The slope is then subtracted out of each visit and the 17 eclipses are then stacked together for the final fit with `BATMAN` to obtain the eclipse depth of 139 ± 8 ppm. Our updated eclipse depth is consistent to within one sigma compared to [Wong et al. \(2021\)](#) which obtained an eclipse depth of 111_{-36}^{+35} ppm using only the sector 14 data.

5.3.3 Spitzer Analysis

We analyzed archival Spitzer/IRAC data for two secondary eclipses of KELT-20b, obtained by program 14059 (J. Bean, P.I.). These data are full phase curve observations, whereas we here concentrate only on the secondary eclipse. We accordingly restricted our analysis to data covering orbital phases in a limited range centered on each eclipse. Those ranges were further constrained by the span of the data in a single Spitzer observational sequence. We explored using slightly different phase limits and thereby verified that the derived eclipse depths are not sensitive to the temporal span of the out-of-eclipse baseline. The data comprise 64-frame subarray cubes (32x32 pixels in each frame), having exposure times of 0.4-seconds per frame. To extract photometry

from these data, we used 11 different circular apertures, centered on the star using a 2-D Gaussian fit procedure, and subtracting the (minimal) median background intensity in each frame via a histogram fitting procedure.

Our method of correcting for Spitzer’s intra-pixel sensitivity variations used pixel-level-decorrelation (PLD, [Deming et al., 2015](#)), as implemented by [Garhart et al. \(2020\)](#) (we used the same code). The PLD fitting procedure bins the data in time and uses 12 pixels as basis vectors (a 4x4 square, minus the corner pixels). Binning in time improves the precision of the pixel basis vectors, and it more effectively matches the red-noise character of the intra-pixel variations due to the IRAC instrument ([Deming et al., 2015](#)). We verified that the binning is not so extreme as to significantly alter the shape of the eclipse ([Kipping, 2010](#)), and we avoid overfitting by requiring that the number of data points after binning remains at least 10 times greater than the number of fitted parameters. The best bin size and photometric aperture radius are chosen by the code, based on minimizing the scatter in the Allan deviation relation ([Allan, 1966](#)), which expresses how the standard deviation of the residuals (data minus fit) varies as a function of bin size. That relation is ideally an inverse square root, and minimizing the Allan deviation scatter provides an initial fit that is optimal over a large range of time scales sampled by the data.

We use a quadratic baseline in time, fitting it simultaneously with the eclipse parameters and pixel coefficients. Because KELT-20b is quite hot, we expect that even the limited span of data we are using out of eclipse will show intensity variations due to the phase curve. Exploratory fitting indicated that the temporal baseline in these data is dominated by the phase curve of the planet, and not by a temporal ramp in instrumental sensitivity. Accordingly, we forced the baseline to be flat during the eclipse (the planet being hidden then), and we verified that a quadratic is an adequate approximation to a sinusoid over the limited range of phase that we

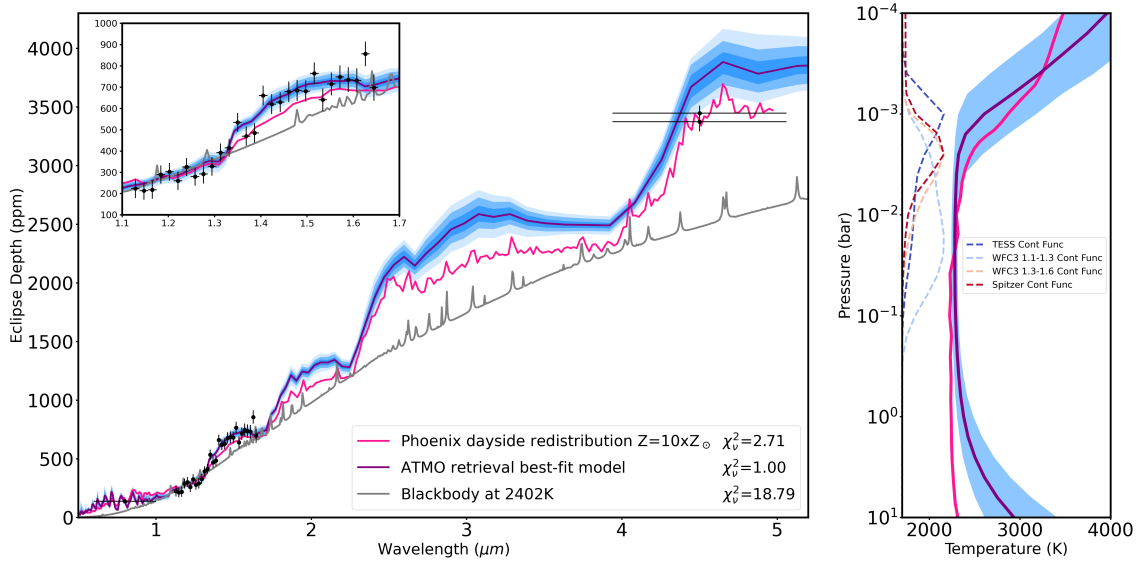


Figure 5.1 The emission spectrum of KELT-20b (black) is overplotted with the ATMO retrieval best-fit model (purple), PHOENIX forward model (pink), and blackbody model of 2402K (grey). The blue shaded regions represent 1 to 3 σ uncertainties from ATMO retrieval. The TP profiles are shown on the right with corresponding colors for ATMO and PHOENIX best-fit models. The blue shaded region represents 1 σ uncertainties. Contribution functions from ATMO for each wavelength channel are overplotted in dashed lines. The data probe pressure levels range from 100 to 1mbar with TESS being the lowest pressure and the blue side of WFC3/G141 (1.1-1.3 μm) being the highest. We detected prominent H₂O and CO emission features indicating a strongly inverted TP profile as shown by both models. The excellent agreement of the TP profiles between ATMO and PHOENIX shows the dayside atmosphere is or very close to radiative equilibrium.

analyze.

Our code is formally Bayesian, but our priors (e.g., for eclipse depth and central phase) are uniform, and we freeze the orbital parameters such as inclination and a/R_s during the fit, as explained in Sec. 3.3 of [Garhart et al. \(2020\)](#). Under these conditions, the fitting process is equivalent to a χ -squared minimization, but the process produces posterior distributions for the fitted parameters using a classic Markov Chain Monte Carlo (MCMC) chain with Gibbs sampling. Our MCMC chains each comprise 800,000 samples, after a 10,000 sample burn-in. Convergence is excellent, as verified by comparing the posterior distributions and Gelman-Rubin parameter for four independent chains at each eclipse. Our adopted eclipse depths and error bars are based on a Gaussian fit to the posterior distributions. The depths that we derive for the two independent eclipses are 3448 ± 64 and 3375 ± 82 ppm, in excellent mutual agreement.

5.4 ATMO retrieval and PHOENIX model

The full emission spectrum (Table 5.1) of KELT-20b from 0.6 to 4.5 μm is presented in Figure 5.1. To interpret the spectrum, we performed ATMO retrieval ([Amundsen et al., 2014](#); [Drummond et al., 2016](#); [Goyal et al., 2018](#); [Tremblin et al., 2016, 2015](#)) analysis and PHOENIX self-consistent forward model ([Lothringer et al., 2018](#)) comparison. Having both retrieval and self-consistent atmospheric models allows us to cross-check the results to ensure more physically robust and consistent interpretations. The priors used for the ATMO retrieval are the following: $\log(Z/Z)=-2$ to 2; $\log g=2.5$ to 3.46; $\log(K_{IR})=-5$ to -0.5; $\log(\gamma/IR)=-4$ to 2; $\beta=0$ to 1.5; $\log(C/C)=-2$ to 2; $\log(O/O)=-2$ to 2. The best-fit retrieved spectrum (Figure 5.1) with a χ^2_ν of 1.00 shows very prominent H₂O and CO emission features at 1.4 and 4.5 μm , respectively.

The retrieved TP profile is highly inverted starting around 1mbar with a rapid increase of $\sim 1000\text{K}$ from ~ 7 to 0.3 mbar. The contribution functions of different wavelength channels of the emission spectrum show that the TESS band is probing the highest layers (lowest pressures) while the blue side (1.1-1.3 μm) of the WFC/G141 band is probing the deepest parts (highest pressures) of the atmosphere. The red side (1.3-1.6 μm) of the WFC/G141 band and Spitzer 4.5 μm have similar flux contributions from the 10 to 1mbar region where H_2O and CO have a relatively higher abundance (VMR $\sim 8 \times 10^{-3}$). The retrieved metallicity, carbon, and oxygen (Figure 5.3) abundances are ~ 3.9 , 10 and 17 times higher than the solar values, but the retrieved C/O ratio of $0.454^{+0.211}_{-0.205}$ is consistent with the solar value to within one sigma.

We also ran a set of self-consistent PHOENIX forward models assuming dayside heat redistribution, Local Thermodynamic Equilibrium (LTE), and solar C/O ratio with 0.1, 1, and 10 times solar metallicity. The best-fit model is 10 times metallicity with a χ^2_ν of 2.71 showing similar strong H_2O and CO emission features compared to the retrieved ATMO best-fit spectrum. We consider this to be a very good forward model fit to the data considering there is only one parameter that was varied being the overall metallicity. The TP profile from PHOENIX is also in excellent agreement to within one sigma of retrieved ATMO TP profile among the pressure levels the data are probing. The matching TP profiles between retrieval and forward model indicate the atmosphere of KELT-20b around $\sim 10 - 1$ mbar range is close to LTE.

5.5 Discussion

The measured blackbody brightness temperatures are based on a PHOENIX stellar model (Husser et al., 2013) grid ($\log g=4.5$ and $\log Z=0$) interpolated to $T_{eff} = 8720\text{K}$ are $2402 \pm 14\text{K}$

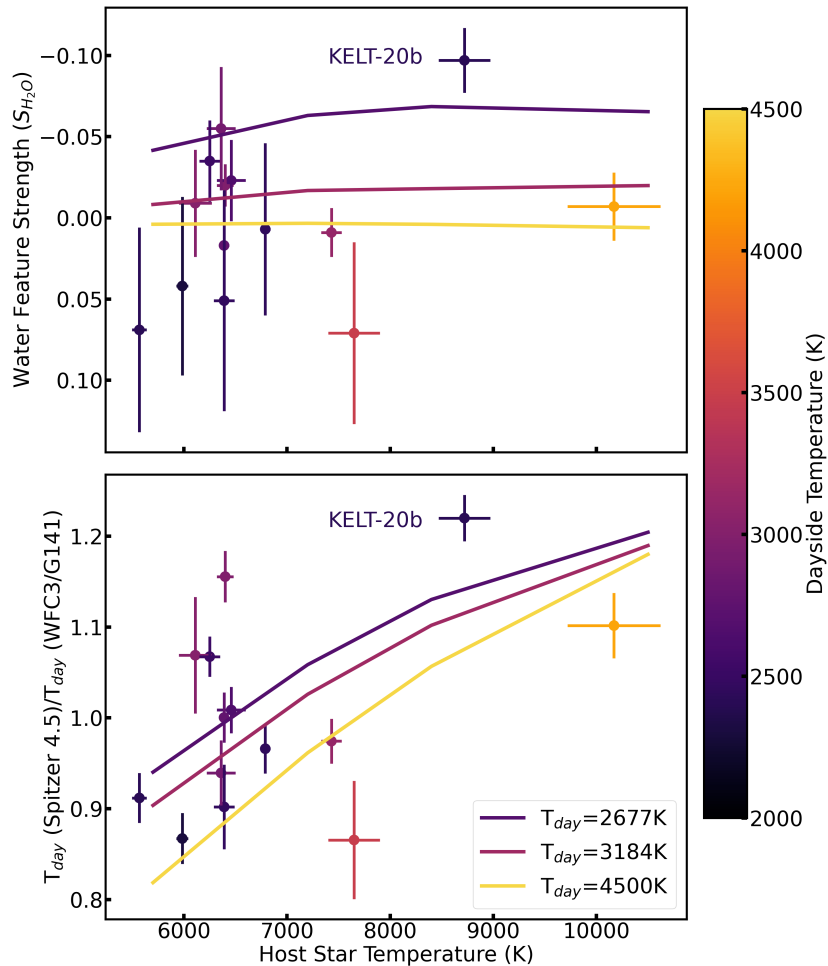


Figure 5.2 KELT-20b emission spectrum metrics compared with other hot Jupiters with day side temperature higher than 2200K overplotted with PHOENIX models assuming solar metallicity and C/O ratio. The top panel shows the water feature strength metric S_{H_2O} from [Mansfield et al. \(2021\)](#) and KELT-20b is located in a unique parameter space of high host star temperature combined with low dayside temperature. The large water emission feature from KELT-20b is consistent with the PHOENIX model predictions. The bottom panel shows the Spitzer 4.5 μm blackbody brightness temperature relative to the WFC3/G141 out of water band blackbody brightness temperature. The large difference between the two bands in KELT-20b indicates a prominent CO emission feature.

for the HST/WFC3 G141 band and $2930 \pm 59\text{K}$ for the Spitzer $4.5 \mu\text{m}$ band. The prominent H_2O and CO emission features of KELT-20b make it unique compared to other UHJs within a similar equilibrium temperature range (Figure 5.2) such as WASP-76b (Fu et al., 2021), WASP-121b (Evans et al., 2017) and HAT-P-7b (Mansfield et al., 2018).

5.5.1 $S_{\text{H}_2\text{O}}$ water feature strength

KELT-20b has a $1.4 \mu\text{m}$ water feature strength metric of $S_{\text{H}_2\text{O}} = -0.097 \pm 0.02$ as defined in Mansfield et al. (2021) which compares the $1.35 - 1.48 \mu\text{m}$ “in-band” part of the emission spectrum to the blackbody model fit based on the two “out-of-band” regions ($1.22 - 1.33$ and $1.52 - 1.61 \mu\text{m}$) of the spectrum. A positive value would suggest a water absorption feature and a negative value would indicate a water emission feature. In comparison with other hot Jupiters that have measured dayside temperatures exceeding 2200K , KELT-20b has a very large water emission feature (Figure 5.2 top panel). It is a unique planet with a relatively cool dayside within ultra-hot Jupiters but high host star temperature. High FUV/UV flux from the star drives a strong thermal inversion, while the relatively low dayside temperature suppresses the thermal dissociation of water and the H- continuum opacity source. To understand the combined atmospheric effects from the planet and host star temperatures, we generated a grid of self-consistent PHOENIX models assuming solar metallicity and C/O ratio. For cooler planets, we see increased water emission feature amplitudes around hotter stars, but as planet temperature increases the water feature diminishes due to thermal dissociation and the raising of H- opacity.

This combined effect of the planet and host star temperature on water emission feature strength has also been demonstrated with a different independent set of atmospheric models as

shown in panel c of Figure 4 in [Mansfield et al. \(2021\)](#). As host star temperature increases, the water emission feature is also expected to increase the most for hot Jupiters with day side temperature between ~ 2200 and 2500K and then taper as planets become even hotter.

5.5.2 WFC3/G141 to Spitzer $4.5 \mu\text{m}$ brightness temperature difference

KELT-20b also has a large measured blackbody brightness temperature difference between “out-of-band” WFC3/G141 ($T_b=2402\pm 14\text{K}$) and the Spitzer $4.5 \mu\text{m}$ ($T_b=2930\pm 59\text{K}$) band which indicates a strong CO emission feature around $4.5 \mu\text{m}$. The high relative blackbody brightness temperature ratio between the two bands ($Tb_{G141}/Tb_{4.5}$) from KELT-20b stands out compared to other hot Jupiters ([Baxter et al., 2021](#); [Garhart et al., 2020](#)) (Figure 5.2 bottom panel). In the absence of H- opacity, WFC3/G141 probes the H_2O and continuum while Spitzer $4.5 \mu\text{m}$ band measures the CO spectral feature. These two bands can probe different pressure levels depending on the TP profile. In an inverted TP profile, Spitzer $4.5 \mu\text{m}$ band usually probes higher in the atmosphere as CO can exist at low-pressure levels with the high thermal dissociation temperature. However, as H- continuum opacity abundance raises with planet temperature, the photosphere pressure levels probed by these two bands converge. This is shown in the same PHOENIX model grid as described in the section above, as at a given host star temperature, increasing planet temperature decreases $Tb_{G141}/Tb_{4.5}$ as they both start to probe H- in the upper atmosphere. On the other hand, as the host star temperature increases, a higher amount of FUV/UV radiation gets absorbed in the upper atmosphere and drives a stronger thermal inversion which enhances the CO emission feature. At the same time, less flux can reach deeper in the atmosphere which leads to a lower continuum temperature probed in the WFC3/G141 band. The $Tb_{G141}/Tb_{4.5}$

value decreases as planet temperature increases due to higher H- opacity raising the photosphere in the WFC3/G141 band and reducing the temperature difference measured between the two bands. Therefore we expect to see large $Tb_{G141}/Tb_{4.5}$ values among cooler planets with hotter host stars as shown in KELT-20b. This is consistent with the observational implications predicted by [Lothringer and Barman \(2019\)](#) (see their Figure 8) which suggested a larger relative emission flux difference between these WFC3/G141 and Spitzer 4.5 μm bands as host star temperature increases. Since the PHOENIX model grid assumes solar metallicity and C/O ratio values, the data-model deviations also demonstrate the atmospheric composition diversity within the hot Jupiter population.

5.5.3 High-resolution spectroscopy

KELT-20b has been observed during transit from the ground with multiple high-resolution spectroscopy facilities including HARPS-N, CARMENES, and EXPRES. Absorption features from neutral and ionized heavy metals including FeI, FeII, CaII, NaI, MgI, and Cr II have been detected with high confidence and confirmed from different independent studies ([Casasayas-Barris et al., 2019](#); [Hoeijmakers et al., 2020](#); [Nugroho et al., 2020](#); [Stangret et al., 2020](#)). The numerous detections of heavy metal species in the upper atmosphere layers through high-resolution transmission spectroscopy are consistent with a strongly inverted TP profile. These metal atoms are likely responsible for the thermal inversion by absorbing the abundant FUV, NUV, and optical flux from the star and then heating up the upper layers. The strong emission features of KELT-20b and the bright host star make it an ideal target for follow-up dayside high-resolution spectroscopy which can access the CO and H₂O features beyond 2 μm to further constrain the metallicity, C/O

Table 5.1 KELT-20b eclipse spectrum

Wavelength midpoint (μm)	Bin width (μm)	Eclipse Depth (ppm)	Uncertainty 1-sigma (ppm)
0.800	0.2000	139	8
1.130	0.0092	224	45
1.150	0.0092	214	42
1.170	0.0092	218	43
1.180	0.0092	289	43
1.200	0.0092	302	42
1.220	0.0092	261	44
1.240	0.0092	325	43
1.260	0.0092	280	42
1.280	0.0092	292	45
1.290	0.0092	328	44
1.310	0.0092	393	43
1.330	0.0092	415	42
1.350	0.0092	535	44
1.370	0.0092	470	45
1.390	0.0092	485	46
1.410	0.0092	660	47
1.420	0.0092	621	47
1.440	0.0092	630	46
1.460	0.0092	679	48
1.480	0.0092	685	50
1.500	0.0092	682	50
1.520	0.0092	765	51
1.530	0.0092	641	53
1.550	0.0092	715	54
1.570	0.0092	748	54
1.590	0.0092	735	58
1.610	0.0092	732	57
1.630	0.0092	857	58
1.640	0.0092	698	62
4.500	0.5600	3448	64
4.500	0.5600	3375	82

ratio, and TP profile (Line et al., 2021).

5.6 Conclusion

We present the emission spectrum of the ultra-hot Jupiter KELT-20b from 0.6 to 4.5 μm showing strong H₂O and CO emission features. The H₂O feature strength is calculated through the $S_{\text{H}_2\text{O}}$ index and the CO feature is inferred by the differential brightness temperature measured between the WFC3/G141 and Spitzer 4.5 μm channel bands. KELT-20b stands out among all other similar hot Jupiters with strong emission features while other UHJs have mostly shown featureless blackbody-like emission spectra. Our results imply that the unique early A-type host star of KELT-20b is the key difference that drives its stronger thermal inversion compared to other UHJs as predicted by Lothringer and Barman (2019). KELT-20b provides direct observational evidence linking host star properties to planetary thermal structure, which adds host star property as the new parameter space to explore for our understanding of exoplanet atmospheres.

KELT-20b is the coolest planet among the only few UHJs (WASP-33b, Kepler-13Ab, and KELT-9b) that have been characterized around early A-type stars. The large differences in equilibrium temperatures within this very small sample size make it infeasible for a statistically significant comparison study. This calls for more follow-up atmospheric characterization of hot Jupiters that orbit A stars. HST will still be valuable in probing the water feature in the near-infrared for targets with favorable signal to noise. However, with Spitzer decommissioned, JWST will be the ideal telescope to access the H₂O and CO emission features in the infrared.

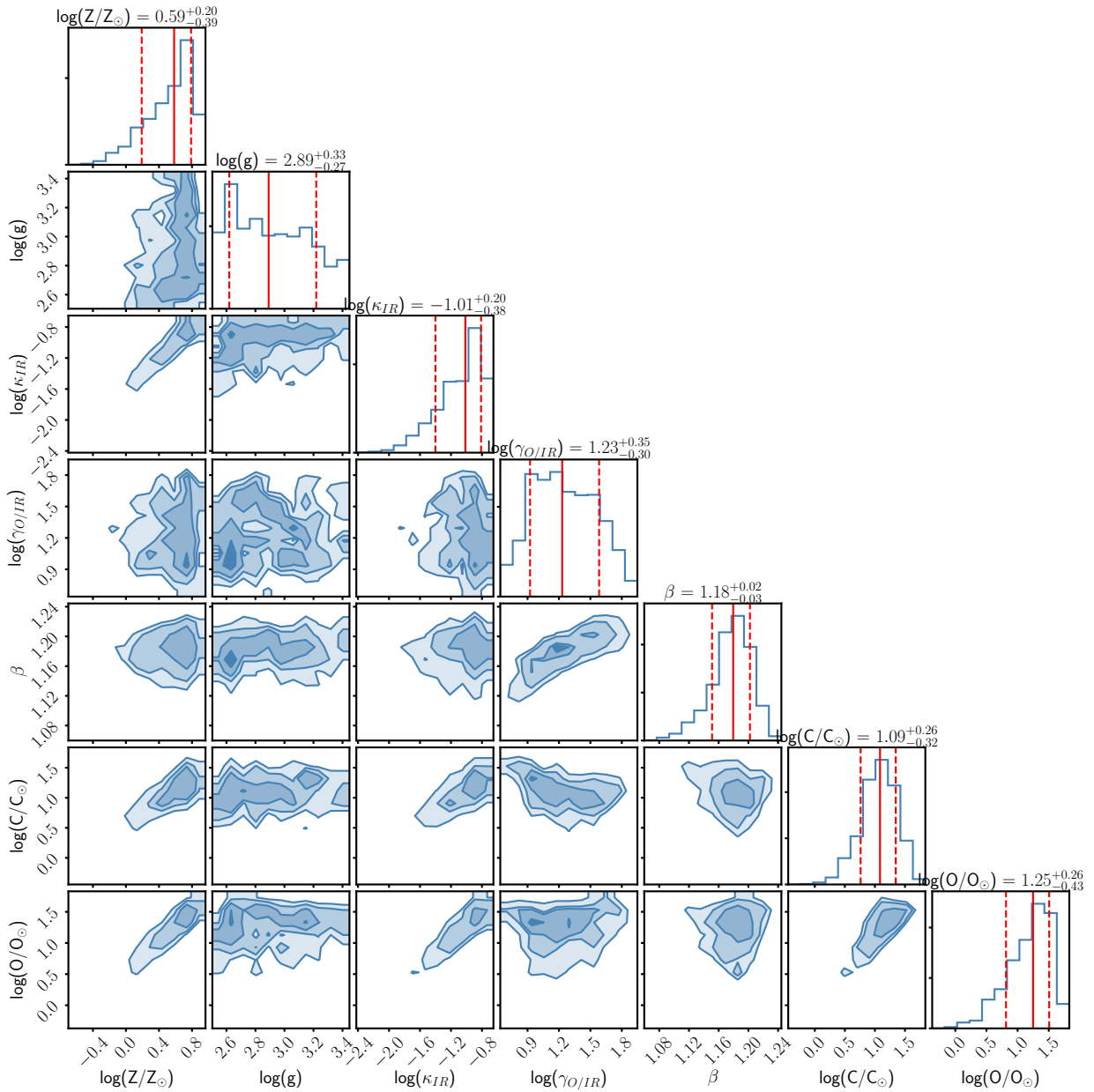


Figure 5.3 Posterior distribution of ATMO retrieval. The retrieved metallicity, carbon, and oxygen abundances are ~ 3.9 , 10, and 17 times higher than the solar values, but the retrieved C/O ratio of $0.454^{+0.211}_{-0.205}$ is consistent with the solar value to within one sigma. The $\log(g)$ is not well constrained as the emission spectrum is not sensitive to surface gravity.

Chapter 6: Statistical Analysis of Hubble/WFC3 Transit Spectroscopy of Extrasolar Planets

6.1 Overview

Transmission spectroscopy provides a window to study exoplanetary atmospheres, but that window is fogged by clouds and hazes. Clouds and haze introduce a degeneracy between the strength of gaseous absorption features and planetary physical parameters such as abundances. One way to break that degeneracy is via statistical studies. We collect all published HST/WFC3 transit spectra for 1.1-1.65 μm water vapor absorption, and perform a statistical study on potential correlations between the water absorption feature and planetary parameters. We fit the observed spectra with a template calculated for each planet using the Exo-Transmit code. We express the magnitude of the water absorption in scale heights, thereby removing the known dependence on temperature, surface gravity, and mean molecular weight. We find that the absorption in scale heights has a positive baseline correlation with planetary equilibrium temperature; our hypothesis is that decreasing cloud condensation with increasing temperature is responsible for this baseline slope. However, the observed sample is also intrinsically degenerate in the sense that equilibrium temperature correlates with planetary mass. We compile the distribution of absorption in scale heights, and we find that this distribution is closer to log-normal than Gaussian. However, we

also find that the distribution of equilibrium temperatures for the observed planets is similarly log-normal. This indicates that the absorption values are affected by observational bias, whereby observers have not yet targeted a sufficient sample of the hottest planets.

6.2 Introduction

Robust observations of exoplanetary atmospheres using transmission and emission spectroscopy with the Wide Field Camera-3 (WFC3) on the HST have led to significant progress in understanding exoplanetary atmospheres. Recent intriguing results have inferred atmospheric thermal structure and circulation patterns (Stevenson et al., 2014a), temperature inversions (Evans et al., 2017; Haynes et al., 2015), clouds/hazes (Sing et al., 2016), and water abundance (Kreidberg et al., 2014b; Wakeford et al., 2017). Focusing on HST/WFC3 transmission spectrum measurements, the amplitude of water vapor absorption (1.1 to 1.7 μm) has been the most commonly used observational quantity due to its relatively high abundance and strong absorption strength. One key scientific motivation is to derive the abundance of oxygen (as a proxy for planetary metallicity) as a function of planetary mass (Kreidberg et al., 2014b). The planetary mass-metallicity relation could yield insights into the planet formation process (Thorngren and Fortney, 2019).

However, accurately measuring water abundance through transmission spectroscopy has been argued to be very challenging if only WFC3 spectra are considered (Griffith, 2014; Heng and Kitzmann, 2017). For example, the presence of patchy clouds/hazes can mimic the same effect as either high molecular weight (Line et al., 2016) or low molecular abundances (?) and also introduce a degeneracy between reference pressure and water abundance in the planetary atmosphere. To optimize and prepare for future transmission spectroscopy observations using

the JWST, it is important to better understand the effects of clouds and hazes, and develop techniques to precisely measure water abundance in exoplanetary atmospheres. One approach is to perform very in-depth studies of individual planets (Fu et al., 2021, 2022a,b). Utilizing additional observational constraints from optical to infrared (0.5 - 5 μm), combined with detailed modeling of T-P profiles, properties of cloud-forming condensate species can be deduced (Line et al., 2016; MacDonald and Madhusudhan, 2017; Stevenson et al., 2017; Wakeford et al., 2017). Once a large sample of planets have been analyzed extensively, patterns and correlations between water abundance and cloud properties may emerge (Sing et al., 2016).

Another approach is to short-circuit the tedious process of multiple in-depth investigations, by seeking correlations between the observed magnitude of water absorption and bulk properties of the exoplanets such as equilibrium temperature, planetary mass and gravity. This approach can also help to formulate hypotheses and reveal potentially related physical parameters that can be tested by subsequent analyses and observations.

Recently, Tsiaras et al. (2018) announced a catalog of hot-Jupiter absorption spectra observed in multiple programs using HST/WFC3 in spatial scanning mode. In this Letter we use these spectra with 4 additional spectra (Huitson et al., 2013; Knutson et al., 2014; Kreidberg et al., 2014a; Mandell et al., 2013) in a statistical analysis of transit water absorption in relation to planetary bulk parameters for a sample of 34 hot-Jupiter (to hot-Neptune) exoplanets. Our analysis uses public data and models, and simple techniques that anyone can reproduce. For reasons that we explain below, our fundamental observational quantity is the number of atmospheric scale heights that are opaque in the water band during transit (Stevenson, 2016). Sec. 2 describes how we determine that quantity based on the spectra from Tsiaras et al. (2018), and Sec. 3 describes the correlation of the inferred absorption with other planetary properties. Sec. 4 summarizes

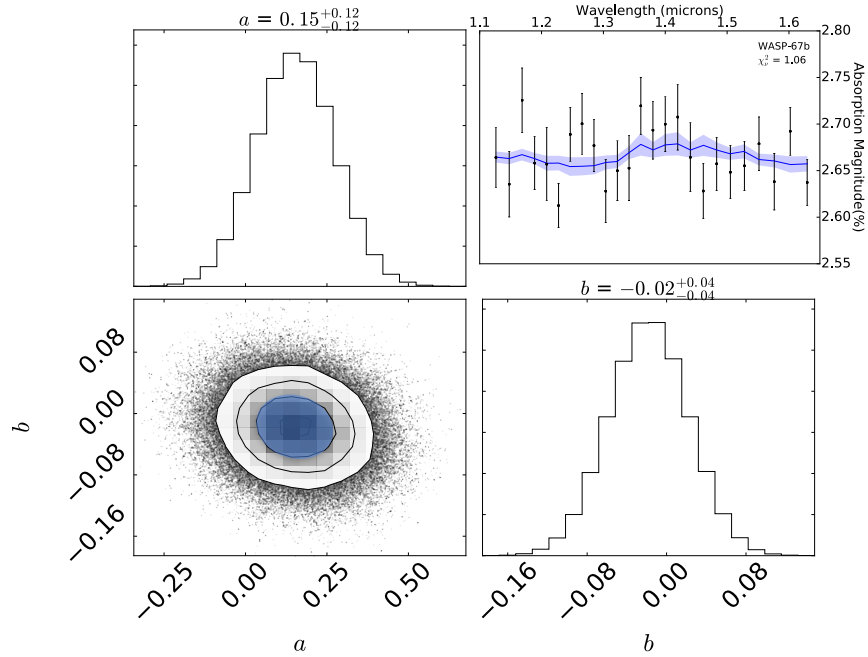


Figure 6.1 Example of our MCMC fitting of an Exo-transmit template spectrum to the data for WASP-67b. This planet has the median χ_ν^2 in the sample, with $\chi_\nu^2 = 1.05$. The a coefficient is the amplitude scale factor for fitting the Exo-transmit template spectrum, and b is the wavelength coefficient of a baseline slope. The $\leq 1\sigma$ contours are shaded in blue for the posterior distribution samples (lower left) and for the fit to the data (upper right).

our conclusions and discusses implications for future measurements.

6.3 Data Analysis

A planet with base radius R_p has a transit depth of R_p^2/R_s^2 (R_s is star's radius). If the planet's atmosphere is opaque over one scale height, the transit depth will increase by $2R_p H/R_s^2$, where the pressure scale height is $H = kT/\mu g$ with k being the Boltzmann constant, T being the planet's equilibrium temperature, μ being the mean molecular weight and g being the surface gravity. Surface gravity and temperature can be directly estimated from measurable quantities including planetary mass and radius, orbital semi-major axis, and stellar temperature and radius (with assumptions on the planetary albedo and longitudinal circulation). We want to determine

how the magnitude of atmospheric absorption varies with physical quantities that are not directly associated with the pressure scale height, such as the existence and height of clouds and hazes. Therefore, following [Stevenson \(2016\)](#), we remove the dependence on known parameters by dividing the magnitude of atmospheric absorption by $2R_p H/R_s^2$. To calculate H and enable a consistent comparison with [Stevenson \(2016\)](#), we used a mean molecular weight of 3.8 for planets with $R < 0.5R_J$ and 2.3 for all other planets, following [Stevenson \(2016\)](#). We then seek the statistical properties of the absorption, measured in scale heights. Our study improves upon [Stevenson \(2016\)](#) in several ways. First, we increase the sample size from 14 to 34. Also, we utilize a model atmosphere template to measure the absorption (Stevenson used absorption indices based upon restricted ranges in wavelength), and we allow for a baseline slope in the spectrum such as might be produced by small-particle scattering. We also investigate the nature of the distribution function for exoplanetary absorption measured in scale heights.

We use observed spectra from [Tsiaras et al. \(2018\)](#), and derive the magnitude of the water absorption from the data as directly as possible. Essentially, we find the minimum and maximum values of the data, and convert the difference between them to scale heights of absorption. But we must allow for the shape of the water band (absorption varies with wavelength), the scatter in the data points, and the possibility of instrumental or astrophysical baseline slopes (e.g., by small-particle scattering). We accomplish that by calculating a nominal model spectrum for each planet, and use it as a template to gauge the amplitude of the absorption. We calculate the equilibrium temperature of each planet, assuming zero albedo and uniform re-distribution of heat, and the surface gravity from published planetary masses and radii. The nominal model spectrum follows from those parameters using the Exo-Transmit code ([Kempton et al., 2017](#)). We used isothermal T/P profiles, with collision-induced continuous opacities as per Table 1 of

Kempton et al. (2017), and line opacity for water only. We then scale the nominal spectrum ($x(\lambda)$) to greater or less absorption using a multiplicative factor (a), and fit it to the observed spectrum ($y(\lambda)$) using an MCMC procedure (*emcee*, (Foreman-Mackey et al., 2013) with the equation $y(\lambda) = ax(\lambda) + b\lambda + c$ where a is the scaling factor, b is the wavelength coefficient for the baseline slope, and c is a constant.

For each planet we then take the difference between the maximum and minimum value of R_p^2/R_s^2 in the fitted model spectrum after removing the slope, and we divide by $2R_pH/R_s^2$, to convert the magnitude of the absorption to scale heights, A_H . These absorption values are listed in Table 6.1. Although we only use the 1.3 - 1.65 μm part of the spectrum for our statistical study (region of strongest absorption), we also tabulate the results from the full 1.1 - 1.65 μm range in Table 6.1. We verified that our results do not change significantly if we fit to the full 1.1 - 1.65 μm range.

Figure 6.1 shows the fit to WASP-67b, that has the median χ_ν^2 in our sample. The posterior distributions for the a and b coefficients (and thus for A_H) are very close to Gaussian, reflecting the high quality of the HST data. We derive the errors on A_H from those posterior distributions.

The 30 spectra presented in Tsiaras et al. (2018) were derived using a uniform and consistent data analysis method (Tsiaras et al., 2018). However, it is still advantageous to compare them with independent spectra derived by other groups (Table 6.1, right columns). When we fit to the other spectra the same way, we derive statistically consistent absorptions in scale heights. Although a few planets (HAT-P-1b, HD 189733b, HD 209458b) show some difference, we do not detect a systematic deviation. The slope (1.14 ± 0.09) of an orthogonal distance fit (Akritas and Bershady, 1996) is within 2σ of unity, indicating that spectra from Tsiaras et al. (2018) are consistent with those derived by other groups. We conclude that we are working with a valid

collection of spectra in the sense that there are no internal inconsistencies in the measurements.

6.4 Statistical Correlations

Armed with A_H values from table 6.1, we investigated their relationship with planetary temperature, mass, radius, and surface gravity. These relationships are subtle, and the statistics are fragile. However, we interpret them boldly, so as to form hypotheses that can stimulate and guide future work.

The first point to note is that the median A_H value is only 1.4, less than expected for clear solar abundance atmospheres ($A_H \approx 5$). That can be due to either clouds (Barstow et al., 2016) or low abundance of water vapor (?). As for correlations, in the top panel of Figure 6.2, we show the relation between A_H and planetary equilibrium temperature. We propagate errors in the stellar and orbital parameters to yield errors in the abscissa as well as the ordinate. An orthogonal distance regression yields a slope of 0.0008 ± 0.00016 , and the Spearman correlation coefficient is 0.43, indicating a moderate correlation. We emphasize that the temperature dependence of the atmospheric scale height has already been removed from the ordinate, so this correlation is a physical effect beyond the atmospheric scale height. We hypothesize that the dominant effect is the decreasing amount of cloud condensation as the planetary equilibrium temperature increases. To the extent that hotter planets have fewer cloud-forming condensate species present in their atmospheres than cooler planets (Barstow et al., 2016; Kataria et al., 2016), that will tend to produce a positive slope between temperature and A_H .

We explored using a mass-metallicity power law, emulating Figure 4 of (Kreidberg et al.,

2014b), to calculate atmospheric molecular weight. That has little effect on most planets in our sample because they are hot Jupiters with predominantly H-He atmospheres. The power law causes two planets to scatter to greater A_H values at the left edge of Figure 2, degrading the correlation, but not affecting the baseline derived on the lower panel of Figure 2.

A similar temperature versus A_H correlation was reported by Crossfield and Kreidberg (2017) with a sample size comprised of six Neptune-size planets. The correlation led them to suggest that hazes might become more significant for planets with $T_{eq} < 850K$. Our study includes their six planets and also an additional six planets with $T_{eq} < 1000K$. We do not see a clear divide of A_H values around $T_{eq} = 850K$ as shown by Crossfield and Kreidberg (2017). However, our six additional planets are not Neptune-like but rather more massive (~ 0.2 to $\sim 0.5 M_J$) planets. Another in-depth study conducted by Sing et al. (2016) used eight planets with extensive wavelength coverage from HST/Spitzer transmission spectra. Although those eight planets have T_{eq} ranging from $\sim 1000K$ to $\sim 2500K$, Sing et al. (2016) found no trend between T_{eq} and the magnitude of water absorption. In the upper panel of 6.2, we shaded the eight planets from (Sing et al., 2016) with blue circles. Those eight planets are not sufficient to establish a clear correlation (p-value of 0.3 for a linear trend).

Another effect that may be present on Figure 6.2 is a "baseline" value for A_H at each equilibrium temperature, with scatter above that baseline value, especially for equilibrium temperatures below 1500K. To better characterize this baseline effect, we developed a binning analysis method that divides the data according to a chosen bin size and takes the lowest point in each bin. This way, upward scattering points will be filtered out and only the points that form the baseline will remain. However, the resulting baseline correlation from this method will depend on the chosen bin size. To support the validity of this binning method and find the optimal bin size, we tested

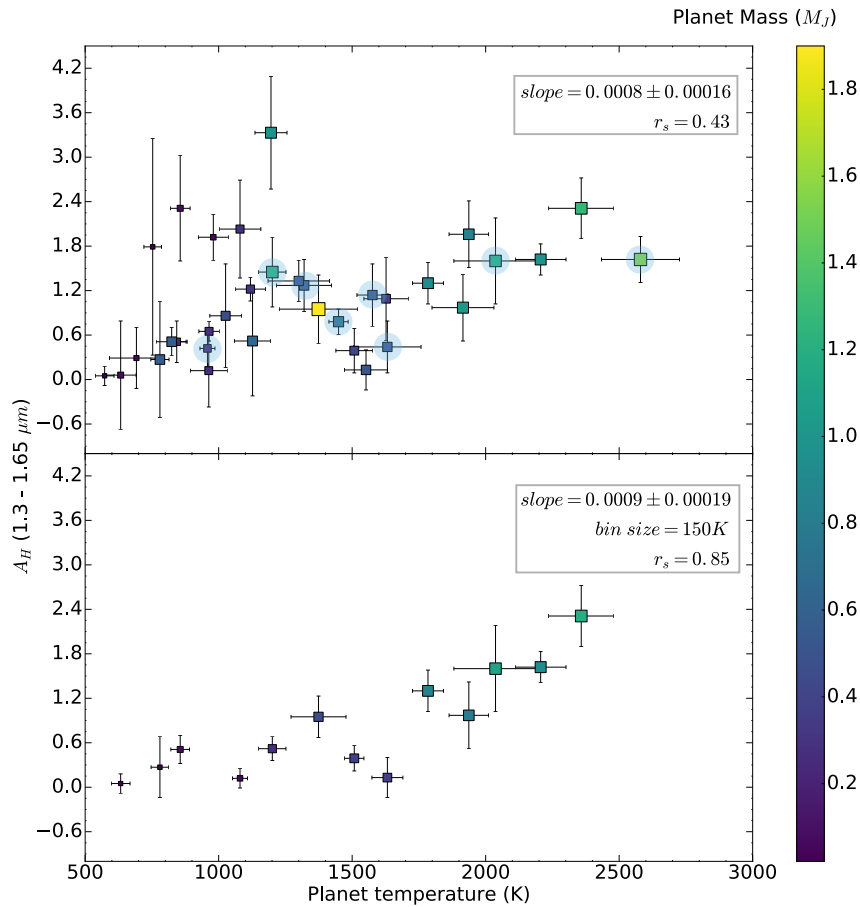


Figure 6.2 The upper panel is the 1.3 - 1.6 μm absorption in scale heights versus planet equilibrium temperature. We infer a positive baseline slope correlation (p-value = 0.01) with upward scattering on the left side. After applying the binning method discussed in section 3, we obtain a statistically significant ($r_s = 0.85$) baseline correlation as shown in the lower panel. Mass uncertainty is proportional to squares size. The eight planets shaded in blue circles in the upper panel are the ones investigated in (Sing et al., 2016)

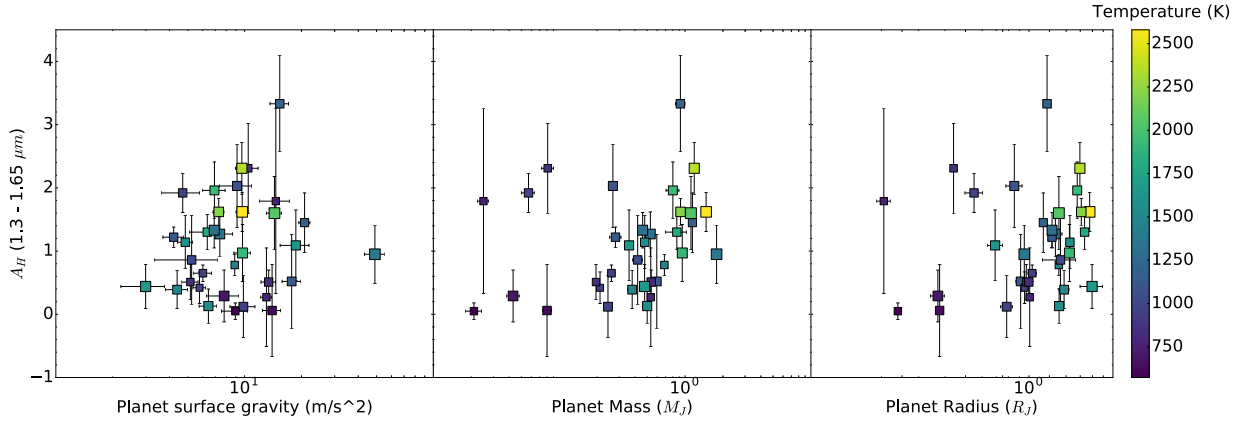


Figure 6.3 Planet surface gravity, mass, and radius versus absorption in scale heights (1.3-1.65 μm). We do not detect any significant statistical correlation; the suggestion of a correlation with mass is due to an intrinsic degeneracy in the sample, combined with the temperature correlation shown in Figure 2.

it on randomly generated absorption values. We averaged the results from 1000 runs of random values and compared with real absorption data. This test indicated that false baseline correlations can result from binning random data, but those correlations are much weaker than we find when we bin the real data. Using a 150K bin size on the real data, we obtained a baseline slope with very strong positive correlation ($R_s=0.85$) as shown in lower plot in Figure 6.2. Binning random data with this bin size produces only $R_s=0.35$, a weak effect. Using orthogonal distance regression on the binned real data, we find a slope of $0.0009 K^{-1}$. Thus, for each 1000K increase in planetary equilibrium temperature, we find that the baseline (i.e., statistical minimum) water vapor absorption increases by about 0.9 scale heights.

The top panel of Figure 6.2 shows that the cooler planets tend to scatter above our inferred baseline. This could be due to variable cloud coverage, variable water vapor abundance, or variations in surface gravity that cause different cloud distributions at a given equilibrium temperature. Surface gravity is the most amenable to investigation, and we now turn to that possible correlation.

Figure 6.3 plots A_H versus surface gravity, planet mass and radius. We do not see any

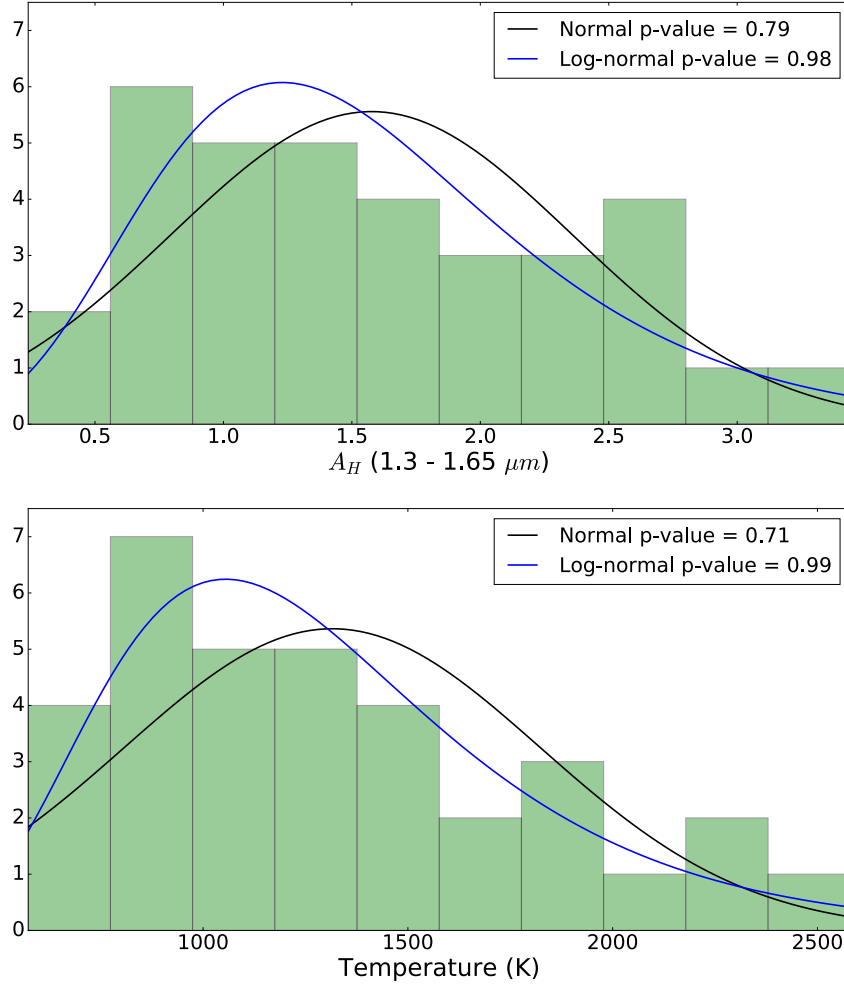


Figure 6.4 Upper plot shows the distribution of absorption in scale heights ($1.3 - 1.65 \mu\text{m}$) is more likely to be log-normal than normal. This is caused by the target selection bias as there are more cooler planets than hotter ones in the sample (shown in the lower panel).

clear statistical correlation between surface gravity, or radius, and A_H . There is an apparent correlation with mass, but it is due to the temperature correlation (Figure 2), combined with an intrinsic degeneracy in the sample, as discussed below. The fact that increasing surface gravity does not seem to have a significant effect on A_H reinforces the expectation that surface gravity is not directly linked to the cloud formation process. In simple models of cloud formation (Burrows and Sharp, 1999), it is largely a chemical process determined by the equilibrium temperature and thermal structure of the planet. Our statistical results are consistent with that paradigm.

We also investigated the distribution function of A_H values. We noticed that the most likely distribution of A_H is not Gaussian but rather log-normal as shown in the upper panel in Figure 6.4. In principle, this could reflect the complexity of transit absorption, since log-normal distributions usually result when the underlying processes are multiplicative as opposed to additive. However, we think this is likely due to a target selection bias instead of fundamental physical processes, since the distribution of equilibrium temperatures (lower panel in Figure 6.4) similarly favors a log-normal distribution. Evidently, observers have been favoring cool planets as opposed to hot ones. We suggest that more hot planets should be included in future observations to ensure unbiased samples (i.e., more closely approaching a uniform distribution).

6.5 Summary and Conclusions

We have expanded the sample studied by [Stevenson \(2016\)](#) from 14 to 34 planets ranging from super-Earths to hot Jupiters. We used Exo-Transmit templates to fit the observed spectra, and express the water absorption in units of scale heights (A_H), removing known physical dependencies. Comparing with results from [Stevenson \(2016\)](#), we find one continuous positive correlation between A_H and T_{eq} ranging from $\sim 500\text{K}$ to $\sim 2500\text{K}$ as opposed to a strong correlation only when $T_{eq} < 750\text{K}$. [Stevenson \(2016\)](#) also reported a weak correlation between surface gravity and A_H , but we see no clear correlation between those two parameters. Our results are qualitatively consistent with the temperature correlation inferred by [Crossfield and Kreidberg \(2017\)](#) for Neptune-like planets.

We point out that the observed sample of exoplanets (Table 6.1) contains an intrinsic

degeneracy in the sense that planetary mass is correlated with equilibrium temperature (correlation coefficient = 0.75, a strong correlation). Moreover, our division by the scale height is equivalent to multiplying by mass. In principle, it is possible for the temperature correlation to be created as an artifact of our analysis method. However, that would require that the total observed water absorption is not proportional to the atmospheric scale height, a very unlikely condition. Therefore we consider the correlation between T_{eq} and A_H as real and physical.

The A_H vs. T_{eq} correlation could be caused by physical mechanisms such as cloud formation and longitudinal circulation of heat. [Barstow et al. \(2016\)](#) discussed cloud formation as a continuum process based on atmospheric thermal structure. At cooler atmospheric temperatures, clouds fall deeper while new species condense in the upper atmosphere. This process will naturally leave cooler planets with more extended cloud coverage than hotter planets. Also, planetary heat circulation has been shown to be inefficient for hotter planets ([Cowan and Agol, 2011](#); [Fortney et al., 2008](#)). This means that for the hottest planets, the terminator regions we probe through transmission spectroscopy are likely to be cooler than our equilibrium temperature, and the sub-stellar regions hotter than our equilibrium temperature. Consequently, our calculated scale heights for the hottest planets are arguably too large, and the true scale heights would further strengthen the A_H -temperature correlation and increase the baseline slope.

Unfortunately, with the quality and sample size of current spectra, degeneracies between clouds, temperature and mean molecular weight can not yet be resolved. However, we favor the cloud interpretation because we deem it to be the most physically based and plausible explanation. We infer a selection bias that prefers cooler planets in all the targets observed to date. A greater proportion of the hottest planets, especially at low mass, should be included in future observations to better constrain the correlations, and also to break the mass-temperature degeneracy in the

current sample.

Table 6.1 Absorption in scale heights (A_H), based on spectra from [Tsiaras et al. \(2018\)](#) unless otherwise noted. Our analysis used the A_H values from fitting to the strongest region of water absorption (1.3 - 1.65 μm), versus the entire WFC3 bandpass (1.1 - 1.65 μm), both listed in the middle set of columns. The columns on the right give values for comparison, based on spectra from other authors. T_{eq} calculated from parameters in corresponding references are listed in the left column.

Planet	$T_{eq}(K)$	Absorption (A_H)		Absorption (A_H)		Reference
		1.1 - 1.65 μm	1.3 - 1.65 μm	1.1 - 1.65 μm	1.3 - 1.65 μm	
GJ 436 b	633 \pm 58	0.22 \pm 0.53	0.06 \pm 0.73	1.16 \pm 0.52	0.87 \pm 0.71	Knutson et al. (2014)
GJ 3470 b	692 \pm 101	0.70 \pm 0.30	0.29 \pm 0.41			
HAT-P-1 b	1320 \pm 103	1.50 \pm 0.33	1.27 \pm 0.35	2.51 \pm 0.35	2.88 \pm 0.42	
HAT-P-3 b	1127 \pm 68	0.22 \pm 0.59	0.52 \pm 0.74			
HAT-P-11 b	856 \pm 37	2.96 \pm 0.62	2.31 \pm 0.71	3.21 \pm 0.64	2.70 \pm 0.82	
HAT-P-12 b	958 \pm 28	0.49 \pm 0.21	0.42 \pm 0.25			
HAT-P-17 b	780 \pm 34	0.47 \pm 0.60	0.27 \pm 0.78			
HAT-P-18 b	843 \pm 35	0.90 \pm 0.21	0.51 \pm 0.28			
HAT-P-26 b	980 \pm 56	2.35 \pm 0.26	1.92 \pm 0.31	2.22 \pm 0.18	1.89 \pm 0.20	Wakeford et al. (2017)
HAT-P-32 b	1784 \pm 58	1.48 \pm 0.22	1.30 \pm 0.28			
HAT-P-38 b	1080 \pm 78	1.60 \pm 0.56	2.03 \pm 0.66			
HAT-P-41 b	1937 \pm 74	1.70 \pm 0.39	1.96 \pm 0.45			
HD149026 b	1627 \pm 83	0.79 \pm 0.48	1.09 \pm 0.56			
HD189733 b	1201 \pm 51	2.31 \pm 0.40	1.45 \pm 0.47	1.99 \pm 0.30	1.59 \pm 0.34	McCullough et al. (2014)
HD209458 b	1449 \pm 36	0.88 \pm 0.14	0.78 \pm 0.17	1.26 \pm 0.14	1.12 \pm 0.16	Deming et al. (2013)
WASP-12 b	2580 \pm 146	1.60 \pm 0.23	1.62 \pm 0.31	2.07 \pm 0.36	2.07 \pm 0.36	Kreidberg et al. (2015)
WASP-29 b	963 \pm 69	0.04 \pm 0.39	0.12 \pm 0.49			
WASP-31 b	1576 \pm 58	0.94 \pm 0.33	1.14 \pm 0.42	1.08 \pm 0.38	1.77 \pm 0.43	Sing et al. (2015)
WASP-39 b	1119 \pm 57	1.27 \pm 0.14	1.22 \pm 0.16			
WASP-43 b	1374 \pm 147	1.46 \pm 0.43	0.95 \pm 0.46	1.47 \pm 0.45	0.98 \pm 0.51	Kreidberg et al. (2014b)
WASP-52 b	1300 \pm 115	1.80 \pm 0.24	1.33 \pm 0.28			
WASP-63 b	1508 \pm 69	0.58 \pm 0.27	0.39 \pm 0.30			
WASP-67 b	1026 \pm 59	0.67 \pm 0.52	0.86 \pm 0.70			
WASP-69 b	964 \pm 38	0.62 \pm 0.11	0.65 \pm 0.13			
WASP-74 b	1915 \pm 116	0.77 \pm 0.40	0.97 \pm 0.45			
WASP-76 b	2206 \pm 95	1.35 \pm 0.18	1.62 \pm 0.21			
WASP-80 b	824 \pm 58	0.38 \pm 0.15	0.51 \pm 0.19			
WASP-101 b	1552 \pm 81	0.16 \pm 0.25	0.13 \pm 0.27			
WASP-121 b	2358 \pm 122	2.51 \pm 0.36	2.31 \pm 0.41			
XO-1 b	1196 \pm 60	2.68 \pm 0.66	3.33 \pm 0.76	2.50 \pm 0.56	3.11 \pm 0.72	Deming et al. (2013)
WASP-17b ^a	1632 \pm 126	0.93 \pm 0.33	0.44 \pm 0.35			
WASP-19b ^b	2037 \pm 156	2.16 \pm 0.65	1.60 \pm 0.58			
GJ 1214b ^c	573 \pm 35	0.11 \pm 0.09	0.05 \pm 0.13			
HD97658b ^d	753 \pm 33	0.46 \pm 1.10	1.79 \pm 1.46			

Notes.

^a [Mandell et al. \(2013\)](#)

^b [Huitson et al. \(2013\)](#)

^c [Kreidberg et al. \(2014a\)](#)

^d [Knutson et al. \(2014\)](#)

Chapter 7: Conclusion

7.1 What have we learned about hot Jupiter atmospheres?

In this thesis, I presented detailed studies of four different hot Jupiter atmospheres and also statistical population studies. The data has painted a picture of diverse hot Jupiter atmospheres. Although they are all hot and inflated, their thermal structure and chemical composition can vary widely. While the cooler ones like WASP-74b and HAT-P-41b can exhibit blackbody-like or absorption features from isothermal and decreasing TP profiles, the hotter planets like WASP-76b and KELT-20b can experience stronger thermal dissociation of molecules and more temperature inversion from heavy metal absorbers. Cooler planets are likely more affected by cloud condensations which lead to muted atmospheric features (Fu et al., 2017; Gao et al., 2020). The ultra-hot Jupiters with dayside temperatures exceeding 2200K show significant heavy metal absorbers in the UV/NUV wavelength (Fu et al., 2021; Sing et al., 2019). Host star type also plays a key role in hot Jupiter atmospheres as earlier type stars emit much stronger UV/NUV radiation which preferentially heats up the upper atmospheres and leads to strong thermal inversion (Fu et al., 2022b; Lothringer and Barman, 2019).

7.2 What is next for hot Jupiter atmospheres?

7.2.1 Finding the origin of hot Jupiters through atmospheric characterization

The biggest mystery regarding hot Jupiters is their origin. It is highly surprising that such massive planets can exist so close to the star as we have no analogs in the solar system. Were they formed in situ or further away and migrated inward later on? Studying their atmospheres could provide insights into their formation origin. One method is to precisely constrain the carbon to oxygen ratio (C/O) which could vary depending on where the planet was formed in the protoplanetary disk ([Madhusudhan, 2012](#)). If it was formed beyond the snow line where water is in the ice phase but CO, CO₂, and CH₄ are still in the gas phase, then the atmosphere could have a relatively high C/O ratio as oxygen in the water will mostly be locked up in the core ([Brewer et al., 2017](#)). If the planet was formed much closer to the star where water and carbon-bearing species are all in the gas phase, then we could see a lower C/O ratio in the atmosphere.

Similar to the C/O ratio, we can also measure the refractory-to-volatile ratio. However, this technique is only applicable to the ultra-hot Jupiters where the atmospheric temperatures are high enough (>2000K) for refractory elements like silicon and magnesium to become gaseous. An enriched refractory abundance relative to the volatile could indicate the planet was formed within the snowline where the planetesimals were mostly made of rock instead of ice ([Lothringer et al., 2021](#)).

Both methods will require a large sample of well-characterized hot Jupiter atmospheres with precisely measured C/O and refractory-to-volatile ratios. Fortunately, with JWST operational this summer, we will be able to access the infrared bands where most of the carbon and oxygen-

bearing volatile species reside.

Another method is to measure the isotope ratios in hot Jupiter atmospheres. The isotopic fractionation process can directly probe the formation environment with the deuterium-to-hydrogen (D/H) being the most widely used ratio. Deuterium is enriched relative to the big bang nucleosynthesis level under cold temperatures due to favorable chemical reaction networks (Oberg and Bergin, 2021). D/H has famously been measured in solar system planets and comets to determine the origin of earth's ocean. Due to the naturally low deuterium abundance, it has not yet been detected in any extrasolar objects. However, carbon isotope ^{13}C has been measured in brown dwarfs and hot Jupiter (Line et al., 2021; Zhang et al., 2021) atmospheres. The 12/13 carbon isotope ratio could also be diagnostic for determining planetary formation origins as we have seen varying 12/13 CO ratios in protoplanetary disks (Yoshida et al., 2022). JWST may be able to detect ^{13}CO if the CO feature is strong but high-resolution spectroscopy from the ground may be the more promising path (Line et al., 2021; Zhang et al., 2021).

7.2.2 Understanding the chemical and physical processes of hot Jupiters

The short period, tidally locked, and high temperature makes hot Jupiters unique targets to test our atmospheric models under the most extreme environments. They are planets that have the surface cooked to almost stellar photosphere temperatures. Our current understanding relies on both planetary atmosphere models based on solar system planets and stellar models. Hot Jupiter's atmospheric circulation and dynamics resemble planetary objects, but opacity and chemistry are more akin to brown dwarfs and low mass stars. The full picture of hot Jupiter atmospheres will be the combination of the two sides.

With JWST opening up the infrared window we will have access to many more chemical species than before, and here are the top questions that we will be able to answer about hot Jupiter atmospheres: 1) Metallicity of these planets and if they are similar to the mass-metallicity correlation we have seen in the solar system? ([Wakeford et al., 2017](#); [Welbanks et al., 2019](#)) 2) Various chemical abundance ratios and how can they tell us about the formation process? ([Madhusudhan, 2012](#); [Oberg et al., 2011](#)) 3) Thermal structure and what causes inversion? ([Fortney et al., 2008](#); [Lothringer et al., 2018](#)) 4) How do atmospheric dynamics and circulation work on a tidally locked planet with permanent day and night sides? ([Komacek et al., 2017](#); [Showman et al., 2009](#)) 5) Under what conditions do clouds condense and form? ([Gao et al., 2021](#); [Morley et al., 2013](#))

7.3 What is beyond hot Jupiter atmospheres?

Hot Jupiters are a stepping stone toward searching for evidence of life beyond Earth. Earth is currently the only habitable planet that we know and based on this one data point we are searching for another planet that resembles the conditions on earth. Transiting exoplanets are ideal for atmospheric characterization when they have a relatively large radius to the host star, an inflated atmosphere, and a short period for frequent transits. While all these conditions are true for hot Jupiters, they are not for an earth analog. Earth is only about 1% of the Sun in radius and 100ppm in transit depth. Earth's atmosphere is less than 1% of Earth's radius which means any atmospheric feature signals will be <1ppm. This level of precision needed is currently orders of magnitude higher than what we have achieved. More importantly, sub-ppm level precision is also below many noise floors (detector, stellar, telescope systematics, etc...) that we currently

know. Therefore, to truly study atmospheric signals from an Earth-like planet around a Sun-like star requires not only a bigger space telescope ($> 30\text{m}$), but we will also need breakthroughs on high-contrast direct imaging technology. Atmospheric characterization of an exo-Earth may be a lofty goal for the near future specifically for transiting exoplanet studies and JWST.

If the true Earth twin is out of reach, we may be able to study Earth cousins. These planets can have a similar temperature, mass, and radius as Earth but orbit a smaller M dwarf star. The most famous system will be TRAPPIST-1 (Gillon et al., 2016) which hosts seven small Earth-sized rocky planets. The late M8 type host star is only about 10% of the Sun's radius which means an Earth-sized planet will have about 1% transit depth and potential atmospheric features could be on the order of 10s ppm. This is much more achievable with JWST and current technologies. The much shorter periods also mean more frequent transits compared to an Earth twin. However, these Earth-like planets around M dwarf stars are most likely to be tidally locked due to the close-in orbits, and they are more vulnerable to flares and stellar activities which are expected to be more common on M dwarfs. JWST will give us the first glimpse of these planets' atmospheres if they are not bare rocks.

Appendix A: Facilities and Software

We made use of the following facilities and software while conducting the research described in this dissertation.

A.1 Facilities

1. Mikulski Archive for Space Telescopes (MAST, <https://archive.stsci.edu/>)

A.2 Software

1. BATMAN (<https://github.com/lkreidberg/batman>) (Kreidberg, 2015)
2. corner.py (<https://corner.readthedocs.io/en/latest/index.html> (Foreman-Mackey et al., 2013))
3. Exo-Transit (<https://github.com/elizakempton/ExoTransmit> (Kempton et al., 2017))
4. MCMC (<https://emcee.readthedocs.io/en/stable/> (Foreman-Mackey et al., 2013))
5. PLATON (<https://github.com/ideasrule/platon> (Zhang et al., 2020))
6. RECTE (<https://recte.readthedocs.io/en/latest/index.html> (Zhou et al., 2017))

Bibliography

- Akritas, M. G. and Bershad, M. A. (1996). Linear Regression for Astronomical Data with Measurement Errors and Intrinsic Scatter. *The Astrophysical Journal*, 470:706. arXiv: astro-ph/9605002.
- Alam, M. K., López-Morales, M., Nikolov, N., Sing, D. K., Henry, G. W., Baxter, C., Désert, J.-M., Barstow, J. K., Mikal-Evans, T., Bourrier, V., Lavvas, P., Wakeford, H. R., Williamson, M. H., Sanz-Forcada, J., Buchhave, L. A., Cohen, O., and Muñoz, A. G. (2020). The Hubble Space Telescope PanCET Program: An Optical to Infrared Transmission Spectrum of HAT-P-32Ab. *The Astronomical Journal*, 160(1):51. Publisher: American Astronomical Society.
- Alexoudi, X., Mallonn, M., von Essen, C., Turner, J. D., Keles, E., Southworth, J., Mancini, L., Ciceri, S., Granzer, T., Denker, C., Dineva, E., and Strassmeier, K. G. (2018). Deciphering the atmosphere of HAT-P-12b: solving discrepant results. *Astronomy & Astrophysics*, 620:A142.
- Allan, D. (1966). Statistics of atomic frequency standards. *Proceedings of the IEEE*, 54(2):221–230. Conference Name: Proceedings of the IEEE.
- Allart, R., Bourrier, V., Lovis, C., Ehrenreich, D., Spake, J. J., Wyttenbach, A., Pino, L., Pepe, F., Sing, D. K., and Etangs, A. L. d. (2018). Spectrally resolved helium absorption from the extended atmosphere of a warm Neptune-mass exoplanet. *Science*, 362(6421):1384–1387. arXiv: 1812.02189.
- Amundsen, D. S., Baraffe, I., Tremblin, P., Manners, J., Hayek, W., Mayne, N. J., and Acreman, D. M. (2014). Accuracy tests of radiation schemes used in hot Jupiter global circulation models. *Astronomy & Astrophysics*, 564:A59.
- Arcangeli, J., Desert, J.-M., Line, M. R., Bean, J. L., Parmentier, V., Stevenson, K. B., Kreidberg, L., Fortney, J. J., Mansfield, M., and Showman, A. P. (2018). H- Opacity and Water Dissociation in the Dayside Atmosphere of the Very Hot Gas Giant WASP-18 b. *The Astrophysical Journal*, 855(2):L30. arXiv: 1801.02489.
- Arcangeli, J., Desert, J.-M., Parmentier, V., Stevenson, K. B., Bean, J. L., Line, M. R., Kreidberg, L., Fortney, J. J., and Showman, A. P. (2019). Climate of an Ultra hot Jupiter: Spectroscopic phase curve of WASP-18b with HST/WFC3. *Astronomy & Astrophysics*, 625:A136. arXiv: 1904.02069.

- Barstow, J. K., Aigrain, S., Irwin, P. G. J., and Sing, D. K. (2016). A consistent retrieval analysis of 10 hot Jupiters observed in transmission. *The Astrophysical Journal*, 834(1):50.
- Baxter, C., Désert, J.-M., Tsai, S.-M., Todorov, K. O., Bean, J. L., Deming, D., Parmentier, V., Fortney, J. J., Line, M., Thorngren, D., Pierrehumbert, R. T., Burrows, A., and Showman, A. P. (2021). Evidence for disequilibrium chemistry from vertical mixing in hot Jupiter atmospheres. A comprehensive survey of transiting close-in gas giant exoplanets with warm-Spitzer/IRAC. *Astronomy & Astrophysics*, 648:39. arXiv: 2103.07185.
- Beatty, T. G., Madhusudhan, N., Tsiaras, A., Zhao, M., Gilliland, R. L., Knutson, H. A., Shporer, A., and Wright, J. T. (2017). Evidence for Atmospheric Cold-trap Processes in the Noninverted Emission Spectrum of Kepler-13Ab Using *HST* /WFC3. *The Astronomical Journal*, 154(4):158.
- Bohn, A. J., Southworth, J., Ginski, C., Kenworthy, M. A., Maxted, P. F. L., and Evans, D. F. (2020). A multiplicity study of transiting exoplanet host stars: I. High-contrast imaging with VLT/SPHERE. *Astronomy & Astrophysics*, 635:A73.
- Brewer, J. M., Fischer, D. A., and Madhusudhan, N. (2017). C/O and O/H Ratios Suggest Some Hot Jupiters Originate Beyond the Snow Line. *The Astronomical Journal*, 153(2):83. arXiv: 1612.04372.
- Burrows, A. and Sharp, C. M. (1999). Chemical Equilibrium Abundances in Brown Dwarf and Extrasolar Giant Planet Atmospheres. *The Astrophysical Journal*, 512(2):843–863.
- Campo, C. J., Harrington, J., Hardy, R. A., Stevenson, K. B., Nymeyer, S., Ragozzine, D., Lust, N. B., Anderson, D. R., Collier-Cameron, A., Blecic, J., Britt, C. B. T., Bowman, W. C., Wheatley, P. J., Loredó, T. J., Deming, D., Hebb, L., Hellier, C., Maxted, P. F. L., Pollaco, D., and West, R. G. (2011). On the orbit of exoplanet WASP-12b. *The Astrophysical Journal*, 727(2):125.
- Casasayas-Barris, N., Pallé, E., Yan, F., Chen, G., Kohl, S., Stangret, M., Parviainen, H., Helling, C., Watanabe, N., Czesla, S., Fukui, A., Montañés-Rodríguez, P., Nagel, E., Narita, N., Nortmann, L., Nowak, G., Schmitt, J. H. M. M., and Zapatero Osorio, M. R. (2019). Atmospheric characterization of the ultra-hot Jupiter MASCARA-2b/KELT-20b: Detection of CaII, FeII, NaI, and the Balmer series of H (H γ , H δ , and H ϵ) with high-dispersion transit spectroscopy. *Astronomy & Astrophysics*, 628:A9.
- Charbonneau, D., Brown, T. M., Noyes, R. W., and Gilliland, R. L. (2002). Detection of an Extrasolar Planet Atmosphere. *The Astrophysical Journal*, 568(1):377–384.
- Claret, A., Hauschildt, P. H., and Witte, S. (2013). New limb-darkening coefficients for Phoenix/1d model atmospheres: II. Calculations for 5000 K T_{eff} 10 000 K *Kepler*, CoRot, *Spitzer*, *uvby*, *UBVRIJHK*, Sloan, and 2MASS photometric systems. *Astronomy & Astrophysics*, 552:A16.
- Colón, K. D., Kreidberg, L., Welbanks, L., Line, M. R., Madhusudhan, N., Beatty, T., Tamburo, P., Stevenson, K. B., Mandell, A., Rodríguez, J. E., Barclay, T., Lopez, E. D., Stassun, K. G.,

- Angerhausen, D., Fortney, J. J., James, D. J., Pepper, J., Ahlers, J. P., Plavchan, P., Awiphan, S., Kotnik, C., McLeod, K. K., Murawski, G., Chotani, H., LeBrun, D., Matzko, W., Rea, D., Vidaurri, M., Webster, S., Williams, J. K., Cox, L. S., Tan, N., and Gilbert, E. A. (2020). An Unusual Transmission Spectrum for the Sub-Saturn KELT-11b Suggestive of a Subsolar Water Abundance. *The Astronomical Journal*, 160(6):280.
- Cowan, N. B. and Agol, E. (2011). The statistics of albedo and heat recirculation on hot exoplanets. *The Astrophysical Journal*, 729(1):54.
- Crossfield, I. J. M., Barman, T., Hansen, B. M. S., Tanaka, I., and Kodama, T. (2012). Re-evaluating WASP-12b: strong emission at 2.315 μ m, deeper occultations, and an isothermal atmosphere. *The Astrophysical Journal*, 760(2):140.
- Crossfield, I. J. M. and Kreidberg, L. (2017). Trends in Atmospheric Properties of Neptune-size Exoplanets. *The Astronomical Journal*, 154(6):261.
- Cubillos, P., Harrington, J., Madhusudhan, N., Stevenson, K. B., Hardy, R. A., Blecic, J., Anderson, D. R., Hardin, M., and Campo, C. J. (2013). WASP-8b: characterization of a cool and eccentric exoplanet with *Spitzer*. *The Astrophysical Journal*, 768(1):42.
- Currie, T., Biller, B., Lagrange, A.-M., Marois, C., Guyon, O., Nielsen, E., Bonnefoy, M., and De Rosa, R. (2022). Direct Imaging and Spectroscopy of Extrasolar Planets. Technical Report arXiv:2205.05696, arXiv. arXiv:2205.05696 [astro-ph] type: article.
- Dawson, R. I. and Johnson, J. A. (2018). Origins of Hot Jupiters. *Annual Review of Astronomy and Astrophysics*, 56(1):175–221. arXiv: 1801.06117.
- Deming, D., Knutson, H., Kammer, J., Fulton, B. J., Ingalls, J., Carey, S., Burrows, A., Fortney, J. J., Todorov, K., Agol, E., Cowan, N., Desert, J.-M., Fraine, J., Langton, J., Morley, C., and Showman, A. P. (2015). *Spitzer* Secondary Eclipses of the Dense, Modestly-irradiated, Giant Exoplanet HAT-P-20b Using Pixel-Level Decorrelation. *The Astrophysical Journal*, 805(2):132. arXiv: 1411.7404.
- Deming, D. and Knutson, H. A. (2020). Highlights of exoplanetary science from *Spitzer*. *Nature Astronomy*, 4(5):453–466. Number: 5 Publisher: Nature Publishing Group.
- Deming, D., Wilkins, A., McCullough, P., Burrows, A., Fortney, J. J., Agol, E., Dobbs-Dixon, I., Madhusudhan, N., Crouzet, N., Desert, J.-M., Gilliland, R. L., Haynes, K., Knutson, H. A., Line, M., Magic, Z., Mandell, A. M., Ranjan, S., Charbonneau, D., Clampin, M., Seager, S., and Showman, A. P. (2013). Infrared Transmission Spectroscopy of the Exoplanets HD209458b and XO-1b Using the Wide Field Camera-3 on the Hubble Space Telescope. *The Astrophysical Journal*, 774(2):95. arXiv: 1302.1141.
- Drummond, B., Tremblin, P., Baraffe, I., Amundsen, D. S., Mayne, N. J., Venot, O., and Goyal, J. (2016). The effects of consistent chemical kinetics calculations on the pressure-temperature profiles and emission spectra of hot Jupiters. *Astronomy & Astrophysics*, 594:A69.

- Eastman, J. D., Rodriguez, J. E., Agol, E., Stassun, K. G., Beatty, T. G., Vanderburg, A., Gaudi, B. S., Collins, K. A., and Luger, R. (2019). EXOFASTv2: A public, generalized, publication-quality exoplanet modeling code. *Astrophysics Source Code Library*, 1710.003.
- Edwards, B., Changeat, Q., Baeyens, R., Tsiaras, A., Al-Refaie, A., Taylor, J., Yip, K. H., Bieger, M. F., Blain, D., Gressier, A., Guilluy, G., Jaziri, A. Y., Kiefer, F., Modirrousta-Galian, D., Morvan, M., Mugnai, L. V., Pluriel, W., Poveda, M., Skaf, N., Whiteford, N., Wright, S., Zingales, T., Charnay, B., Drossart, P., Leconte, J., Venot, O., Waldmann, I., and Beaulieu, J.-P. (2020). ARES I: WASP-76 b, A Tale of Two HST Spectra. *The Astronomical Journal*, 160(1):8. arXiv: 2005.02374.
- Ehrenreich, D., Bourrier, V., Wheatley, P. J., Etangs, A. L. d., Hébrard, G., Udry, S., Bonfils, X., Delfosse, X., Désert, J.-M., Sing, D. K., and Vidal-Madjar, A. (2015). A giant comet-like cloud of hydrogen escaping the warm Neptune-mass exoplanet GJ 436b. *Nature*, 522(7557):459–461. arXiv: 1506.07541.
- Ehrenreich, D., Lovis, C., Allart, R., Zapatero Osorio, M. R., Pepe, F., Cristiani, S., Rebolo, R., Santos, N. C., Borsa, F., Demangeon, O., Dumusque, X., González Hernández, J. I., Casasayas-Barris, N., Ségransan, D., Sousa, S., Abreu, M., Adibekyan, V., Affolter, M., Allende Prieto, C., Alibert, Y., Aliverti, M., Alves, D., Amate, M., Avila, G., Baldini, V., Bandy, T., Benz, W., Bianco, A., Bolmont, , Bouchy, F., Bourrier, V., Broeg, C., Cabral, A., Calderone, G., Pallé, E., Cegla, H. M., Cirami, R., Coelho, J. M. P., Conconi, P., Coretti, I., Cumani, C., Cupani, G., Dekker, H., Delabre, B., Deiries, S., D’Odorico, V., Di Marcantonio, P., Figueira, P., Fragoso, A., Genolet, L., Genoni, M., Génova Santos, R., Hara, N., Hughes, I., Iwert, O., Kerber, F., Knudstrup, J., Landoni, M., Lavie, B., Lizon, J.-L., Lendl, M., Lo Curto, G., Maire, C., Manescau, A., Martins, C. J. a. P., Mégevand, D., Mehner, A., Micela, G., Modigliani, A., Molaro, P., Monteiro, M., Monteiro, M., Moschetti, M., Müller, E., Nunes, N., Oggioni, L., Oliveira, A., Pariani, G., Pasquini, L., Poretti, E., Rasilla, J. L., Redaelli, E., Riva, M., Santana Tschudi, S., Santin, P., Santos, P., Segovia Milla, A., Seidel, J. V., Sosnowska, D., Sozzetti, A., Spanò, P., Suárez Mascareño, A., Tabernero, H., Tenegi, F., Udry, S., Zanutta, A., and Zerbi, F. (2020). Nightside condensation of iron in an ultrahot giant exoplanet. *Nature*, 580(7805):597–601.
- Evans, T. M., Sing, D. K., Kataria, T., Goyal, J., Nikolov, N., Wakeford, H. R., Deming, D., Marley, M. S., Amundsen, D. S., Ballester, G. E., Barstow, J. K., Ben-Jaffel, L., Bourrier, V., Buchhave, L. A., Cohen, O., Ehrenreich, D., García Muñoz, A., Henry, G. W., Knutson, H., Lavvas, P., Etangs, A. L. d., Lewis, N. K., López-Morales, M., Mandell, A. M., Sanz-Forcada, J., Tremblin, P., and Lupu, R. (2017). An ultrahot gas-giant exoplanet with a stratosphere. *Nature*, 548(7665):58–61.
- Fazio, G. G., Hora, J. L., Allen, L. E., Ashby, M. L. N., Barmby, P., Deutsch, L. K., Huang, J., Kleiner, S., Marengo, M., Megeath, S. T., Melnick, G. J., Pahre, M. A., Patten, B. M., Polizotti, J., Smith, H. A., Taylor, R. S., Wang, Z., Willner, S. P., Hoffmann, W. F., Pipher, J. L., Forrest, W. J., McMurty, C. W., McCreight, C. R., McKelvey, M. E., McMurray, R. E., Koch, D. G., Moseley, S. H., Arendt, R. G., Mentzell, J. E., Marx, C. T., Losch, P., Mayman, P., Eichhorn, W., Krebs, D., Jhabvala, M., Gezari, D. Y., Fixsen, D. J., Flores, J., Shakoorzadeh, K., Jungo,

- R., Hakun, C., Workman, L., Karpati, G., Kichak, R., Whitley, R., Mann, S., Tollestrup, E. V., Eisenhardt, P., Stern, D., Gorjian, V., Bhattacharya, B., Carey, S., Nelson, B. O., Glaccum, W. J., Lacy, M., Lowrance, P. J., Laine, S., Reach, W. T., Stauffer, J. A., Surace, J. A., Wilson, G., Wright, E. L., Hoffman, A., Domingo, G., and Cohen, M. (2004). The Infrared Array Camera (IRAC) for the *Spitzer Space Telescope*. *The Astrophysical Journal Supplement Series*, 154(1):10–17.
- Foreman-Mackey, D., Hogg, D. W., Lang, D., and Goodman, J. (2013). emcee: The MCMC Hammer. *Publications of the Astronomical Society of the Pacific*, 125(925):306–312. arXiv: 1202.3665.
- Fortney, J., Lodders, K., Marley, M., and Freedman, R. (2008). A Unified Theory for the Atmospheres of the Hot and Very Hot Jupiters: Two Classes of Irradiated Atmospheres. *The Astrophysical Journal*, 678(2):1419–1435.
- Fortney, J. J., Dawson, R. I., and Komacek, T. D. (2021). Hot Jupiters: Origins, Structure, Atmospheres. *Journal of Geophysical Research: Planets*, 126(3):e2020JE006629. eprint: <https://onlinelibrary.wiley.com/doi/pdf/10.1029/2020JE006629>.
- Fu, G., Deming, D., Knutson, H., Madhusudhan, N., Mandell, A., and Fraine, J. (2017). Statistical Analysis of Hubble/WFC3 Transit Spectroscopy of Extrasolar Planets. *The Astrophysical Journal Letters*, 847:L22.
- Fu, G., Deming, D., May, E., Stevenson, K., Sing, D. K., Lothringer, J. D., Wakeford, H. R., Nikolov, N., Mikal-Evans, T., Bourrier, V., dos Santos, L. A., Alam, M. K., Henry, G. W., Muñoz, A. G., and López-Morales, M. (2021). The Hubble PanCET program: Transit and Eclipse Spectroscopy of the Hot-Jupiter WASP-74b. *The Astronomical Journal*, 162(6):271.
- Fu, G., Sing, D. K., Deming, D., Sheppard, K., Wakeford, H. R., Mikal-Evans, T., Alam, M. K., Dos Santos, L. A., López-Morales, M., and Lothringer, J. D. (2022a). The Hubble PanCET Program: Emission Spectrum of Hot Jupiter HAT-P-41b. *The Astronomical Journal*, 163(4):190.
- Fu, G., Sing, D. K., Lothringer, J. D., Deming, D., Ih, J., Kempton, E. M. R., Malik, M., Komacek, T. D., Mansfield, M., and Bean, J. L. (2022b). Strong H₂O and CO Emission Features in the Spectrum of KELT-20b Driven by Stellar UV Irradiation. *The Astrophysical Journal Letters*, 925(1):L3.
- Gao, P., Thorngren, D. P., Lee, G. K. H., Fortney, J. J., Morley, C. V., Wakeford, H. R., Powell, D. K., Stevenson, K. B., and Zhang, X. (2020). Aerosol Composition of Hot Giant Exoplanets Dominated by Silicates and Hydrocarbon Hazes. *Nature Astronomy*, 4(10):951–956. arXiv: 2005.11939.
- Gao, P., Wakeford, H. R., Moran, S. E., and Parmentier, V. (2021). Aerosols in Exoplanet Atmospheres. *Journal of Geophysical Research: Planets*, 126(4). arXiv: 2102.03480.
- Garhart, E., Deming, D., Mandell, A., Knutson, H. A., Wallack, N., Burrows, A., Fortney, J. J., Hood, C., Seay, C., Sing, D. K., Benneke, B., Fraine, J. D., Kataria, T., Lewis, N.,

- Madhusudhan, N., McCullough, P., Stevenson, K. B., and Wakeford, H. (2020). Statistical Characterization of Hot Jupiter Atmospheres using Spitzer’s Secondary Eclipses. *The Astronomical Journal*, 159(4):137. arXiv: 1901.07040.
- Gillon, M., Jehin, E., Lederer, S. M., Delrez, L., de Wit, J., Burdanov, A., Van Grootel, V., Burgasser, A. J., Triaud, A. H. M. J., Opitom, C., Demory, B.-O., Sahu, D. K., Bardalez Gagliuffi, D., Magain, P., and Queloz, D. (2016). Temperate Earth-sized planets transiting a nearby ultracool dwarf star. *Nature*, 533(7602):221–224.
- Goldreich, P. and Soter, S. (1966). Q in the solar system. *Icarus*, 5(1):375–389.
- Goyal, J. M., Mayne, N., Sing, D. K., Drummond, B., Tremblin, P., Amundsen, D. S., Evans, T., Carter, A. L., Spake, J., Baraffe, I., Nikolov, N., Manners, J., Chabrier, G., and Hebrard, E. (2018). A library of ATMO forward model transmission spectra for hot Jupiter exoplanets. *Monthly Notices of the Royal Astronomical Society*, 474(4):5158–5185. arXiv: 1710.10269.
- Griffith, C. A. (2014). Disentangling degenerate solutions from primary transit and secondary eclipse spectroscopy of exoplanets. *Philosophical Transactions of the Royal Society A: Mathematical, Physical and Engineering Sciences*, 372(2014):20130086. Publisher: Royal Society.
- Guillot, T., Burrows, A., Hubbard, W. B., Lunine, J. I., and Saumon, D. (1996). Giant Planets at Small Orbital Distances. *The Astrophysical Journal*, 459(1).
- Hartman, J. D., Bakos, G. A., Béky, B., Torres, G., Latham, D. W., Csubry, Z., Penev, K., Shporer, A., Fulton, B. J., Buchhave, L. A., Johnson, J. A., Howard, A. W., Marcy, G. W., Fischer, D. A., Kovács, G., Noyes, R. W., Esquerdo, G. A., Everett, M., Szklenár, T., Quinn, S. N., Bieryla, A., Knox, R. P., Hinz, P., Sasselov, D. D., Fűrész, G., Stefanik, R. P., Lázár, J., Papp, I., and Sári, P. (2012). HAT-P-39b–HAT-P-41b: three highly inflated transiting hot Jupiters. *The Astronomical Journal*, 144(5):139.
- Haynes, K., Mandell, A. M., Madhusudhan, N., Deming, D., and Knutson, H. (2015). Spectroscopic evidence for a temperature inversion in the dayside atmosphere of hot Jupiter WASP-33b. *The Astrophysical Journal*, 806(2):146.
- Hellier, C., Anderson, D. R., Collier Cameron, A., Delrez, L., Gillon, M., Jehin, E., Lendl, M., Maxted, P. F. L., Pepe, F., Pollacco, D., Queloz, D., Ségransan, D., Smalley, B., Smith, A. M. S., Southworth, J., Triaud, A. H. M. J., Turner, O. D., Udry, S., and West, R. G. (2015). Three WASP-south transiting exoplanets: WASP-74b, WASP-83b, and WASP-89b. *The Astronomical Journal*, 150(1):18.
- Heng, K. and Kitzmann, D. (2017). The theory of transmission spectra revisited: a semi-analytical method for interpreting WFC3 data and an unresolved challenge. *Monthly Notices of the Royal Astronomical Society*, 470(3):2972–2981.
- Henry, G. W., Fekel, F. C., and Henry, S. M. (2011). A volume-limited photometric survey of 114 doradus candidates. *The Astronomical Journal*, 142(2):39.

- Henry, G. W., Marcy, G. W., Butler, R. P., and Vogt, S. S. (2000). A Transiting “51 Peg-like” Planet. *The Astrophysical Journal*, 529(1):L41–L44.
- Hoeijmakers, H. J., Cabot, S. H. C., Zhao, L., Buchhave, L. A., Tronsgaard, R., Davis, A. B., Kitzmann, D., Grimm, S. L., Cegla, H. M., Bourrier, V., Ehrenreich, D., Heng, K., Lovis, C., and Fischer, D. A. (2020). High-resolution transmission spectroscopy of MASCARA-2 b with EXPRES. *Astronomy & Astrophysics*, 641:A120.
- Huitson, C. M., Sing, D. K., Pont, F., Fortney, J. J., Burrows, A. S., Wilson, P. A., Ballester, G. E., Nikolov, N., Gibson, N. P., Deming, D., Aigrain, S., Evans, T. M., Henry, G. W., Lecavelier des Etangs, A., Showman, A. P., Vidal-Madjar, A., and Zahnle, K. (2013). An HST optical-to-near-IR transmission spectrum of the hot Jupiter WASP-19b: detection of atmospheric water and likely absence of TiO. *Monthly Notices of the Royal Astronomical Society*, 434(4):3252–3274.
- Husser, T.-O., Wende-von Berg, S., Dreizler, S., Homeier, D., Reiners, A., Barman, T., and Hauschildt, P. H. (2013). A new extensive library of PHOENIX stellar atmospheres and synthetic spectra. *Astronomy & Astrophysics*, 553:A6.
- Ingalls, J. G., Krick, J. E., Carey, S. J., Stauffer, J. R., Lowrance, P. J., Grillmair, C. J., Buzasi, D., Deming, D., Diamond-Lowe, H., Evans, T. M., Morello, G., Stevenson, K. B., Wong, I., Capak, P., Glaccum, W., Laine, S., Surace, J., and Storrie-Lombardi, L. (2016). Repeatability and accuracy of exoplanet eclipse depths measured with post-cryogenic *Spitzer*. *The Astronomical Journal*, 152(2):44.
- Jack, D., Hauschildt, P. H., and Baron, E. (2009). Time-dependent radiative transfer with PHOENIX. *Astronomy & Astrophysics*, 502(3):1043–1049.
- Kasting, J. F. and Catling, D. (2003). Evolution of a Habitable Planet. *Annual Review of Astronomy and Astrophysics*, 41(1):429–463.
- Kataria, T., Sing, D. K., Lewis, N. K., Visscher, C., Showman, A. P., Fortney, J. J., and Marley, M. S. (2016). The atmospheric circulation of a nine-hot-Jupiter sample: probing circulation and chemistry over a wide phase space. *The Astrophysical Journal*, 821(1):9.
- Kempton, E. M.-R., Lupu, R., Owusu-Asare, A., Slough, P., and Cale, B. (2017). Exo-Transmit: An Open-Source Code for Calculating Transmission Spectra for Exoplanet Atmospheres of Varied Composition. *Publications of the Astronomical Society of the Pacific*, 129(974):044402.
- Kipping, D. M. (2010). Binning is sinning: morphological light-curve distortions due to finite integration time: Binning is sinning. *Monthly Notices of the Royal Astronomical Society*, 408(3):1758–1769.
- Kirk, J., Alam, M. K., López-Morales, M., and Zeng, L. (2020). Confirmation of WASP-107b’s Extended Helium Atmosphere with Keck II/NIRSPEC. *The Astronomical Journal*, 159(3):115.
- Knutson, H. A., Benneke, B., Deming, D., and Homeier, D. (2014). A featureless transmission spectrum for the Neptune-mass exoplanet GJ 436b. *Nature*, 505(7481):66–68.

- Komacek, T. D., Showman, A. P., and Tan, X. (2017). Atmospheric Circulation of Hot Jupiters: Dayside–Nightside Temperature Differences. II. Comparison with Observations. *The Astrophysical Journal*, 835(2):198.
- Kreidberg, L. (2015). batman: BASeic Transit Model cAlculationN in Python. *Publications of the Astronomical Society of the Pacific*, 127(957):1161.
- Kreidberg, L., Bean, J. L., Désert, J.-M., Benneke, B., Deming, D., Stevenson, K. B., Seager, S., Berta-Thompson, Z., Seifahrt, A., and Homeier, D. (2014a). Clouds in the atmosphere of the super-Earth exoplanet GJ 1214b. *Nature*, 505(7481):69–72.
- Kreidberg, L., Bean, J. L., Désert, J.-M., Line, M. R., Fortney, J. J., Madhusudhan, N., Stevenson, K. B., Showman, A. P., Charbonneau, D., McCullough, P. R., Seager, S., Burrows, A., Henry, G. W., Williamson, M., Kataria, T., and Homeier, D. (2014b). A Precise Water Abundance Measurement for the Hot Jupiter WASP-43b. *The Astrophysical Journal*, 793(2):L27. arXiv: 1410.2255.
- Kreidberg, L., Line, M. R., Bean, J. L., Stevenson, K. B., Désert, J.-M., Madhusudhan, N., Fortney, J. J., Barstow, J. K., Henry, G. W., Williamson, M. H., and Showman, A. P. (2015). A detection of water in the transmission spectrum of the hot Jupiter WASP-12b and implications for its atmospheric composition. *The Astrophysical Journal*, 814(1):66.
- Kreidberg, L., Line, M. R., Parmentier, V., Stevenson, K. B., Louden, T., Bonnefoy, M., Faherty, J. K., Henry, G. W., Williamson, M. H., Stassun, K., Beatty, T. G., Bean, J. L., Fortney, J. J., Showman, A. P., Désert, J.-M., and Arcangeli, J. (2018a). Global Climate and Atmospheric Composition of the Ultra-hot Jupiter WASP-103b from *HST* and *Spitzer* Phase Curve Observations. *The Astronomical Journal*, 156(1):17.
- Kreidberg, L., Line, M. R., Thorngren, D., Morley, C. V., and Stevenson, K. B. (2018b). Water, High-altitude Condensates, and Possible Methane Depletion in the Atmosphere of the Warm Super-Neptune WASP-107b. *The Astrophysical Journal*, 858(1):L6.
- Latham, D. W., Mazeh, T., Stefanik, R. P., Mayor, M., and Burki, G. (1989). The unseen companion of HD114762: a probable brown dwarf. *Nature*, 339(6219):38–40.
- Lewis, N. K., Wakeford, H. R., MacDonald, R. J., Goyal, J. M., Sing, D. K., Barstow, J., Powell, D., Kataria, T., Mishra, I., Marley, M. S., Batalha, N. E., Moses, J. I., Gao, P., Wilson, T. J., Chubb, K. L., Mikal-Evans, T., Nikolov, N., Pirzkal, N., Spake, J. J., Stevenson, K. B., Valenti, J., and Zhang, X. (2020). Into the UV: The Atmosphere of the Hot Jupiter HAT-P-41b Revealed. *The Astrophysical Journal Letters*, 902(1):L19. arXiv: 2010.08551.
- Line, M. R., Brogi, M., Bean, J. L., Gandhi, S., Zalesky, J., Parmentier, V., Smith, P., Mace, G. N., Mansfield, M., Kempton, E. M.-R., Fortney, J. J., Shkolnik, E., Patience, J., Rauscher, E., Désert, J.-M., and Wardenier, J. P. (2021). A solar C/O and sub-solar metallicity in a hot Jupiter atmosphere. *Nature*, 598(7882):580–584.
- Line, M. R., Knutson, H., Wolf, A. S., and Yung, Y. L. (2014). A systematic retrieval analysis of secondary eclipse spectra. II. a uniform analysis of nine planets and their C to O ratios. *The Astrophysical Journal*, 783(2):70.

- Line, M. R., Stevenson, K. B., Bean, J., Desert, J.-M., Fortney, J. J., Kreidberg, L., Madhusudhan, N., Showman, A. P., and Diamond-Lowe, H. (2016). No thermal inversion and a solar water abundance for the hot Jupiter HD209458b from *HST*/WFC3 spectroscopy. *The Astronomical Journal*, 152(6):203.
- Line, M. R., Wolf, A., Zhang, X., Knutson, H., Kammer, J., Ellison, E., Deroo, P., Crisp, D., and Yung, Y. (2013). A Systematic Retrieval Analysis of Secondary Eclipse Spectra I: A Comparison of Atmospheric Retrieval Techniques. *The Astrophysical Journal*, 775(2):137. arXiv: 1304.5561.
- Lothringer, J. D. and Barman, T. (2019). The Influence of Host Star Spectral Type on Ultra-hot Jupiter Atmospheres. *The Astrophysical Journal*, 876(1):69.
- Lothringer, J. D., Barman, T., and Koskinen, T. (2018). Extremely Irradiated Hot Jupiters: Non-oxide Inversions, H Opacity, and Thermal Dissociation of Molecules. *The Astrophysical Journal*, 866(1):27.
- Lothringer, J. D., Fu, G., Sing, D. K., and Barman, T. S. (2020). UV Exoplanet Transmission Spectral Features as Probes of Metals and Rainout. *The Astrophysical Journal*, 898(1):L14.
- Lothringer, J. D., Rustamkulov, Z., Sing, D. K., Gibson, N. P., Wilson, J., and Schlaufman, K. C. (2021). A New Window into Planet Formation and Migration: Refractory-to-Volatile Elemental Ratios in Ultra-hot Jupiters. *The Astrophysical Journal*, 914(1):12.
- Lothringer, J. D., Sing, D. K., Rustamkulov, Z., Wakeford, H. R., Stevenson, K. B., Nikolov, N., Lavvas, P., Spake, J. J., and Winch, A. T. (2022). UV absorption by silicate cloud precursors in ultra-hot Jupiter WASP-178b. *Nature*, 604(7904):49–52.
- Lund, M. B., Rodriguez, J. E., Zhou, G., Gaudi, B. S., Stassun, K. G., Johnson, M. C., Bieryla, A., Oelkers, R. J., Stevens, D. J., Collins, K. A., Penev, K., Quinn, S. N., Latham, D. W., Villanueva, S., Eastman, J. D., Kielkopf, J. F., Oberst, T. E., Jensen, E. L. N., Cohen, D. H., Joner, M. D., Stephens, D. C., Relles, H., Corfini, G., Gregorio, J., Zambelli, R., Esquerdo, G. A., Calkins, M. L., Berlind, P., Ciardi, D. R., Dressing, C., Patel, R., Gagnon, P., Gonzales, E., Beatty, T. G., Siverd, R. J., Labadie-Bartz, J., Kuhn, R. B., Colón, K. D., James, D., Pepper, J., Fulton, B. J., McLeod, K. K., Stockdale, C., Novati, S. C., DePoy, D. L., Gould, A., Marshall, J. L., Trueblood, M., Trueblood, P., Johnson, J. A., Wright, J., McCrady, N., Wittenmyer, R. A., Johnson, S. A., Sergi, A., Wilson, M., and Sliski, D. H. (2017). KELT-20b: A Giant Planet with a Period of $P \sim 3.5$ days Transiting the $V \sim 7.6$ Early A Star HD 185603. *The Astronomical Journal*, 154(5):194.
- Luque, R., Casasayas-Barris, N., Parviainen, H., Chen, G., Pallé, E., Livingston, J., Béjar, V. J. S., Crouzet, N., Esparza-Borges, E., Fukui, A., Hidalgo, D., Kawashima, Y., Kawauchi, K., Klagyivik, P., Kurita, S., Kusakabe, N., de Leon, J. P., Madrigal-Aguado, A., Montañés-Rodríguez, P., Mori, M., Murgas, F., Narita, N., Nishiumi, T., Nowak, G., Oshagh, M., Sánchez-Benavente, M., Stangret, M., Tamura, M., Terada, Y., and Watanabe, N. (2020). Obliquity measurement and atmospheric characterization of the WASP-74 planetary system. *Astronomy & Astrophysics*, 642:A50. arXiv: 2007.11851.

- MacDonald, R. J., Goyal, J. M., and Lewis, N. K. (2020). Why Is it So Cold in Here? Explaining the Cold Temperatures Retrieved from Transmission Spectra of Exoplanet Atmospheres. *The Astrophysical Journal*, 893(2):L43.
- MacDonald, R. J. and Madhusudhan, N. (2017). HD 209458b in new light: evidence of nitrogen chemistry, patchy clouds and sub-solar water. *Monthly Notices of the Royal Astronomical Society*, 469(2):1979–1996.
- Madhusudhan, N. (2012). C/O ratio as a dimension for characterizing exoplanetary atmospheres. *The Astrophysical Journal*, 758(1):36.
- Magic, Z., Chiavassa, A., Collet, R., and Asplund, M. (2015). The Stagger-grid: A grid of 3D stellar atmosphere models: IV. Limb darkening coefficients. *Astronomy & Astrophysics*, 573:A90.
- Mancini, L., Southworth, J., Molliere, P., Tregloan-Reed, J., Juvan, I. G., Chen, G., Sarkis, P., Bruni, I., Ciceri, S., Andersen, M. I., Bozza, V., Bramich, D. M., Burgdorf, M., D’Ago, G., Dominik, M., Evans, D. F., Jaimes, R. F., Fossati, L., Henning, T., Hinse, T. C., Hundertmark, M., Jorgensen, U. G., Kerins, E., Korhonen, H., Kuffmeier, M., Longa, P., Peixinho, N., Popovas, A., Rabus, M., Rahvar, S., Skottfelt, J., Snodgrass, C., Tronsgaard, R., Wang, Y., and Wertz, O. (2019). Physical properties and transmission spectrum of the WASP-74 planetary system from multi-band photometry. *Monthly Notices of the Royal Astronomical Society*, 485(4):5168–5179. arXiv: 1903.02800.
- Mandel, K. and Agol, E. (2002). Analytic Light Curves for Planetary Transit Searches. *The Astrophysical Journal*, 580(2):L171–L175.
- Mandell, A. M., Haynes, K., Sinukoff, E., Madhusudhan, N., Burrows, A., and Deming, D. (2013). Exoplanet transit spectroscopy using WFC3: WASP-12 b, WASP-17 b, and WASP-19 b. *The Astrophysical Journal*, 779(2):128.
- Mansfield, M., Bean, J. L., Line, M. R., Parmentier, V., Kreidberg, L., Desert, J.-M., Fortney, J. J., Stevenson, K. B., Arcangeli, J., and Dragomir, D. (2018). A HST/WFC3 Thermal Emission Spectrum of the Hot Jupiter HAT-P-7b. *The Astronomical Journal*, 156(1):10. arXiv: 1805.00424.
- Mansfield, M., Bean, J. L., Stevenson, K. B., Komacek, T. D., Bell, T. J., Tan, X., Malik, M., Beatty, T. G., Wong, I., Cowan, N. B., Dang, L., Désert, J.-M., Fortney, J. J., Gaudi, B. S., Keating, D., Kempton, E. M.-R., Kreidberg, L., Line, M. R., Parmentier, V., Stassun, K. G., Swain, M. R., and Zellem, R. T. (2020). Evidence for H₂ Dissociation and Recombination Heat Transport in the Atmosphere of KELT-9b. *The Astrophysical Journal*, 888(2):L15.
- Mansfield, M., Line, M. R., Bean, J. L., Fortney, J. J., Parmentier, V., Wiser, L., Kempton, E. M.-R., Gharib-Nezhad, E., Sing, D. K., López-Morales, M., Baxter, C., Désert, J.-M., Swain, M. R., and Roudier, G. M. (2021). A unique hot Jupiter spectral sequence with evidence for compositional diversity. *Nature Astronomy*. arXiv: 2110.11272.

- May, E. M., Komacek, T. D., Stevenson, K. B., Kempton, E. M.-R., Bean, J. L., Malik, M., Ih, J., Mansfield, M., Savel, A. B., Deming, D., Desert, J.-M., Feng, Y. K., Fortney, J. J., Kataria, T., Lewis, N., Morley, C., Rauscher, E., and Showman, A. (2021). Spitzer Phase-curve Observations and Circulation Models of the Inflated Ultrahot Jupiter WASP-76b. *The Astronomical Journal*, 162(4):158.
- May, E. M. and Stevenson, K. B. (2020). Introducing a New Spitzer Master BLISS Map to Remove the Instrument-Systematic – Phase-Curve-Parameter Degeneracy, as Demonstrated by a Reanalysis of the 4.5 μ m WASP-43b Phase Curve. *The Astronomical Journal*, 160(3):140. arXiv: 2007.06618.
- Mayor, M. and Queloz, D. (1995). A Jupiter-mass companion to a solar-type star. *Nature*, 378(6555):355–359. Number: 6555 Publisher: Nature Publishing Group.
- McCullough, P. R., Crouzet, N., Deming, D., and Madhusudhan, N. (2014). Water vapor in the spectrum of the extrasolar planet HD 189733b. I. The transit. *The Astrophysical Journal*, page 11.
- Mikal-Evans, T., Sing, D. K., Kataria, T., Wakeford, H. R., Mayne, N. J., Lewis, N. K., Barstow, J. K., and Spake, J. J. (2020). Confirmation of water emission in the dayside spectrum of the ultrahot Jupiter WASP-121b. *Monthly Notices of the Royal Astronomical Society*, 496(2):1638–1644.
- Morley, C. V., Fortney, J. J., Kempton, E. M.-R., Marley, M. S., Vissler, C., and Zahnle, K. (2013). Quantitatively assessing the role of clouds in the transmission spectrum of GJ1214b. *The Astrophysical Journal*, 775(1):33.
- Moses, J. I., Madhusudhan, N., Visscher, C., and Freedman, R. S. (2013). Chemical consequences of the C/O ratio on hot Jupiters: Examples from WASP-12b, CoRoT-2b, XO-1b, and HD 189733b. *The Astrophysical Journal*, 763(1):25. arXiv: 1211.2996.
- Murray-Clay, R. A., Chiang, E. I., and Murray, N. (2009). Atmospheric escape from hot Jupiters. *The Astrophysical Journal*, 693(1):23–42.
- Muñoz, A. G. and Isaak, K. G. (2015). Probing exoplanet clouds with optical phase curves. *Proceedings of the National Academy of Sciences*, 112(44):13461–13466.
- Nikolov, N., Sing, D. K., Burrows, A. S., Fortney, J. J., Henry, G. W., Pont, F., Ballester, G. E., Aigrain, S., Wilson, P. A., Huitson, C. M., Gibson, N. P., Desert, J.-M., Etangs, A. L. d., Showman, A. P., Vidal-Madjar, A., Wakeford, H. R., and Zahnle, K. (2015). HST hot-Jupiter transmission spectral survey: Haze in the atmosphere of WASP-6b. *Monthly Notices of the Royal Astronomical Society*, 447(1):463–478. arXiv: 1411.4567.
- Nikolov, N., Sing, D. K., Pont, F., Burrows, A. S., Fortney, J. J., Ballester, G. E., Evans, T. M., Huitson, C. M., Wakeford, H. R., Wilson, P. A., Aigrain, S., Deming, D., Gibson, N. P., Henry, G. W., Knutson, H., Lecavelier des Etangs, A., Showman, A. P., Vidal-Madjar, A., and Zahnle, K. (2014). Hubble Space Telescope hot Jupiter transmission spectral survey: a detection of Na and strong optical absorption in HAT-P-1b. *Monthly Notices of the Royal Astronomical Society*, 437(1):46–66.

- Nugroho, S. K., Gibson, N. P., de Mooij, E. J. W., Watson, C. A., Kawahara, H., and Merritt, S. (2020). Searching for thermal inversion agents in the transmission spectrum of KELT-20b/MASCARA-2b: detection of neutral iron and ionised calcium H&K lines. *Monthly Notices of the Royal Astronomical Society*, 496(1):504–522.
- Oberg, K. I. and Bergin, E. A. (2021). Astrochemistry and compositions of planetary systems. *Physics Reports*, 893:1–48. arXiv:2010.03529 [astro-ph].
- Oberg, K. I., Murray-Clay, R., and Bergin, E. A. (2011). The effects of snowlines on C/O in planetary atmospheres. *The Astrophysical Journal*, 743(1):L16.
- Oswalt, T. D. (2003). The Future of Small Telescopes In The New Millennium. Volume II - The Telescopes We Use. *Astrophysics and Space Science Library*, 288.
- Parmentier, V., Fortney, J. J., Showman, A. P., Morley, C., and Marley, M. S. (2016). Transitions in the cloud composition of hot Jupiters. *The Astrophysical Journal*, 828(1):22.
- Parmentier, V., Line, M. R., Bean, J. L., Mansfield, M., Kreidberg, L., Lupu, R., Visscher, C., Desert, J.-M., Fortney, J. J., Deleuil, M., Arcangeli, J., Showman, A. P., and Marley, M. S. (2018). From thermal dissociation to condensation in the atmospheres of ultra hot Jupiters: WASP-121b in context. *Astronomy & Astrophysics*, 617:A110. arXiv: 1805.00096.
- Paulson, D. B., Cochran, W. D., and Hatzes, A. P. (2004). Searching for Planets in the Hyades. V. Limits on Planet Detection in the Presence of Stellar Activity. *The Astronomical Journal*, 127(6):3579–3586.
- Queloz, D., Henry, G. W., Sivan, J. P., Baliunas, S. L., Beuzit, J. L., Mayor, R. A. D. M., Naef, D., Perrier, C., and Udry, S. (2001). No planet for HD 166435. *Astronomy and Astrophysics*, 379(1):279–287. arXiv: astro-ph/0109491.
- Rodríguez, J. E., Quinn, S. N., Huang, C. X., Vanderburg, A., Penev, K., Brahm, R., Jordán, A., Ikwut-Ukwa, M., Tsirolik, S., Latham, D. W., Stassun, K. G., Shporer, A., Ziegler, C., Matthews, E., Eastman, J. D., Gaudi, B. S., Collins, K. A., Guerrero, N., Relles, H. M., Barclay, T., Batalha, N. M., Berlind, P., Bieryla, A., Bouma, L. G., Boyd, P. T., Burt, J., Calkins, M. L., Christiansen, J., Ciardi, D. R., Colón, K. D., Conti, D. M., Crossfield, I. J. M., Daylan, T., Dittmann, J., Dragomir, D., Dynes, S., Espinoza, N., Esquerdo, G. A., Essack, Z., Soto, A. G., Glidden, A., Günther, M. N., Henning, T., Jenkins, J. M., Kielkopf, J. F., Krishnamurthy, A., Law, N. M., Levine, A. M., Lewin, P., Mann, A. W., Morgan, E. H., Morris, R. L., Oelkers, R. J., Paegert, M., Pepper, J., Quintana, E. V., Ricker, G. R., Rowden, P., Seager, S., Sarkis, P., Schlieder, J. E., Sha, L., Tokovinin, A., Torres, G., Vanderspek, R. K., Villanueva Jr., S., Villaseñor, J. N., Winn, J. N., Wohler, B., Wong, I., Yahalomi, D. A., Yu, L., Zhan, Z., and Zhou, G. (2019). An Eccentric Massive Jupiter Orbiting a Sub-Giant on a 9.5 Day Period Discovered in the Transiting Exoplanet Survey Satellite Full Frame Images. *The Astronomical Journal*, 157(5):191. arXiv: 1901.09950.
- Seager, S., Bains, W., and Petkowski, J. (2016). Toward a List of Molecules as Potential Biosignature Gases for the Search for Life on Exoplanets and Applications to Terrestrial Biochemistry. *Astrobiology*, 16(6):465–485.

- Sheppard, K. B., Welbanks, L., Mandell, A., Madhusudhan, N., Nikolov, N., Deming, D., Henry, G. W., Williamson, M. H., Sing, D. K., López-Morales, M., Ih, J., Sanz-Forcada, J., Lavvas, P., Ballester, G. E., Evans, T. M., Muñoz, A. G., and Santos, L. A. D. (2021). The Hubble PanCET Program: A Metal-rich Atmosphere for the Inflated Hot Jupiter HAT-P-41b. *The Astronomical Journal*, 161(2):51. arXiv: 2010.09659.
- Showman, A. P., Fortney, J. J., Lian, Y., Marley, M. S., Freedman, R. S., Knutson, H. A., and Charbonneau, D. (2009). Atmospheric circulation of hot Jupiters: coupled radiative-dynamical general circulation model simulations of HD 189733b and HD 209458b. *The Astrophysical Journal*, 699(1):564–584.
- Shporer, A., O’Rourke, J. G., Knutson, H. A., Szabó, G. M., Zhao, M., Burrows, A., Fortney, J., Agol, E., Cowan, N. B., Desert, J.-M., Howard, A. W., Isaacson, H., Lewis, N. K., Showman, A. P., and Todorov, K. O. (2014). Atmospheric characterization of the hot Jupiter Kepler-13Ab. *The Astrophysical Journal*, 788(1):92.
- Sing, D. K. (2018). Observational Techniques With Transiting Exoplanetary Atmospheres. Number: arXiv:1804.07357 arXiv:1804.07357 [astro-ph].
- Sing, D. K., Fortney, J. J., Nikolov, N., Wakeford, H. R., Kataria, T., Evans, T. M., Aigrain, S., Ballester, G. E., Burrows, A. S., Deming, D., Désert, J.-M., Gibson, N. P., Henry, G. W., Huitson, C. M., Knutson, H. A., Etangs, A. L. d., Pont, F., Showman, A. P., Vidal-Madjar, A., Williamson, M. H., and Wilson, P. A. (2016). A continuum from clear to cloudy hot-Jupiter exoplanets without primordial water depletion. *Nature*, 529(7584):59–62.
- Sing, D. K., Lavvas, P., Ballester, G. E., Etangs, A. L. d., Marley, M. S., Nikolov, N., Ben-Jaffel, L., Bourrier, V., Buchhave, L. A., Deming, D. L., Ehrenreich, D., Mikal-Evans, T., Kataria, T., Lewis, N. K., López-Morales, M., Muñoz, A. G., Henry, G. W., Sanz-Forcada, J., Spake, J. J., and and, H. R. W. (2019). The Hubble Space Telescope PanCET Program: Exospheric Mg ii and Fe ii in the Near-ultraviolet Transmission Spectrum of WASP-121b Using Jitter Decorrelation. *The Astronomical Journal*, 158(2):91.
- Sing, D. K., Pont, F., Aigrain, S., Charbonneau, D., Desert, J.-M., Gibson, N., Gilliland, R., Hayek, W., Henry, G., Knutson, H., Etangs, A. L. d., Mazeh, T., and Shporer, A. (2011). Hubble Space Telescope Transmission Spectroscopy of the Exoplanet HD 189733b: High-altitude atmospheric haze in the optical and near-UV with STIS. *Monthly Notices of the Royal Astronomical Society*, 416(2):1443–1455. arXiv: 1103.0026.
- Sing, D. K., Vidal-Madjar, A., Desert, J.-M., Etangs, A. L. d., and Ballester, G. (2008). HST/STIS Optical Transit Transmission Spectra of the hot-Jupiter HD209458b. *The Astrophysical Journal*, 686(1):658–666. arXiv: 0802.3864.
- Sing, D. K., Wakeford, H. R., Showman, A. P., Nikolov, N., Fortney, J. J., Burrows, A. S., Ballester, G. E., Deming, D., Aigrain, S., Désert, J.-M., Gibson, N. P., Henry, G. W., Knutson, H., Lecavelier des Etangs, A., Pont, F., Vidal-Madjar, A., Williamson, M. W., and Wilson, P. A. (2015). HST hot-Jupiter transmission spectral survey: detection of potassium in WASP-31b along with a cloud deck and Rayleigh scattering. *Monthly Notices of the Royal Astronomical Society*, 446(3):2428–2443.

- Spake, J. J., Sing, D. K., Evans, T. M., Oklopčić, A., Bourrier, V., Kreidberg, L., Rackham, B. V., Irwin, J., Ehrenreich, D., Wyttenbach, A., Wakeford, H. R., Zhou, Y., Chubb, K. L., Nikolov, N., Goyal, J. M., Henry, G. W., Williamson, M. H., Blumenthal, S., Anderson, D. R., Hellier, C., Charbonneau, D., Udry, S., and Madhusudhan, N. (2018). Helium in the eroding atmosphere of an exoplanet. *Nature*, 557(7703):68–70.
- Spake, J. J., Sing, D. K., Wakeford, H. R., Nikolov, N., Mikal-Evans, T., Deming, D., Barstow, J. K., Anderson, D. R., Carter, A. L., Gillon, M., Goyal, J. M., Hebrard, G., Hellier, C., Kataria, T., Lam, K. W. F., Triaud, A. H. M. J., and Wheatley, P. J. (2020). Abundance measurements of H₂O and carbon-bearing species in the atmosphere of WASP-127b confirm its supersolar metallicity. *Monthly Notices of the Royal Astronomical Society*, 500(3):4042–4064.
- Stangret, M., Casasayas-Barris, N., Pallé, E., Yan, F., Sánchez-López, A., and López-Puertas, M. (2020). Detection of Fe I and Fe II in the atmosphere of MASCARA-2b using a cross-correlation method. *Astronomy & Astrophysics*, 638:A26. arXiv: 2003.04650.
- Stevenson, K. B. (2016). Quantifying and predicting the presence of clouds in exoplanet atmospheres. *The Astrophysical Journal*, 817(2):L16.
- Stevenson, K. B., Bean, J. L., Madhusudhan, N., and Harrington, J. (2014a). Deciphering the atmospheric composition of WASP-12b: a comprehensive analysis of its dayside emission. *The Astrophysical Journal*, 791(1):36.
- Stevenson, K. B., Desert, J.-M., Line, M. R., Bean, J. L., Fortney, J. J., Showman, A. P., Kataria, T., Kreidberg, L., McCullough, P. R., Henry, G. W., Charbonneau, D., Burrows, A., Seager, S., Madhusudhan, N., Williamson, M. H., and Homeier, D. (2014b). Thermal structure of an exoplanet atmosphere from phase-resolved emission spectroscopy. *Science*, 346(6211):838–841. arXiv: 1410.2241.
- Stevenson, K. B. and Fowler, J. (2019). Analyzing Eight Years of Transiting Exoplanet Observations Using WFC3’s Spatial Scan Monitor. *Instrument Science Report WFC3*. arXiv: 1910.02073.
- Stevenson, K. B., Harrington, J., Fortney, J. J., Loredó, T. J., Hardy, R. A., Nymeyer, S., Bowman, W. C., Cubillos, P., Bowman, M. O., and Hardin, M. (2012). Transit and Eclipse Analyses of Exoplanet HD 149026b Using BLISS Mapping. *The Astrophysical Journal*, 754(2):136. arXiv: 1108.2057.
- Stevenson, K. B., Line, M. R., Bean, J. L., Désert, J.-M., Fortney, J. J., Showman, A. P., Kataria, T., Kreidberg, L., and Feng, Y. K. (2017). *Spitzer* phase curve constraints for WASP-43b at 3.6 and 4.5 μ m. *The Astronomical Journal*, 153(2):68.
- Thorngren, D. and Fortney, J. J. (2019). Connecting Giant Planet Atmosphere and Interior Modeling: Constraints on Atmospheric Metal Enrichment. *The Astrophysical Journal*, 874(2):L31.
- Tremblin, P., Amundsen, D. S., Chabrier, G., Baraffe, I., Drummond, B., Hinkley, S., Mourier, P., and Venot, O. (2016). Cloudless atmospheres for L/T dwarfs and extrasolar giant planets. *The Astrophysical Journal*, 817(2):L19.

- Tremblin, P., Amundsen, D. S., Mourier, P., Baraffe, I., Chabrier, G., Drummond, B., Homeier, D., and Venot, O. (2015). Fingering convection and cloudless models for cool brown dwarf atmospheres. *The Astrophysical Journal*, 804(1):L17.
- Tsiaras, A., Waldmann, I. P., Zingales, T., Rocchetto, M., Morello, G., Damiano, M., Karpouzias, K., Tinetti, G., McKemmish, L. K., Tennyson, J., and Yurchenko, S. N. (2018). A Population Study of Gaseous Exoplanets. *The Astronomical Journal*, 155(4):156.
- von Essen, C., Mallonn, M., Hermansen, S., Nixon, M. C., Madhusudhan, N., Kjeldsen, H., and Tautvaišienė, G. (2020). HST/STIS transmission spectrum of the ultra-hot Jupiter WASP-76 b confirms the presence of sodium in its atmosphere. *Astronomy & Astrophysics*, 637:A76. arXiv: 2003.06424.
- Wakeford, H. R., Sing, D. K., Kataria, T., Deming, D., Nikolov, N., Lopez, E. D., Tremblin, P., Amundsen, D. S., Lewis, N. K., Mandell, A. M., Fortney, J. J., Knutson, H., Benneke, B., and Evans, T. M. (2017). HAT-P-26b: A Neptune-Mass Exoplanet with a Well Constrained Heavy Element Abundance. *Science*, 356(6338):628–631. arXiv: 1705.04354.
- Wakeford, H. R., Sing, D. K., Stevenson, K. B., Lewis, N. K., Pirzkal, N., Wilson, T. J., Goyal, J., Kataria, T., Mikal-Evans, T., Nikolov, N., and Spake, J. (2020). Into the UV: A precise transmission spectrum of HAT-P-41b using Hubble’s WFC3/UVIS G280 grism. *The Astronomical Journal*, 159(5):204. arXiv: 2003.00536.
- Wallack, N. L., Knutson, H. A., and Deming, D. (2021). Trends in Spitzer Secondary Eclipses. *The Astronomical Journal*, 162(1):36.
- Welbanks, L., Madhusudhan, N., Allard, N. F., Hubeny, I., Spiegelman, F., and Leininger, T. (2019). Mass-Metallicity Trends in Transiting Exoplanets from Atmospheric Abundances of H₂O, Na, and K. *The Astrophysical Journal*, 887(1):L20. arXiv: 1912.04904.
- West, R. G., Hellier, C., Almenara, J.-M., Anderson, D. R., Barros, S. C. C., Bouchy, F., Brown, D. J. A., Collier Cameron, A., Deleuil, M., Delrez, L., Doyle, A. P., Faedi, F., Fumel, A., Gillon, M., Gómez Maqueo Chew, Y., Hébrard, G., Jehin, E., Lendl, M., Maxted, P. F. L., Pepe, F., Pollacco, D., Queloz, D., Ségransan, D., Smalley, B., Smith, A. M. S., Southworth, J., Triaud, A. H. M. J., and Udry, S. (2016). Three irradiated and bloated hot Jupiters: WASP-76b, WASP-82b, and WASP-90b. *Astronomy & Astrophysics*, 585:A126.
- Wilkins, A., Deming, D., Madhusudhan, N., Burrows, A., Knutson, H., McCullough, P., and Ranjan, S. (2014). The Emergent 1.1-1.7 Micron Spectrum of the Exoplanet CoRoT-2b as Measured Using the Hubble Space Telescope. *The Astrophysical Journal*, 783(2):113. arXiv: 1401.4464.
- Wong, I., Kitzmann, D., Shporer, A., Heng, K., Fetherolf, T., Benneke, B., Daylan, T., Kane, S. R., Vanderspek, R., Seager, S., Winn, J. N., Jenkins, J. M., and Ting, E. B. (2021). Visible-light Phase Curves from the Second Year of the TESS Primary Mission. *The Astronomical Journal*, 162(4):127. arXiv: 2106.02610.

- Wöllert, M. and Brandner, W. (2015). A Lucky Imaging search for stellar sources near 74 transit hosts. *Astronomy & Astrophysics*, 579:A129.
- Yan, F., Pallé, E., Reiners, A., Molaverdikhani, K., Casasayas-Barris, N., Nortmann, L., Chen, G., Mollière, P., and Stangret, M. (2020). A temperature inversion with atomic iron in the ultra-hot dayside atmosphere of WASP-189b. *Astronomy & Astrophysics*, 640:L5.
- Yoshida, T. C., Nomura, H., Furuya, K., Tsukagoshi, T., and Lee, S. (2022). A New Method for Direct Measurement of Isotopologue Ratios in Protoplanetary Disks: A Case Study of the $^{12}\text{CO}/^{13}\text{CO}$ Ratio in the TW Hya Disk. *The Astrophysical Journal*, 932(2):126.
- Zhang, M., Chachan, Y., Kempton, E. M.-R., Knutson, H., Wenjun, and Chang (2020). PLATON II: New Capabilities And A Comprehensive Retrieval on HD 189733b Transit and Eclipse Data. *The Astrophysical Journal*, 899(1):27. arXiv: 2004.09513.
- Zhang, M., Knutson, H. A., Kataria, T., Schwartz, J. C., Cowan, N. B., Showman, A. P., Burrows, A., Fortney, J. J., Todorov, K., Desert, J.-M., Agol, E., and Deming, D. (2018). Phase Curves of WASP-33b and HD 149026b and a New Correlation between Phase Curve Offset and Irradiation Temperature. *The Astronomical Journal*, 155(2):83.
- Zhang, Y., Snellen, I. A. G., Bohn, A. J., Mollière, P., Ginski, C., Hoeijmakers, H. J., Kenworthy, M. A., Mamajek, E. E., Meshkat, T., Reggiani, M., and Snik, F. (2021). The ^{13}CO -rich atmosphere of a young accreting super-Jupiter. *Nature*, 595(7867):370–372.
- Zhou, Y., Apai, D., Lew, B. W. P., and Schneider, G. (2017). A Physical Model-based Correction for Charge Traps in the Hubble Space Telescope’s Wide Field Camera 3 Near-IR Detector and Its Applications to Transiting Exoplanets and Brown Dwarfs. *The Astronomical Journal*, 153(6):243.